ELECTROCHEMICAL SENSORS BASED ON GRAPHENE AND NANOBRUSH STRUCTURES FOR POINT OF USE DETECTION OF FOODBORNE PATHOGENS

A Dissertation

by

DANIELA ALVES DE OLIVEIRA

Submitted to the Graduate and Professional School of
Texas A&M University
in partial fulfillment of the requirements for the degree of

DOCTOR OF PHILOSOPHY

Chair of Committee,	Carmen Gomes
Co-Chair of Committee,	Zivko Nikolov
Committee Members,	Elena Castell-Perez
	Sandun Fernando
Head of Department,	John C. Tracy

December 2021

Major Subject: Biological and Agricultural Engineering

ABSTRACT

Recurrent foodborne pathogen outbreaks result in significant economic and public health burden. Thus, there is a critical need for the development of real-time and reliable detection methods to prevent disease outbreaks and replace current highly technical and time-consuming methods. This study aimed to develop different electrochemical biosensor platforms with enhanced limit of detection (LOD) and sensitivity for quantification of bacteria, *Listeria monocytogenes* and *Salmonella enterica* serovar Typhimurium, two of the most common foodborne bacteria. Two sensing platforms included stimuli-responsive polymer nanobrushes embedded with platinum nanoparticles fabricated using a simultaneous one-step sonoelectrodeposition method and subsequently functionalized with aptamers as biorecognition agents. Two pH-sensitive polymers, chitosan and alginate, were tested as well as different polymers preparation, grafting parameters, polymer response to pH changes (actuation) and aptamer concentrations. The optimized electrodeposition of chitosan/platinum (CHI/Pt) onto electrodes increased ($p < 0.05$) the average electroactive surface area (ESA) by 11 times compared to the bare electrode, while the alginate-thiomer/platinum (ALG-thiomer/Pt) deposition increased ($p < 0.05$) ESA by 7 times. Actuation protocol for the polymer brushes, i.e., bacteria capture with brushes on extended conformation and electrochemical signal transduction on collapsed state, led to the improved sensing performance for the detection of L. monocytogenes with a low LOD in chicken broth of 3.3 ± 0.9 CFU/mL and 4.4 ± 0.8 CFU/mL for the CHI/Pt-aptamer and ALG-thiomer/Pt-

aptamer sensors, respectively. A third sensing platform consisting of laser-induced graphene with nickel oxide nanoparticles (LIG-NiO) was fabricated by a two-step process using polyimide film and nickel acetate solution as substrates. The sensor was functionalized with *Salmonella*-specific antibodies and its performance investigated towards bacteria sensing in PBS alone and with interferent (*Escherichia coli*) and in chicken broth. The results showed that the immunosensor was highly specific and sensitive for the detection of *Salmonella* Typhimurium with a LOD of 1.28 ± 0.21 CFU/mL in chicken broth. All the three biosensors tested had a detection time of approximately 17 minutes (sample exposure plus testing) and a wide detection range from 10 to 10^6 CFU/mL of the target bacteria, which covers the relevant levels for food safety analysis. In addition to enable bacteria detection in very low levels with a time frame of minutes, the devices studied present other advantages such as easy fabrication and no need for labeling or bacteria concentration.

DEDICATION

To my family

Your love and support mean more than you know.

To my beloved son Lucas,

without whom this dissertation would have been completed much earlier

Totally worth it.

ACKNOWLEDGEMENTS

Foremost, I would like to express my sincere gratitude to my advisor, Dr. Carmen Gomes, for her patient and reliable guidance, encouragement, knowledge, and precious time dedicated to me throughout my graduate career. I could not have imagined having a better mentor. Also, I would like to thank my committee chair, Dr. Zivko Nikolov, for accepting me when Dr. Gomes left and for the support throughout the course of this research; and my committee members, Dr. Fernando, and Dr. Castell-Perez, for agreeing to serve on my committee. Thank you, too, to Dr. McLamore at Clemson University, Nicholas Cavallaro at the University of Florida, Dr. Jonathan Claussen, Cicero Pola and Raquel Soares at Iowa University for the collaboration and expertise regarding the subject.

Thank you also to the department faculty and staff for all help and guidance, and especially to Dr. Maria King and Sonya Stranges, for the conversations that helped to make my time at Texas A&M University a great experience. Thank you to all the lab colleagues that passed throughout the course of this research.

Finally, to my family and my friends, I cannot express how happy and grateful I am for you to be part of my life. I am profoundly thankful to my parents, my husband and my cousin, Maria Claudia, for all the good times and for all the love, support, encouragement, patience, reassurance, etc., on the not so good ones. My sincerest thanks and gratitude to all persons involved, directly or indirectly, in the completion of this work.

CONTRIBUTORS AND FUNDING SOURCES

Contributors

This work was supervised by a dissertation committee consisting of Dr. Nikolov (chair), Dr. Elena Castell-Perez and Dr. Sandun Fernando of the Department of Biological and Agricultural Engineering, Dr. Carmen Gomes of the Department of Mechanical Engineering at Iowa State University, and Dr. Eric McLamore of Clemson University.

The material characterization analyses were performed at the Materials Characterization Facility at Texas A&M University under the guidance, help and supervision of Dr. Yordanos Bisrat, Dr. Winson Kuo and Dr. Jing Wu. The LIG-NiO electrodes and its respective Raman characterization were provided by the Mechanical Engineering Department and the Department of Chemistry at Iowa State University.

All other work conducted for the thesis (or) dissertation was completed by the student independently.

Funding Sources

This work was supported by the National Science Foundation (NSF) under award numbers CBET-1756999, and CBET-1512659. Its contents are solely the responsibility of the authors and do not necessarily represent the official views of NSF.

Graduate study was supported by the NSF under award numbers CBET-1756999, and CBET-1512659, the Department of Biological & Agricultural Engineering and the Texas A&M University dissertation fellowship.

TABLE OF CONTENTS

Page

LIST OF FIGURES

Page

LIST OF TABLES

Page

CHAPTER I INTRODUCTION AND LITERATURE REVIEW

1.1. Objectives and dissertation organization

The overall goal of this study was to develop electrochemical biosensors with enhanced limit of detection and sensitivity for real-time detection of bacteria pathogens in food products.

Objective 1. Engineer stimuli-responsive polymer brushes (chitosan and alginate) decorated with platinum on the surface of the electrodes by a one-step sonoelectrodeposition process and optimize the deposition parameters of the polymer brushes.

Objective 2. Characterize the surface of the electrodes: polymer brushes with platinum nanoparticles and laser induced graphene with nickel oxide nanoparticles.

Objective 3. Optimize biorecognition agents loading concentration on the sensors.

Objective 4. Determine brush actuation properties and the best test conditions for sensing bacteria using the polymer brushes/platinum sensors.

Objective 5. Analyze the electrochemical response caused by the binding between biorecognition agents and bacteria to determine the performance of the biosensors for measuring pathogens in stagnant media, buffer suspension and food sample, over a range of bacteria concentration relevant to food safety.

This dissertation is organized as follows. Chapter I provides a general introduction on the current food safety data and the critical need to develop rapid (less

than one hour) and sensitive (ability to detect less than 5 CFU/mL of bacteria) biosensors to monitor food safety monitoring. Literature review on the foodborne bacteria that are the focus of this dissertation, materials used to fabricate the sensors and electrochemical methods applied for characterization and sensing is provided. Chapters II, III and IV contain studies of the individual electrodes and are organized as scientific publications. Each chapter further provides an introduction into the details of the study, followed by the methods undertaken. The results of each study are presented, followed by discussion of the findings and a chapter-specific conclusion. Chapter V summarizes the conclusions of this dissertation and the recommendations for future work.

1.2. Introduction

Despite strict regulations and the efforts of the food industry to prevent foodborne pathogens outbreaks, incidents involving foodborne infection continue to be an important public health problem and a threat to the economic well-being of the food system (FDA, 2018). It is estimated that in the United States each year approximately 48 million people get sick from a foodborne illness with an economic burden over $15.5 billion (Hoffmann, Maculloch, & Batz, 2015). The Economic Research Service (ERS) of the U.S. Department of Agriculture (USDA) reported in 2015 that five pathogens accounted for about 90% of that total estimated cost being three of them, *Salmonella* (all nontyphoidal species), *Toxoplasma gondii*, and *Listeria monocytogenes*, responsible for more than 60% of the total economic cost from major foodborne illnesses (Hoffmann et al., 2015). The bacteria targeted in this study, *Salmonella* and *Listeria monocytogenes,*

can be considered among the most dangerous to the health of the consumers, causing a great number of hospitalizations and deaths, and ranked first and third places in terms of economic burden, estimated in $3.7 billion and $2.8 billion, respectively, in a year (CDC, 2019; Hoffmann et al., 2015). In 2011, the U.S. Food and Drug Administration (FDA) launched the Food Safety and Modernization Act (FSMA) with the goal to ensure a higher level of public health by focusing on preventing food pathogen outbreaks instead of reacting to problems after disease outbreaks take place (FDA, 2018). The rules included more comprehensive, science-based preventive controls compulsory for all food products considering naturally occurring hazards, as well as those that may be introduced either unintentionally or intentionally (FDA, 2018). The FDA, the United States Department of Agriculture (USDA), and the European Union (EU) current rules include zero-tolerance for both *Salmonella* spp. and *L. monocytogenes* in ready-to-eat foods (V. S. Somerset, 2011), that are responsible for a great the number of food recalls. In 2020, the FDA reported 50 recalls of food products due to contamination or potential contamination by *Listeria* spp. and 71 by *Salmonella* spp. (FDA, 2021). This reinforces the need for real-time pathogen detection methods that can identify contaminated food products before reaching the public.

Although the traditional methods for food safety monitoring, such as culture and colony counting methods, provide valuable information, their major drawbacks are the labor and time required to yield results (requiring 2 to 7 days for analysis) (Vanegas, Gomes, Cavallaro, Giraldo-Escobar, & McLamore, 2017). Such a long delay has significant economic and safety implications as product deterioration and loss and

shipping complications can occur while the food product is being held. Other conventional and commercially available methods that are used to detect foodborne pathogens in the food industry include immunology-based methods such as enzyme-linked immunosorbent assay (ELISA), being the most commonly used, and polymerase chain reaction (PCR) methods that involve antigen–antibody association and deoxyribose nucleic acid/ribose nucleic acid (DNA/RNA) amplification and analysis, respectively. Despite faster than colony counting, these methods do not provide real-time results, require highly trained personnel and are still laborious, susceptible to errors and false readings, and expensive (Vanegas, Claussen, Mclamore, & Gomes, 2017; Velusamy, Arshak, Korostynska, Oliwa, & Adley, 2010). Valderrama et al. (Valderrama, Dudley, Doores, & Cutter, 2016) reviewed on commercially available methods for rapid detection and quantification of some bacteria, including *Listeria monocytogenes* and *Salmonella* spp. Most rapid methods can analyze a sample in a few minutes to a few hours but still lack sufficient sensitivity and specificity for direct testing of foods so that the sample still needs to be culture-enriched before analysis (Valderrama et al., 2016). Detection methods that are fast, sensitive, and require little expertise or training are desirable (Duncan, 2011). Hence, the development of biosensor platforms that could lead to reliable and faster results analysis than conventional techniques and determine whether foods are contaminated with pathogens in time to prevent them from reaching the public are critically needed.

Biosensors are analytical devices that use biological components as part of the detection method where the response of interactions between the biological component

and the target analyte can be detected by a transducer and converted to a quantifiable signal (electrical, optical, mass or temperature-based) (Arora, Sindhu, Dilbaghi, & Chaudhury, 2011; Thevenot, Toth, Durst, & Wilson, 2001). A wide variety of biological recognition elements and transducers can be used to detect analytes providing flexibility for biosensors applications in different fields (Velusamy et al., 2010). The transduction elements may include optical, electrochemical, piezoelectric, thermometric, or a combination of one or more of these elements (Vanegas, Claussen, et al., 2017). The biorecognition agents are the key to the specificity of the biosensors and can include antibody, enzymes, proteins (i.e., lectins), aptamers (i.e., DNA-based molecules), among others (Velusamy et al., 2010). Biosensors used in food applications include detection of pathogens, allergens, chemical contaminants, and others.

Electrochemical biosensors are classified into amperometric, potentiometric, impedimetric, and conductometric (Vanegas, Claussen, et al., 2017). Electrochemical biosensors are extensively studied for different applications due to the inherent advantages of their robustness, fast response, easy miniaturization, low detection limits, small analyte volumes, and simplicity of use (Grieshaber, Mackenzie, Vörös, & Reimhult, 2008). Electrochemical biosensors are able to detect the targeted bacteria by sensing the changes in the electrical properties caused by biochemical reactions or by binding events at the surface of the sensor (Grieshaber et al., 2008). Impedimetric-based biosensors measures the impedance change in a response to small amplitude sinusoidal excitation input when the molecular interactions take place at the surface of the working electrode (Grieshaber et al., 2008). It is solely based on the attachment of the analyte to

the surface of the electrode and its effect on the electrical properties of the biosensor (Arora et al., 2011). Thus, the bacteria concentration is measured by the difference on the electrical signal induced by their attachment to surface of the biosensor functionalized with bioreceptors, in order to be selective to the bacteria as well as to reduce the influence of nonspecific binding, which affects the capacitance in a similar way to the specific interaction (Lisdat & Schäfer, 2008).

The performance of the biosensor can be further improved by increasing the electrochemical surface area of the electrode (Adeloju & Hussain, 2016). The two options for increasing the electrochemical surface area are either by increasing the electrode diameter or by incorporating adequate nanomaterials (Adeloju & Hussain, 2016). The latter is more practical for keeping the biosensor compact and portable for use in both laboratory and in the field (Adeloju & Hussain, 2016). Materials with high surface area (i.e., high reactivity) are most suited for use in biosensors (Nigam, Chandra, & Bahadur, 2015). Improved performance of biosensors have been demonstrated with the use of nanomaterials that enhance transduction (Vanegas, Gomes, & Mclamore, 2016). Many researches on electrochemical sensing focused on developing transducer-composites based on carbon nanomaterials and/or noble nanometals to enhance the electrical conductivity of the sensor, combined with polymer nanoparticles to increase the surface area of the sensor and also to assist the binding of a large quantity of the bioreceptor agent (Vanegas et al., 2016). The synergistic effects resulting from combining nanostructured materials and biorecognition agents is promising to obtain sensors with high sensitivity, fast (real-time) response time, and low detection limit

(Vanegas et al., 2016). Thus, rapid and sensitive detection of foodborne contamination can be successfully achieved by using nanoparticles in very low concentrations in combination with biofunctionalizing the sensor with biological recognition elements resulting in enhanced biosensor performance (H. Yang, Li, & Jiang, 2008).

Noble metal nanomaterials have been used as transducer materials for improving performance of electrochemical biosensors because of their excellent electrical and thermal conductivity, as well as biocompatibility, chemical resistance, thermal stability, and large specific surface area (Yu et al., 2021). Biosensors based on platinum nanomaterials have been widely used in the past few decades as platinum nanoparticles have unique properties such as their surface effect, volume effect, quantum size effect, and macroscopic quantum tunneling effect (Yu et al., 2021). Platinum nanoparticles are used on biosensors to enhance electron transfer due to higher current densities and faster mass transport compared to larger macro particles as well as increased electrocatalytic behavior (Claussen et al., 2012; Taguchi et al., 2016).

Carbon based nanomaterials have remarkable mechanical and electrical properties (Lawal, 2018). Nanostructured conducting allotropes of carbon such as carbon nanotubes, carbon quantum dots, graphene, and graphene oxide are excellent materials for sensing applications due to their mechanical strength, electrochemical properties, and inert nature (Wallace, Chen, Li, Moulton, & Razal, 2010). Graphene in particular presents other unique properties, such as a high surface-to-volume ratio, high electrical conductivity, chemical stability, and biocompatibility, that result in increased electroactive surface area of the transducing surface, enhanced electron transfer, and

improved adsorption of molecules (Lawal, 2018). The combination of graphene with metals and metal oxide nanoparticles can further improve electrochemical performance including enhanced electron transport, surface wettability, stability, and biorecognition agent immobilization (Z. Wan et al., 2020; Ye et al., 2015).

Stimuli-responsive polymers can undergo chemical and conformational changes in response to small external variations in the environment and may improve the performance of biosensors by utilizing the transition between collapsed and expanded states (shrunken and swollen) (Zhao, Liu, Lu, Zhou, & Li, 2012). When in their hydrophilic configuration, these polymers form hydrogen-bonds with water which results in a swollen hydrogel. When in hydrophobic form, the polymer-water hydrogen bonds weaken, the polymer-polymer interactions among the hydrophobic groups predominate and the polymer chains contract to minimize thermodynamically unfavorable interactions between the aqueous environment and the hydrophobic polymer groups (Schild, 1992). In this work, two pH-responsive polymers were applied, chitosan and alginate, which are further detailed in the literature review.

A polymer brush consists of end-tethered (grafted, anchored) polymer chain stretched away from the substrate due to the volume-excluded effect. Recent studies with polymers grafting over a metal layer aimed to build nanobrushes which may have the capability to increase the total amount of bioreceptors that can be loaded onto the surface of the biosensor based on polymer length, among other functions (Giacobassi et al., 2021; Hills, Oliveira, Cavallaro, Gomes, & McLamore, 2018). A drawback in this approach is the long electrode preparation. Electrodeposition is a versatile and efficient

approach for fabricating coatings in which an imposed electric field is employed to direct charged particles dispersed in a liquid towards an electrode (Z. Wang et al., 2014). Electrodeposition has advantages of short processing time, the possibility of room temperature processing, and no requirement for cross-link agents (Z. Wang et al., 2014). Therefore, this work aimed to design polymeric nanobrushes embedded with nanoplatinum grafted on the surface of the electrode simultaneously in a one-step sonoelectrodeposition procedure, allowing the adsorption of the platinum nanoparticles to the polymer brush. It is hypothesized that this new nanobrush structure will improve the transportation of electrons when deposited onto the surface of the electrode and will enhance the bacteria capture and detection.

1.3. Literature review

1.3.1. Bacteria

1.3.1.1. Listeria

Listeria monocytogenes is a Gram-positive, psychrotrophic and virulent foodborne bacteria species ubiquitous in water and soil that causes hundreds of deaths in the U.S. annually (V. S. Somerset, 2011). Healthy individuals might have mild symptoms when infected with *L. monocytogenes*, while others may develop fever, muscle aches, nausea and vomiting, and, sometimes, diarrhea (FDA, 2012). In vulnerable populations with weak immune systems, however; a more severe form of infection may develop spreading to the nervous system, and symptoms may include headache, stiff neck, confusion, loss of balance, and convulsions potentially causing

meningitis (FDA, 2012). Pregnant women may abort or be stillborn, and those born alive may have bacteremia and meningitis (FDA, 2012). One-third of confirmed cases of maternal-fetal *L. monocytogenes* infections lead to abortion or stillbirth (FDA, 2012). Although not a leading cause of foodborne illness, *L. monocytogenes* is among the leading causes of death from foodborne illness (FDA, 2012).

L. monocytogenes is particularly difficult to monitor in food processing environments due to its ability to proliferate under low moisture content, high salinity conditions, or at temperatures associated with common refrigerator and freezer units (Noordhout et al., 2014). Also, cross contamination on food handlers and the food processing environment itself is a bigger concern in the case of *Listeria* (FDA, 2012). In the last decade some food products that were a source of outbreaks of *Listeria* include fruits, frozen vegetables, deli meats, pork products, cheese, ice cream and other dairy products (CDC, 2021a). The USDA establishes a minimum of products and surface samples to be collected according to the daily production volume of the industry for ready-to-eat meat and poultry products (USDA, 2014). This USDA guideline specifies that if a product tests positive for *Listeria*, then the product will be considered adulterated and the product must be reworked or destroyed (USDA, 2014). Additionally, in the case of finding *Listeria* on surfaces the establishments are expected to take corrective action to address *Listeria* positives so that product does not become adulterated (USDA, 2014).

1.3.1.2. Salmonella

Salmonella is a motile, non-spore forming, Gram-negative, rod-shaped bacterium in the family Enterobacteriaceae (FDA, 2012). *Salmonella* is a ubiquitous and hardy bacteria that can survive several weeks in a dry environment and several months in water (WHO, 2018). The species *Salmonella enterica* is an important public health concern as it is among the most commonly encountered bacteria and a prominent cause of foodborne illness around the world (V. S. Somerset, 2011). *Salmonella enterica* subsp. *enterica* is further divided into numerous serotypes, including *S.* Enteritidis and *S.* Typhimurium, which are common in the U.S. (FDA, 2012). *Salmonella* causes gastrointestinal illness such as nausea, vomiting, diarrhea, cramps, and fever, called salmonellosis, generally lasting up to a week (FDA, 2012). Most patients recover well from salmonellosis, however; in some cases, particularly in children and elderly patients, the associated dehydration can become severe and life-threatening (WHO, 2018). This bacterium is usually associated with poultry and eggs, although many kinds of food can become contaminated with *Salmonella*, such as fruits and vegetables, and even dry foods, like spices and raw tree nuts (FDA, 2012). Important measures for preventing foodborne illness from *Salmonella* include thorough cooking, hand washing and avoiding cross contamination between cooked and raw foods (FDA, 2012).

Salmonella enterica is a notable target of interest for public health as it has been demonstrated to have a multi-drug resistance (V. S. Somerset, 2011). On the current performance standard established by the U.S. Department of Agriculture's Food Safety Inspection Services (USDA-FSIS), the acceptable number of *Salmonella*-positive samples is 5 out of a 51 on chicken whole carcass rinses (USDA, 2019). The inability to

provide rapid and definitive diagnosis delays initiation of appropriate control measures, increases the likelihood of continued colonization and contamination and consequently foodborne illnesses.

1.3.2. Polymers

Chitosan and alginate are natural biodegradable, biocompatible and non-toxic polysaccharidic polymers that have the ability to form hydrogel and to respond to fluctuations in pH (S. Q. Liu, 2007). In pH-sensitive polymers, swelling is mainly influenced by intramolecular interactions between the polymer chains, which depend on the crosslinking density set during the formation of the network (Berger et al., 2004). An increase in crosslinking density induces a decrease in swelling and pH-sensitivity, by improving the stability of the network (Berger et al., 2004). Stimuli-responsive polysaccharides can be electrochemically deposited on the surface of electrodes in response to localized electrical signals that generate pH gradients that can locally neutralize the polysaccharide and induce its macromolecular chain crosslinking (Cheng et al., 2011). Electrochemical deposition of cationic polymers (positively charged) is normally done cathodically, i.e., the polymer precipitates on the surface of the cathode, while anionic polymers are normally deposited anodically (precipitation on the surface of the anode) (Z. Wang et al., 2014).

Chitosan is a linear long-chained molecule composed of D-glucosamine units jointed by β-1,4-glycosidic bonds with randomly inserted N-acetylglucosamine units (S. Q. Liu, 2007). Chitosan is a partially deacetylated derivative of chitin, which is the

second most abundant polysaccharide after cellulose (Elieh-Ali-Komi & Hamblin, 2016). The main natural sources of chitin are shrimp and crab shells, which are an abundant byproduct of the food-processing industry (Elieh-Ali-Komi & Hamblin, 2016). Chitin, a polymer molecule with more than 50% N-acetylglucosamine units, is converted through enzymatic or chemical deacetylation to chitosan, which contain more than 50% D-glucosamine units (Elieh-Ali-Komi & Hamblin, 2016; S. Q. Liu, 2007). Chitosan is a semicrystalline molecule and its crystallinity is regulated by deacetylation (S. Q. Liu, 2007). The higher degree of deacetylation the more crystallinity and stable is the chitosan (S. Q. Liu, 2007). Chitosan is insoluble in water, but soluble in acidic solutions when it is hydrophilic/positively charged and binds to negatively charged surfaces shifting to hydrophobic at pH values above its pKa of ~6.5 (S. Q. Liu, 2007). The charge density of chitosan is dependent on pH (S. Q. Liu, 2007). At pH values below pKa, the charge density and therefore the crosslinking density of chitosan decrease, which leads to swelling (Berger et al., 2004). Moreover, swelling is favored by the protonation and repulsion of chitosan free ammonium groups (Berger et al., 2004).

Alginates are linear polysaccharides isolated from brown algae and certain bacteria containing repeating β-mannuronic and α-guluronic acids (S. Q. Liu, 2007). Commercially available alginates are typically extracted from different species of brown algae (*Phaeophyceae*) with molecular weight ranging between 32,000 and 400,000 g/mol, additionally bacterial biosynthesis may provide alginate with more defined chemical structures and physical properties (Lee & Mooney, 2012). Alginates are actually block copolymers, and the ratio of β-mannuronic acid and α-guluronic acid as

well as the length of each block varies depending on the natural source (Lee & Mooney, 2012). Normally, alginate gels are formed using divalent cations as crosslinkers to link α-guluronic acid units between different polymer chains (S. Q. Liu, 2007). The mechanical properties of alginate gels can be enhanced by increasing the length of α-guluronic acid block and molecular weight (Lee & Mooney, 2012). However, an alginate solution formed from high molecular weight polymer becomes greatly viscous (Lee & Mooney, 2012). Also, the viscosity of alginate solutions increase as pH decreases, and reach a maximum around pH = 3-3.5, as carboxylate groups in the alginate backbone become protonated and form hydrogen bonds (Lee & Mooney, 2012). Alginates exhibits similar behavior of chitosan, but at opposing pH ranges. It is an anionic molecule with pKa of approximately 3.5. Above the pKa, alginate is hydrophilic and in environments that are below this pH it is hydrophobic (Augst, Kong, & Mooney, 2006; Gu, Amsden, & Neufeld, 2004).

1.3.3. Laser-induced graphene with nickel oxide

Carbon based nanomaterials have remarkable mechanical and electrical properties (Lawal, 2018). Graphene represents a class of carbon materials based on a monolayer of carbon atoms, a one-atom-thick sheet, arranged in a honeycomb lattice (Lawal, 2018). With unique properties, such as a high surface-to-volume ratio, high electrical conductivity, chemical stability, biocompatibility, and robust mechanical strength, the use of graphene is advantageous for electrochemical biosensors as it increases the electroactive area of the transducing surface, enhances electron transfer,

and promotes adsorption of molecules (Lawal, 2018). Therefore, graphene-electroanalytical based electrodes generally have higher sensitivities, lower limits of detection, and faster electron transfer kinetics than traditional carbon electrodes (Lawal, 2018). Additionally, excellent fluorescence quenching ability of graphene has been exploited in optical sensors (Lawal, 2018).

Several kinds of graphene have been synthesized and many techniques are available; however, most of them are time consuming, require high thermal and/or low-pressure (vacuum), or involve multiple steps toward chemical formation of graphene (Cooper et al., 2012). Pristine graphene, obtained by the mechanical cleavage of graphite (exfoliation), has some exceptional properties; however, this process is time consuming with a low throughput and is not suitable for mass production (Lawal, 2018). Another method is the thermal decomposition of silicon carbide that consists of heating the substrate in ultra-high vacuum and temperature to sublimate the Si from the material and leave behind a carbon-rich surface (Cooper et al., 2012). In the chemical vapor deposition (CVD) technique, carbon is supplied in gas form and a metal (nickel, cobalt, copper, iron) is used as both catalyst and substrate (prepatterned surface) to grow the graphene layer also under high temperature and vacuum (Cooper et al., 2012). Other examples of graphene synthesis procedures include radio frequency plasma and chemical-based techniques, such as reduction of graphene oxide and wet chemical synthesis (Cooper et al., 2012).

Graphene-based electronics offer great promise for a wide variety of applications, including sensors and other flexible electronics due to the aforementioned

unique material properties of graphene. Some scalable manufacturing protocols for graphene-based electrical circuits comprise solution-phase printing, that are capable of printing graphene electrodes from graphene flakes synthesized from bulk chemical exfoliation of graphite, which includes inkjet printing, screen printing, dispenser printing, and direct laser scribing, among others (Garland et al., 2018; Soares et al., 2020). Solution phase printing techniques generally require additional post-print processing steps, such as thermal, laser, or photonic annealing to improve electrical conductivity (Garland et al., 2018).

A recent alternative to printed graphene circuits is a simple one-step, direct-write graphene electrode fabrication method, called laser-induced graphene (LIG) (J. Lin et al., 2014; Ye, James, & Tour, 2018). LIG is fabricated via a one-step direct CO_2 or UV laser-scribing process on commercial carbon-based polymer films (i.e., polyimide, also known as Kapton tape) in air that forms 3D graphene layers by converting sp^3-hybridized carbon found in the substrates into sp^2-hybridized carbon (Garland et al., 2018; J. Lin et al., 2014). The laser can selectively design any distinct circuit patterns on the film converting the film into nano/micro-structured or porous high-surface graphene by combining both the graphene synthesis and graphene electrode fabrication steps into one simple process (Soares et al., 2020). This process is inherently scalable and cost-effective as it requires neither ink formulation and post-print annealing that are involved in graphene printing techniques nor prior patterning of the substrate with a metal catalyst or chemical etching/cleaning techniques associated with chemical vapor deposition fabrication of graphene (Garland et al., 2018; J. Lin et al., 2014). Direct synthesis of LIG

on polyimide films allows the development of disposable, mass scalable, low-cost sensors (Cinti, Volpe, Piermarini, Delibato, & Palleschi, 2017; Vanegas et al., 2018). LIG applications as sensors include detection of glucose (Tehrani & Bavarian, 2016), ascorbic acid, dopamine, and uric acid (Nayak, Kurra, Xia, & Alshareef, 2016), tyrosine and uric acid in sweat (Y. Yang et al., 2020), thrombin in serum (Fenzl et al., 2017) and nitrogen in soil (Garland et al., 2018). Studies with LIG that can be applied in improving food quality and safety include fouling biofilm resistant surfaces, one of the main challenges in the food industry, and antibacterial electrodes (Singh et al., 2017); monitoring of biogenic amines which in high levels is an indication of possible microbiological contamination and can cause food poisoning (Vanegas et al., 2018); detection of the antibiotic chloramphenicol which is banned in food production (Cardoso et al., 2019); and detection of foodborne pathogens in food samples (Soares et al., 2020). In the work with bacteria detection, Soares et al. (2020) reported that LIG biosensors functionalized with *Salmonella*-specific antibodies were able to detect *S.* Typhimurium in chicken broth across a wide linear range (25 to 10^5 CFU/mL) and with a low detection limit (13 ± 7 CFU/mL).

A second step can be added to the LIG process to deposit metal oxides to further improve sensors performance. Metal oxides have been investigated for use in supercapacitor electrodes to improve specific capacitance and energy density, as some metal oxides show excellent pseudo-capacitance (Zhi, Xiang, Li, Li, & Wu, 2013). The pseudo-capacitance is originated from the weakly attached surface ions (Zhi et al., 2013). Metal oxide electrodes have one order higher specific capacitance and energy

density than carbon electrodes at a slow scan rate or at a low current density; however, only a small percentage of this capacitance is retained when the scan rate increases (Zhi et al., 2013). Also, the conductivity of most metal oxides is very low, and their high resistivity increases both the sheet resistance and the charge transfer resistance of the electrodes (Zhi et al., 2013). Therefore, metal oxides may not be employed alone on electrodes for practical purpose and a composite electrode containing both carbon and metal oxide which combines the merits and mitigate the shortcomings of both the components may be a logical solution (Zhi et al., 2013). In the carbon-metal oxide composite, the carbon serves as physical support for the metal oxides and provide the channels for charge transport with high electronic conductivity. While the metal oxides contribute with high specific capacitance and high energy density to store the charge and the energy. The combination of graphene with metal oxides provides synergistic effects improving their electrochemical properties with developed electron conductive network and shortened ion transport paths due to size effects and interfacial interactions, additionally the materials cost can be reduced (Z. Wu, Zhou, Yin, & Ren, 2012; Zhi et al., 2013). Among the metal oxides, nickel oxide (NiO) presents advantages of high theoretical capacity, high natural abundance, nontoxicity, low cost, and environmental benignity (Chu et al., 2016; Z. Wu et al., 2012). The direct charge transfer between NiO and graphene is expected to improve electron-transfer kinetics properties of the electrode due to a more direct and rapid electron transfer within the electrode material (W. Huang et al., 2017). Most of the research available involving graphene with NiO is related to energy storage, fuel cells (Chu et al., 2016; Kucherenko et al., 2021; D. Wang et al.,

2010; Z. Wu et al., 2012; Zhi et al., 2013), and more recently to sensors for monitoring of toxic and hazardous gas (NO_2) in environmental pollution (Niavol et al., 2020).

1.3.4. Biorecognition agents

1.3.4.1. Antibodies

Antibodies are host glycoproteins, members of the immunoglobulin (I_g) superfamily, that serve as the first response of the immune system to external molecules and organisms (Lipman, Jackson, Trudel, & Weis-Garcia, 2005; Mirsky, 2004). The ability of antibodies to bind an antigen with a high degree of affinity and specificity has led to their ubiquitous use in a variety of scientific disciplines (Lipman et al., 2005). Antibodies are composed of four polypeptides, two identical heavy chains (~55 kD) and two identical light chains (~25 kD), which are held together by a number of disulfide bonds (Lipman et al., 2005; Stapleton, Kennedy, & Tully, 2005). The antibody chains can be further divided into constant (C) and variable (V) regions based on their amino acid variability (Stapleton et al., 2005). The resulting molecule is often represented by a schematic Y-shaped molecule of~150 kD (Figure 1.1) (Lipman et al., 2005). Amino termini of the variable regions of both chains associate to form the antigen-binding domain (arms of the Y), also known as paratope (Lipman et al., 2005; Mirsky, 2004). Each arm of the Y or monovalent antibody fragment (F_{ab}) domain contains a binding site, making each antibody molecule at least bivalent (Lipman et al., 2005). The region connecting the two arms (F_{ab}) of the antibody molecule (antigen-binding domains) and the tail (F_c) imparts lateral and rotational movement to the antigen-binding domains,

providing the antibody the ability to interact with a variety of antigen presentations (Lipman et al., 2005). The binding of the antigen is crucially determined by the composition and conformation of the paratope and, hence, the "recognition" of the ligand (Mirsky, 2004). The selectivity and affinity of the interaction between the antibody and the corresponding antigen is the basis of the recognition part of immunosensors and determines its potential applications (Mirsky, 2004).

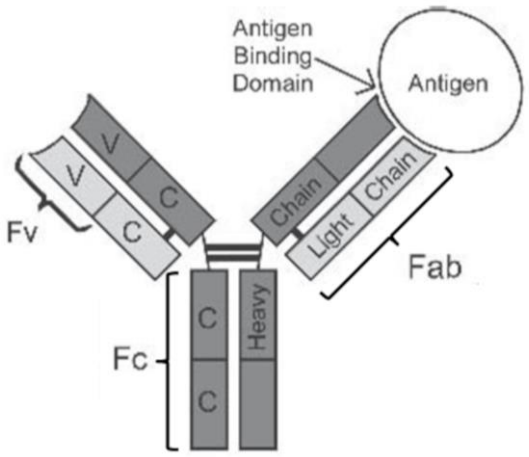

Figure 1.1 The basic structural molecule of an antibody (adapted from Lipman et al., 2005).

Polyclonal antibodies are secreted in response to repeated immunization of animals with a desired antigen; rabbits, goats, and sheep are generally used (Stapleton et al., 2005). When a sufficient titer (antibody concentration) is obtained, the animal is bled and high concentrations of antibodies can be purified from relatively small amounts of serum (Stapleton et al., 2005). Polyclonal antibodies can be very specific; however, on this process a mixed population of antigen reactive B-cells is stimulated, which recognize different epitopes on the immunogen producing a heterogeneous population of

antibodies, with a wide range of binding affinities (Stapleton et al., 2005). Consequently, to reproduce in subsequent immunizations can be hard and a consistent source of antibodies cannot be generated (Stapleton et al., 2005).

Monoclonal antibodies; however, are derived from a single clone of B-cells providing a single epitope and identical antigen-binding specificity (Stapleton et al., 2005). Monoclonal antibodies are most commonly produced by employing the hybridoma technique in which splenocytes (normal B-cells) from an immunized animal are fused with myeloma cells (tumor B-cells) derived from a common ancestor known to have lost the ability to produce immunoglobulin type G, so that the only antibody produced is derived from the antigen-sensitized splenocyte (Stapleton et al., 2005). The resultant hybrid cell is known as a hybridoma and inherits antigen specificity from the splenocytes and immortality from the myeloma cells, thus creating a permanent cell line, which secretes a homogeneous antibody of desired specificity in potentially limitless amounts (Stapleton et al., 2005). Polyclonal antibodies can be produced quicker (within several months of initiating immunizations) and cheaper than monoclonal antibodies, and do not require the same amount of expertise or time; the generation of hybridomas and subsequent production of monoclonal antibodies can take up to a year, therefore, requiring considerably more expense and time (Lipman et al., 2005; Stapleton et al., 2005).

Antibodies have long been the most popular biorecognition elements used in biosensors (Y. Wang, Ye, & Ying, 2012), also known as immunosensors. The main advantage of the use of antibodies as biorecognition agents is their sensitivity, selectivity

(Y. Wang, Ye, & Ying, 2012) and the wide variety of antibodies commercially available. Immunosensors applied for detection of a multitude of bacteria can be found in the literature. For instance, Joung et al. (2013) immobilized antibody on a nanoporous alumina membrane modified with hyaluronic acid for the impedimetric detection of *E. coli* O157:H7 in whole milk, reporting detection limits as low as 83.7 CFU/mL (95% confidence). R. Wang, Ruan, Kanayeva, Lassiter, & Li (2008) developed a TiO_2 nanowire bundle based immunosensor functionalized with anti-*Listeria* antibodies that can detect as low as 10^2 CFU/mL and up to 10^7 CFU/mL of *L. monocytogenes* in 1 h without significant interference from other foodborne pathogens. Wen, Wang, Sotero, & Li (2017) developed a portable impedance immunosensing system consisting of a gold interdigitated array microelectrode functionalized with antibodies for detection of *S.* Typhimurium, reporting LOD of 10^3 CFU/mL, detection time of 1 h and a sensing range between 10^3 and 10^7 CFU/mL. Vu et al. (2021) immobilized antibodies in a carbon screen-printed electrode modified with gold nanoparticles for label-free detection of *Escherichia coli* O157:H7, with limit of detection of 15 CFU/mL in about 30 min.

1.3.4.2. Aptamers

Aptamers are biomolecular ligands composed of nucleic acids developed to bind with high-affinity and specificity to a target molecule (Kärkkäinen et al., 2011). Essentially, aptamers are small, single-stranded DNA or RNA oligonucleotides, often ranging between 20 to 60 nucleotides (Ali, Elsherbiny, & Emara, 2019). The process by which aptamers are relatively rapidly selected *in vitro* is called systematic evolution of

ligands by exponential enrichment (SELEX) and once they have been identified they can be inexpensively produced either synthetically or enzymatically (Kärkkäinen et al., 2011); and large scale production is also possible for mass production of pharmaceuticals or diagnostic kits (Kedzierski, Khoshnejad, & Caltagirone, 2013). The SELEX process entails progressive separation of single-stranded DNAs or RNAs (ssDNA/RNA) using a combinatorial single-stranded oligonucleotide library via repeated rounds of binding, partitioning, and amplification (Ali et al., 2019). Different modified SELEX techniques have emerged over the past three decades (Ali et al., 2019).

Although completely distinct from antibodies, aptamers molecules mimic the properties of antibodies in several formats and are simply considered nucleotide analogues of antibodies (Ali et al., 2019). However, compared to antibodies, the generation of aptamers is significantly easier and cheaper (Ali et al., 2019). One significant advantage of aptamers over other biomolecules, such as antibodies, is that no animals or animal-derived cells or tissues are needed for their production which have clear ethical and financial benefits (Kärkkäinen et al., 2011). Other advantages include their specificity and inertness towards the surrounding cells, higher binding affinity, better target discrimination, minimized batch-to-batch variation, their smaller size allows for easy entry into biological compartments, dyes or functional groups can be easily added during synthesis, reduced side effects and stable shelf life (Ali et al., 2019; Kedzierski et al., 2013). Aptamers are remarkably stable; lyophilized aptamers can be stored for years without loss of activity and once they are reconstituted, aptamers can be boiled or subjected to numerous freeze-thaw cycles (Pendergrast, Marsh, Grate, Healy,

& Stanton, 2005). Additionally, aptamers are considerably smaller than antibodies, allowing higher densities of sensing elements on the sensor surface leading to higher sensitivity and lower non-specific (Y. Wang, Ye, & Ying, 2012). These characteristics allied with the target specific binding (as opposed to other material in the sample matrix) are advantageous for detecting pathogenic bacteria in food, as the aptamers should bind solely to the target pathogen opposed to other microorganisms or food matrix components (Kärkkäinen et al., 2011). As pathogenic microorganisms have complex target structures, the targets for screening aptamers of pathogenic microorganisms are usually the specific purified proteins that exist on the cell surface, i.e., there are specific aptamers for each type of bacteria (Y. Wang, Ye, Si, & Ying, 2012).

There are many examples of aptamers used in biosensors to detect pathogens in the literature, including Guo et al. (2020) that proposed aptamer and antibody-based dual recognition units using aggregation-induced emission nanoparticles and magnetic nanoparticles and reported a range of detection for *L. monocytogenes* of 10-10^6 CFU/mL after a 90 min incubation time. Sidhu et al. (2016) functionalized platinum interdigitated array microelectrodes with aptamer and reported a limit of detection of 5.39 CFU/mL of *Listeria* spp. in PBS with 17 min response time. W. Wu et al. (2014) reported the detection of *Salmonella* Enteritidis using aptamers, fluorescence label and fluorescence quenching graphene oxide, with limit of detection as low as 40 CFU/mL of *S.* Enteritidis in 30 min.

Table 1.1 Comparison between aptamers and antibodies.

	Aptamer	**Antibodies**
Molecular weight	Small (~12–30 kDa)	Relatively big (~150–180 kDa)
Secondary structures	Various structures: hairpin, loop, G-quadruplex, etc.	β-sheets
Generation time	Few hours to months	Several months (~six months)
Batches variations	Low	High
Immunogenicity	Low	High
Minimal target size	Targets small sizes ~60 Da	~600 Da
Targets	Wide range of targets	Immunogenic molecules
Shelf life	Long	Short
Allowed chemical modifications	Various modifications	Limited modifications
Nuclease degradation	Sensitive	Resistant
***In vivo* half-life**	Short (~20 min)	Long (~one month)
Stability	Very stable	Sensitive to temperature and pH changes
Cost	Lower	Higher

Reprinted from Ali et al. (2019)

1.3.5. Electrochemistry

Electrochemistry is a powerful tool to probe reactions involving electron transfers and relates the flow of electrons to chemical changes (Elgrishi et al., 2018). Cyclic voltammetry (CV) is a popular tool for studying electrochemical reactions such as biosynthetic reactions, generation of free radicals, effects of ligands on the oxidation/reduction potential of the central metal ion in complexes and multinuclear clusters which are useful in the selection of the proper oxidizing agent, introduction of functional groups and removal blocking agents (Elgrishi et al., 2018; Mabbott, 1983). This technique gives important information for studies involving solar energy conversion and for model studies of enzymatic catalysis (Mabbott, 1983). Depending on the molecule, a change in the number of electrons may induce changes on its structure and reactivity. An electron transfer may therefore be followed by a chemical reaction and, in such cases, cyclic voltammetry may be used to study the process and the species involved (Carriedo, 1988).

Based on Mabbott (1983), Kissinger & Heineman (1983) and Elgrishi et al. (2018) reviews, the fundamentals of cyclic voltammetry consist of cycling the potential of an electrode, which is immersed in an unstirred electrolyte solution, and measuring the resulting current. The potential (excitation signal) of the working electrode is controlled versus a reference electrode such as a silver/silver chloride electrode (Ag/AgCl) and is a linear potential scan with a triangular waveform as shown in Figure 1.2. This triangular potential excitation signal sweeps the potential of the electrode between two values, also called switching potentials (b and d), where the direction of the

scan is reversed causing forward and reverse scans. The scan rate is the slope (a or c). Single or multiple cycles can be used. If the reaction is reversible, there is very little difference between the first cycle and successive scans (Kissinger & Heineman, 1983; Mabbott, 1983).

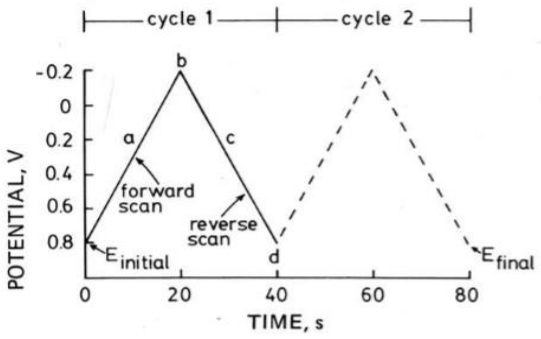

Figure 1.2 Typical excitation signal for cyclic voltammetry, a triangular potential waveform with switching potential versus the reference electrode. Reprinted with permission from Kissinger & Heineman (1983). Copyright 1983 American Chemical Society.

The current measured at the working electrode during the potential scan is the response signal. The current versus potential plot is known as cyclic voltammogram. A typical cyclic voltammogram for a platinum working electrode in an aqueous solution containing potassium ferricyanide ($K_3Fe(CN)_6$) as the electroactive species and potassium nitrate (KNO_3) as the supporting electrolyte is shown in Figure 1.3 (Kissinger & Heineman, 1983).

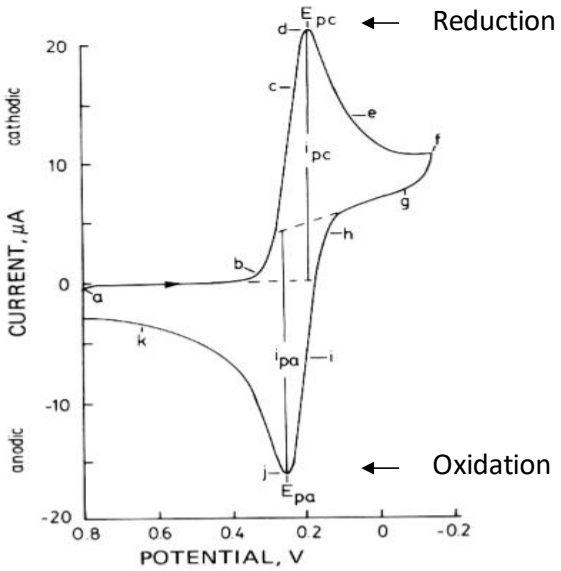

Figure 1.3 Typical cyclic voltammogram of ferrocyanide redox species. Reprinted with permission from Kissinger & Heineman (1983). Copyright 1983 American Chemical Society.

The initial potential applied is chosen to avoid any electrolysis of the $Fe(CN)_6^{3-}$ when the electrode is switched on. The potential is scanned negatively (forward scan) as indicated by the arrow and when the potential is sufficiently negative to reduce $Fe^{III}(CN)_6^{3-}$ (Reaction 1), a cathodic current appears as indicated at (b) (Kissinger & Heineman, 1983).

$$Fe^{III}(CN)_6^{3-} + e \longrightarrow Fe^{II}(CN)_6^{4-} \quad (1)$$

The cathodic current increases rapidly (b → d) until the concentration of $Fe^{III}(CN)_6^{3-}$ is depleted (current peak d) at the surface of the electrode and then decays (d → g) (Kissinger & Heineman, 1983). The current depends on two steps in the overall

process, the movement of electroactive material to the surface and the electron transfer reaction (Mabbott, 1983). As the electrolysis of the reactant depletes its concentration near the surface and the experiment is performed at a stationary electrode in an unstirred solution, diffusion is the principal means of moving the reactant to the surface (Mabbott, 1983). As the depletion zone grows and the average distance that the reactant molecules must travel to reach the surface increases, the rate of mass transport decreases (Mabbott, 1983). The dependence on mass transport, and the fact that a finite rate for the reverse electron transfer process is possible, prevent the current from increasing exponentially with potential (Mabbott, 1983). When the reaction becomes diffusion-limited, the current reaches a maximum and as the concentration gradient and the rate of mass transport continue to decrease, the current decays (Mabbott, 1983). When the scan direction is reversed and the electrode becomes a sufficiently strong oxidant, the reduced form is oxidized back to the original starting material (Reaction 2) causing anodic current (i → k) (Kissinger & Heineman, 1983; Mabbott, 1983). The anodic current rapidly increases until a low concentration of $Fe^{II}(CN)_6^{4-}$ at the surface causes the current to peak (j) and then decays (j → k) as the solution surrounding the electrode is depleted of $Fe^{II}(CN)_6^{4-}$. The first cycle is completed when the potential reaches the initial potential applied (Kissinger & Heineman, 1983).

$$Fe^{II}(CN)_6^{4-} \longrightarrow Fe^{III}(CN)_6^{3-} + e \qquad (2)$$

The reduction potential for the redox couple can be approximated as the average of the forward and return peak potentials, and is most accurate when the electron transfer process is reversible and the diffusion coefficients for the oxidized and reduced forms are the same (Kissinger & Heineman, 1983). The two peaks are separated due to the diffusion of the analyte to and from the electrode. If the reduction process is chemically and electrochemically reversible, the difference between the anodic and cathodic peak potentials, called peak-to-peak separation (ΔE_p), is 57 mV at 25 °C (Elgrishi et al., 2018). Reversible means that the reaction is fast enough to maintain the concentrations of the oxidized and reduced forms in equilibrium with each other at the electrode surface. The proper equilibrium ratio at a given potential is determined by the Nernst Equation (1) (Kissinger & Heineman, 1983).

$$E = E^0 - \frac{RT}{nF} ln\left(\frac{Red}{Ox}\right) \quad \text{(Eq. 1)}$$

Where E^0 is the standard redox potential, R is the gas constant, T is the temperature, n is the number of exchanged electrons, F is the Faraday constant, Ox is the concentration of the oxidized form and Red is the concentration of the reduced form. When there is a low barrier to electron transfer and the process is electrochemically reversible, the electron transfers are fast, and equilibrium is established immediately upon any change in applied potential. This processes follow the Nernst equation and are referred to as “Nernstian” (Elgrishi et al., 2018). By contrast, when there is a high barrier to electron transfer (electrochemical irreversibility), electron transfer reactions are sluggish and more

negative (or positive) potentials are required to observe reduction (or oxidation) reactions, giving rise to larger ΔE_p (Elgrishi et al., 2018). A system may look reversible at low scan rate but as the scan rate is increased, slow electron transfer kinetics can make the peak potentials shift farther apart in such a manner that they are no longer symmetric, being classified as quasi-reversible (Kissinger & Heineman, 1983). Estimating formal reduction potentials from quasi-reversible voltammograms is less reliable the farther the peak separation deviates from the reversible case. Reactions that yield products that cannot be recycled electrochemically to give back the original reactants (extensive bond breaking and/or loss of substituents to solution) are "chemically irreversible" reactions, and many yield no return peak at all (Kissinger & Heineman, 1983). Another characteristic of electrochemically reversible electron transfer processes involving freely diffusing redox species is the dependence of the peak height on the square root of the potential scan rate (v), depicted by the Randles-Sevcik in Equation (2) (Elgrishi et al., 2018; Kissinger & Heineman, 1983).

$$i_p = (2.69x10^5)n^{3/2}D^{1/2}CAv^{1/2} \quad \text{(Eq. 2)}$$

where the current of the peak on the cyclic voltammogram (i_p) will be in amperes, n is the number of transferred electrons in the redox reaction (equals to 1 for the example of the $Fe^{III}(CN)_6^{3-}$ above), the electroactive surface area (A) is in cm^2, D is the diffusion coefficient (6.70×10^{-6} cm^2/s), v is in V/s, and C is the molar bulk concentration of the electrolyte (Kissinger & Heineman, 1983). On biosensing studies, CV can be used to

understand the electrochemical behavior of the biosensors by the shape of their CV curves and determine their electroactive surface area through the Randles-Sevcik equation.

Electrochemical impedance spectroscopy (EIS) is a powerful technique for investigating electrochemical systems and processes due to its ability to determine multiple parameters from a single experiment and for being sensitive to different surface phenomena and changes of bulk properties (Dhillon & Kant, 2017; Lisdat & Schäfer, 2008). It is a high precision measurement technique which does not substantially remove or disturb the system from its operating condition (Dhillon & Kant, 2017). In the field of biosensors, EIS is particularly convenient to the detection of binding events on the transducer surface such as detection of biorecognition processes and surface modifications characterizations, e.g. immobilization of biomolecules on the transducer (Lisdat & Schäfer, 2008). This technique has the inherent potential for label-free detection, which is of special interest in bioanalysis as it circumvents the need to modify biomolecules with labels (such as fluorescence dyes, enzymes, redox or radioactive compounds) and its limitation with regard to achieving competitive and low-cost point-of-care applications (Garrote, Santos, & Bueno, 2019; Lisdat & Schäfer, 2008). In a typical biosensor application, the biological component is immobilized on the working electrode and the interaction with an analyte molecule is detected (Lisdat & Schäfer, 2008). The impedimetric term arises because the interface offers (upon the occupation of the receptive centers) an electronic impediment for charges to be transferred (Garrote et al., 2019). The electric impediment for an exchange of charge between the electrode and

the solution increases as a function of target binding to the interface, which allows the label-free biosensing (Garrote et al., 2019).

Impedance is a term used to describe how much effort (voltage, V, generally applied with a small amplitude) is required to produce a response (current, I) in electrical systems (Berney, 2004; Lisdat & Schäfer, 2008). Resistance is a measure of how much a system resists the flow of a direct current (DC) signal while impedance is the same measurement on an alternating current (AC) signal at a given frequency (Berney, 2004). In DC systems, only resistors impede current flow. However, in AC systems resistors, capacitors and inductors impede current flow and the total impedance is the combined contribution of all those elements (Berney, 2004). In an electrochemical cell, slow electrode kinetics, slow chemical reactions and diffusion can all impede electron flow, and can be considered analogous to the resistors, capacitors and inductors that impede the flow of electrons in an AC circuit (Berney, 2004). The impedance Z (Ω) is the quotient of the voltage–time function $V(t)$ and the resulting current-time function $I(t)$, as described by Equation (3).

$$Z = \frac{V(t)}{I\,(t)} = \frac{V_0 \sin(2\Pi f t)}{I_0 \sin(2\Pi f t + \phi)} = \frac{1}{Y} \qquad \text{(Eq. 3)}$$

where V_0 and I_0 are the maximum voltage (V) and current (A) signals, respectively, f is the frequency (Hz), t is the time (s), ϕ is the phase shift (rad) between the voltage-time and current-time functions, and Y is the complex conductance or admittance (S). The impedance is a complex value, since the current can differ not only in terms of the

amplitude, but it can also show a phase shift, ϕ, compared to the voltage-time function (Lisdat & Schäfer, 2008). In EIS, the response of the sample under test can be described by its impedance $Z = Z' + iZ''$', where Z' is the real and Z'' is the imaginary impedance components that originate mainly from the resistance and capacitance of the cell, respectively (Berney, 2004).

In EIS, the impedance is generally determined at different frequencies rather than just one, thus the name impedance spectroscopy (Lisdat & Schäfer, 2008). The impedance spectrum obtained allows the characterization of surfaces, ion diffusion, electron transfer rate, redox reactions, diffusion processes and double layer capacitances of electrochemical interfaces (Garrote et al., 2019). The two main requisites for using impedance spectroscopic methods in electrochemical biosensing are: 1) the platform interface must possess a linear response with respect to the perturbation, i.e., if the output signal is equivalently proportional to the amplitude of the input; and 2) be time-invariant during the acquisition of the spectrum, i.e., spectra do not vary in time for a given steady-state (Garrote et al., 2019). The requirement for linearity is easier to achieve in electrochemical interfaces than that for time-invariances. The linearity is generally achieved by how the users set the magnitude of the perturbation (small as possible is better in obtaining the desired linearity, though the ratio of signal-to-noise decreases). The time-invariance depends on the chemical stability at a particular steady-state, and the invariance of the interface under the conditions of the analysis (Garrote et al., 2019).

The EIS analysis of the interface can be conducted in the absence (nonfaradaic response) or in the presence of a redox probe (faradaic response) (Garrote et al., 2019). Redox-active compounds are commonly added to the analysis solution (ferri/ferrocyanide is often chosen) giving a faradic response and the changes in the barrier to redox conversion results in a well-defined charge transfer resistance (R_{ct}) (Garrote et al., 2019; Lisdat & Schäfer, 2008). If the redox-active compound is omitted or a blocking layer is applied to the electrode, rather capacitive impedance behavior will be observed (since R_{ct} will become extremely large) (Lisdat & Schäfer, 2008). Measurements performed in an inert electrolyte solution (non-faradaic response) usually result in a much higher impedance, but as long as the impedance changes that take place during the biorecognition process are reproducible, this kind of measurement can also result in reliable data (Garrote et al., 2019; Lisdat & Schäfer, 2008). The data can be presented in a Bode plot that shows the logarithm of the impedance magnitude as a function of the logarithm of frequency (Figure 1.4a). For faradic responses, the impedance spectrum can also be analyzed using an equivalent circuit, usually a Randles circuit, as shown in Figure 1.4b, for the situation of an electrode in contact with an electrolyte, comprising the solution resistance (Ω), R_s, the charge transfer resistance (Ω), R_{ct}, the double layer capacitance (μF), C_{dl}, and the Warburg impedance ($\Omega\ s^{1/2}$), W. In the Nyquist plot (imaginary impedance versus real impedance) shown in Figure 1.4c, the values for R_s and R_{ct} can be easily determined (Lisdat & Schäfer, 2008). The R_{ct} accounts for the electron transfer (redox reaction) occurring between the redox probe and the electrode, and the W accounts for a diffusional process associated with a limited-

diffusional transport process due to the mass transport of the redox probe species from the bulk of the electrolyte to the interface of the electrode (Garrote et al., 2019). A binding event at the electrode can be detected by following the change in R_{ct} or the change in impedance in the case of faradic and non-faradic responses, respectively, and both have been used in biosensing applications (Garrote et al., 2019; Lisdat & Schäfer, 2008).

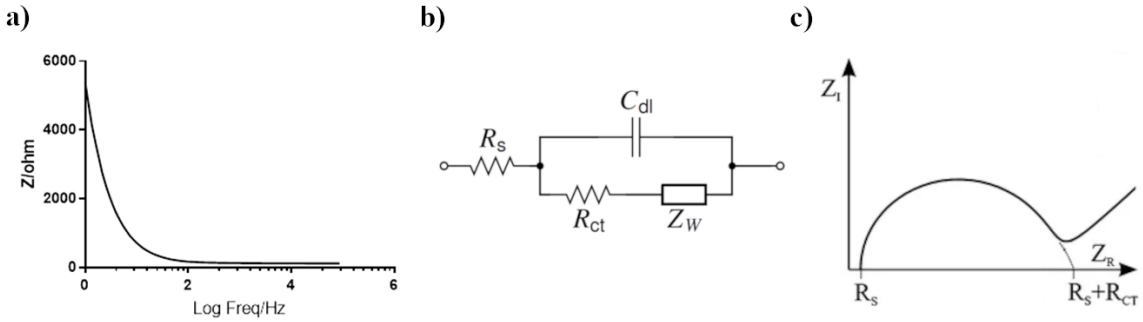

Figure 1.4 a) Representative of Bode plot adapted from Lvovich (2012). b) Depiction of Randles equivalent circuit. c) Typical Nyquist plot of mixed kinetic and charge-transfer control systems (Randles equivalent circuit) adapted from Lisdat & Schäfer (2008).

CHAPTER II RAPID AND LABEL-FREE *LISTERIA MONOCYTOGENES* DETECTION BASED ON STIMULI-RESPONSIVE ALGINATE-PLATINUM THIOMER NANOBRUSHES

2.1. Introduction

Listeria monocytogenes is a virulent foodborne bacterium ubiquitous in the environment that causes hundreds of deaths in the US annually (FDA, 2012; V. S. Somerset, 2011). Every year, nearly 48 million cases of foodborne illness are reported, nearly 19% of which are due to infection with *Listeria monocytogenes*, having potentially a $15 billion negative economic impact from healthcare costs, lost productivity, and loss of life (Hoffmann et al., 2015; USFDA, 2016). *L. monocytogenes* is among the deadliest of foodborne pathogens, with a fatality rate of up to 30% in high-risk individuals (Frye et al., 2002; Ramaswamy et al., 2007). It is particularly dangerous for pregnant women, although they generally recover, their babies may not survive (FDA, 2012). This pathogen is very difficult to monitor in food processing environments due to its ability to proliferate under low moisture content, high salinity conditions, or at temperatures associated with common refrigerator/freezer units (Noordhout et al., 2014). A zero-tolerance rule for *L. monocytogenes* in ready-to-eat foods was implemented by the U.S. Food and Drug Administration (FDA), the United States Department of Agriculture (USDA), and the European Union (EU) (V. S. Somerset, 2011) compounded with the increasing number of food recalls related to *Listeria* contamination in recent

years (FDA, 2021) further reinforces the need for real-time pathogen detection methods that can identify contaminated food products before reaching the public.

Food manufacturers expend tremendous resources on Hazard Analysis Critical Control Points (HACCP) strategies to ensure that their intervention methods are efficacious. But the current state-of-the-art for detecting *Listeria* in food processing plants, such as total viable counts (TVC), polymerase chain reaction (PCR), and enzyme-linked immunosorbent assays (ELISA) are susceptible to errors and false readings, and require costly laboratory settings with highly-trained personnel to complete (Lavecchia, Tibuzzi, & Giardi, 2010; Velusamy et al., 2010). Test results from these methods are severely delayed by requiring two consecutive enrichment steps (up to 48 h) to concentrate/amplify bacteria prior to a qualitative detection step (Hitchins, Jinneman, & Chen, 2017), because these methods lack sensitivity (~100 CFU/mL limits of detection (LOD)) (Vanegas, Claussen, et al., 2017; Vanegas et al., 2016) and cannot directly detect low levels of pathogens in complex samples such as media, broth, or homogenized tissue. Even with strict adherence to HACCP plans and environmental test protocols, *Listeria* outbreaks still occur in the population, forcing food recalls. In fact, the FDA reported 226 products recalls due to potential contamination with *Listeria* in 2020 (FDA, 2021). The consequent public health impacts and economic losses resulting from these recalls and disease outbreaks motivate a substantial effort to develop faster and more economical techniques for detecting foodborne pathogens in food. Rapid and accurate detection would allow food manufacturers to test more frequently and thereby meet the goals of pathogen reduction programs.

Electrochemical sensing techniques provide the ability to rapidly and sensitively detect bacteria (L. Yang & Bashir, 2008). Electrochemical devices can circumvent the challenges associated with fluorescence/optical-based sensors. Optical sensors require complex equipment/processes (e.g., fluorescence microscopes, pre-labeling steps) and can be impeded by turbid, optically dense, biological samples that often contain autofluorescent molecules such as calcium that cause noise (Baraket et al., 2017). These properties are important to consider for the analysis of food and environmental samples in a processing facility where user-friendly devices and simple sample preparation are required (McLamore et al., 2021; Mclamore et al., 2019; Valderrama et al., 2016). The deposition of metal particles and/or polymers at the surface of a biosensor is known to significantly enhance surface area and electrical conductivity, in addition to improving biorecognition agent immobilization, resulting in higher sensitivity, faster capture and improved detection of the target bacteria (Burrs et al., 2015). Nanoplatinum presents favorable electrocatalytic properties for sensing and its use has been shown to increase the electroactive surface area, enhancing sensor sensitivity, response time, and limit of detection (Hrapovic, Liu, Male, & Luong, 2004; Taguchi et al., 2016).

Aptamers are single-stranded oligonucleotides and, if selected properly and applied in the correct binding buffer, show high affinity toward targets (Acquah, Agyei, Monney, Pan, & Danquah, 2018). Aptamers bind specifically via interactions of target(s) and exposed structures, commonly loops (Acquah et al., 2016; Teng et al., 2016). In some cases aptamer-based sensors (i.e., aptasensors) have shown ultra-low detection limits (femto- to picomolar) (Y. Chen, Xiang, Liu, & Chen, 2020). High affinity

secondary structures (commonly in the range of ten to a few hundred nucleotides) are typically synthesized by an iterative selection assay called SELEX (Systematic Evolution of Ligands by Exponential Enrichment). Aptamers have numerous advantages over antibodies, including low synthesis cost, high reproducibility, high thermal stability, and ability to modify and/or integrate various tags or functional groups (e.g., biotinylation, thiolation, etc.) (Acquah et al., 2016; Tan et al., 2016). Use of aptamers can greatly increase the selectivity of the sensor relative to other strategies, but this approach usually depends on co-immobilization with nanomaterials for signal amplification (Y. Lin et al., 2020). Among these nanomaterials, hybrid metallic-nanocarbon composites have shown improved stability and electron transport, consequently resulting in improved electrochemical signal transduction and sensor performance (Walcarius, Minteer, Wang, Lin, & Merkoçi, 2013). Comprehensive reviews on aptamer-based technologies for foodborne pathogen detection summarize recent developments in optical and electrochemical biosensors (i.e., aptasensors) (Kärkkäinen et al., 2011; Teng et al., 2016; Torres-Chavolla & Alocilja, 2009), including platforms that use magnetic beads conjugated to DNA aptamers and antibody-aptamer functionalized fiber-optic sensor for target detection of *L. monocytogenes* cells from contaminated ready-to-eat meat products (Ohk, Koo, Sen, Yamamoto, & Bhunia, 2010). Hills et al. (2018) reported a sensing mechanism for rapid detection of *L. monocytogenes* in food samples using the actuation of chitosan-aptamer nanobrush using the aptamer discovered by Ohk et al. (2010). Recently, Sidhu et al. (Sidhu et al., 2020) developed an aptasensor using platinum interdigitated microelectrodes functionalized with this same

DNA aptamer for *Listeria* spp. detection in vegetable broth and hydroponic media by incorporating the sensor into a particle/sediment trap for real-time analysis of irrigation water.

The use of stimuli-responsive polymers for actuation in sensing applications has gathered increasing attention in recent years as summarized in a recent review by Hu, Zhang, Li, & Serpe (2019). Stimuli-responsive polymers undergo major changes in solubility, volume, and/or conformation in response to external stimuli, and have been used to mimic naturally occurring responsivity to external changes on the environment that is observed in living systems (i.e., biomimetic) (Hu et al., 2019). Stimuli-responsive polymers can exhibit significant changes in the swelling behavior of the network structure expanding and collapsing at pH values above or below their pK_a (Ju, Kim, & Lee, 2001; López-León, Carvalho, Seijo, Ortega-Vinuesa, & Bastos-González, 2005). Sodium alginate is a natural biodegradable, biocompatible, non-toxic and low-cost polysaccharide isolated from brown algae, containing repeating mannuronic and guluronic acids. This polymer is an anionic molecule with pKa of approximately 3.5. Above the pKa, alginate is hydrophilic and in environments that are below this pH it is hydrophobic (Cheong & Zhitomirsky, 2008; Reddy et al., 2007). Previous works have used polymer actuation for improving bacteria capture (A. Liu et al., 2009) and more recently Hills et al. (2018) and Giacobassi et al. (2021) used actuation of stimuli-responsive polymers for both capture and sensing of pathogens in complex media. These studies successfully demonstrated that by controlling polymer actuation at the microscale, pathogens can be captured when the polymer is extended, and signal

transduction is improved after collapsing the polymer at the sensor surface (Giacobassi et al., 2021; Hills et al., 2018). However, these previous studies used metals nanoparticles and polymers in a layer-by-layer deposition to produce the sensors (Hills et al., 2018; Z. Wang et al., 2014), which required a multi-step fabrication process. One of the biggest challenges in these previous works was tethering the nanobrush to the surface followed by biofunctionalization. Use of crosslinking techniques (e.g., homobifunctional crosslinking with glutaraldehyde) are non-specific, and control of the degree of surface tethering versus bioreceptor immobilization is challenging.

Herein, the focus of this study was to develop of a one-step co-electrodeposition of alginate thiomers (thiolated alginate) and nanoplatinum as an aptasensor platform. A unique alginate thiomer (ALG-thiomer) with platinum platform was built to develop a rapid, label-free and high-performance biosensor to detect *L. monocytogenes.* This is the first report of thiomers used in sensing applications, which opens a new and exciting area of research for nano-biosensor development. Previous studies have shown co-electrodeposition of alginate and other conductive material such as graphite and MnO_2-C (X. Chen, Yan, Sun, Shi, & Zhang, 2019; Vigués, Pujol-Vila, Marquez-Maqueda, Muñoz-Berbel, & Mas, 2018), but this work was the first to show simultaneous electrodeposition of ALG-thiomers and platinum for biosensing. In addition to testing this ALG-thiomer platform for small molecule sensing (cationic, anionic and neutral redox compounds), it was also shown its ability to incorporate aptamers for pathogen detection. To achieve this goal the alginate was modified to present a thiol termination, which presents good metal binding properties, allowing the adsorption of the platinum

nanoparticles directly to the polymer. The ALG-thiomer deposition conditions were optimized under different combinations of voltage, ALG-thiomer concentration and sonoelectrodeposition cycles, achieving up to 7-fold increase in the electroactive surface area for the best condition (5.75 V / 140 sonoelectrodeposition cycles / 0.05% w/v ALG-thiomer). Next, the actuation of the ALG-thiomer/Pt nanobrushes was tested at pH values below and above the pKa of alginate for small molecule sensing. Following this testing, aptamers specific to *Listeria* were tethered to the nanobrush, and cell capture strategies were investigated for ALG-thiomer/Pt aptasensing. The results showed that the highest signal-to-noise ratio was achieved when cell capture occurred in the extended brush conformation (pH > 3.5) and the sensing in the collapsed brush conformation (pH < 3.5). Finally, it was demonstrated that the ALG-thiomer/Pt nanobrush biosensor can selectively detect *L. monocytogenes* in a food matrix in concentrations as low as 5 CFU/mL and in the presence of other Gram-positive cells under 17 min without the need for sample preconcentration or redox labeling techniques.

2.2. Materials and methods

2.2.1 Materials

Platinum/iridium working electrodes (Pt/Ir, BASi MF-2013, 1.6 mm diameter, 7.5 cm length), and reference (Ag/AgCl) and Pt auxiliary electrodes were purchased from BASinc (West Lafayette, IN). Chloroplatinic acid 8% (w/w), hydroquinone ($C_6H_4(OH)_2$, hexaammineruthenium(III) chloride ($Ru(NH_3)_6Cl_3$,) potassium phosphate monobasic, and sodium phosphate dibasic were purchased from Sigma-Aldrich Co. (St.

Louis, MO). Polycrystalline diamond suspensions (1 µm and 3 µm) and alumina slurry (0.05 µm) were obtained from Buehler (Lake Bluff, IL). Lead acetate ($Pb(C_2H_3O_2)_2$) (30% w/v) was purchased from Fisher Scientific (Pittsburgh, PA). Potassium ferrocyanide trihydrate ($K_4Fe(CN)_6.3H_2O$) was purchased from Ward's Science (Rochester, NY). Potassium ferricyanide ($K_3Fe(CN)_6$) and cysteine hydrochloride monohydrate were obtained from J.T. Baker (Phillipsburg, NJ).

Sulfo-SMCC (sulfosuccinimidyl 4-(N- maleimidomethyl)cyclohexane-1-carboxylate) and 1-ethyl-3-(3-dimethylaminopropyl)carbodiimide HCl (EDC) were obtained from Thermo Fisher Scientific (Waltham, MA). N-Hydroxysuccinimide (NHS), 2-(morpholino)ethanesulfonic acid) (MES) buffer, Ellman's reagent (5,5'-dithiobis-(2-nitrobenzoic acid)), alginic acid sodium salt (low viscosity) and platinum wire (99.95% Pt, 1.5 mm dia.) were obtained from Alfa Aesar (Ward Hill, MA). DiaEasy™ dialysis tubing (3.5 kDa MWCO) was purchased from Biovision (Milpitas, CA). *L. monocytogenes* aptamers developed by Ohk et al. (2010) that target Internalin A (47 DNA bases, $K_D = 10^3$ CFU/mL, Mw 15,008 g/mol) were purchased from Gene Link Inc. (Hawthorne, NY). Commercially sterilized vegetable broth was purchased from a local grocery store. Tryptose phosphate broth (TPB) was bought from HiMedia (Mumbai, India). Tryptic soy broth (TSB), tryptic soy agar (TSA), yeast extract, and buffered peptone water (BPW) were purchased from Becton, Dickson and Company (Sparks, MD). Potassium nitrate (KNO_3) was purchased from British Drug Houses (ON, Canada). Tris EDTA (TE) buffer pH 7.4 was purchased from Quality Biological

(Gaithersburg, MD). Sodium chloride (NaCl) and potassium chloride (KCl) were acquired from EMD Millipore Corporation (Burlington, MA).

2.2.2 Bacteria cultures

Listeria monocytogenes (ATCC 15313) and *Staphylococcus aureus* (ATCC 25923) were used as target and interferent bacteria, respectively. These are pathogenic microorganisms and must be handled using biosafety level 2 standards established by the National Institute of Health. Resuscitation from frozen culture used two identical consecutive transfers to TPB for *L. monocytogenes* and TSB for *S. aureus* and incubation at 35 °C for 24 hours under aerobic conditions. Bacteria were maintained on tryptic soy agar (TSA) and TSA with 0.6% (w/v) yeast extract (TSAYE) slants for *S. aureus* and *L. monocytogenes*, respectively, and stored at 4°C for no more than 3 months. Total aerobic plate counts were measured in triplicate by serially diluting samples of the bacteria in BPW and plating on TSA and TSAYE for *S. aureus* and *L. monocytogenes*, respectively.

2.2.3 Nanobrush fabrication

2.2.3.1 Thiomer fabrication

Sodium alginate was modified to incorporate a thiol group termination by amide bond formation between carboxylic acid groups of sodium alginate and primary amino groups of cysteine using carbodiimide mediated coupling as in Jindal, Wasnik, & Nair (2010). In this method, the carboxyl groups of the alginate are activated with EDC at pH

6 for 45 min. Then, cysteine hydrochloride monohydrate was added in a weight ratio of 2 : 1 (alginate : cysteine) and allowed to react for 2 h at pH 4 followed by another 1 h at pH 6. The reaction was performed under continuous stirring at room temperature. Next, the solution was dialyzed (molecular weight cut-off 3.5 kDa) to isolate the alginate-cysteine conjugate (ALG-thiomer). The dialysis included two days against 1 mM HCl (pH 4), followed by 1 day in 1 mM HCl and 1% (w/v) NaCl, and another two days in 1 mM HCl (all the solutions were exchanged twice a day). Subsequently, the suspension was freeze-dried (-50 °C, -0.120 mBar, 48 h) in a Labconco FreeZone 6 unit (Labconco, Kansas City, MO, USA). ALG-thiomers were subsequently stored under nitrogen atmosphere at 5 ^{o}C until use for sensor modification.

The degree of modification achieved on the alginate was determined by quantifying the amount of thiol groups through Ellman's analysis according to instruction from Thermo Scientific (2011). Briefly, the samples and the Ellman's reagent (5,5'-dithiobis-(2-nitrobenzoic acid)) were mixed in a reaction phosphate buffer containing EDTA (ethylenediamine tetraacetic acid) at pH 8 and their absorbance was measured at 412 nm against a blank control (Genesys 10S UV-Vis Spectrophotometer, Thermo Scientific, Waltham, MA). The thiol concentration was calculated through the correlation with a standard curve of cysteine hydrochloride monohydrate.

2.2.3.2 ALG-thiomer/Platinum nanobrush deposition

Alginate and platinum were simultaneously deposited (Figure 2.1) on the surface of platinum/iridium working electrodes (previously polished according to manufacturer

instructions) using the sonoelectrodeposition method developed by Taguchi et al. (2016). In this method, the applied potential and sonication are alternated in cycles of 1 second each. A platinum wire (positive or anode) and the working electrode (negative or cathode) were connected to the power supply and submerged in the deposition solution. The deposition solutions were composed of 0.72% (w/v) chloroplatinic acid, 0.001% (w/v) lead acetate and ALG-thiomers at different concentrations (0.05, 0.075 and 0.1% w/v). Voltages of 1.5, 5.75 and 10 V for 60, 100 and 140 sonoelectrodeposition cycles were also evaluated to determine the optimal deposition conditions.

2.2.4. Material characterization

The optimized brush deposition morphology was observed through field emission scanning electron microscopy (SEM) images using a FEI Quanta 600 FEG (Hillsboro, OR). The electrode modified with ALG-thiomer/Pt brushes was first coated with a 5-nm thick layer of platinum using a Cressington sputter coater 208 HR (Watford, United Kingdom) and allowed to ventilate for 30 min prior to SEM imaging. Magnification of 10,000 and 16,000 times with accelerating voltage of 10 kV were used for the surface imaging.

The surface chemistry of the electrodes coated using the selected optimized brush deposition was analyzed by X-ray photoelectron spectroscopy (XPS), also known as electron spectroscopy for chemical analysis (ESCA). XPS was performed in an Omicron ESCA+ (Scienta Omicron, Sweden) equipped with a Mg/Al dual X-ray gun and CN10 electron gun.

2.2.5. Electrochemical characterization and actuation testing

Each step of the biosensor preparation (alginate-platinum deposition, aptamer loading and bacteria detection) was electrochemically characterized using a 3-electrodes cell system with a platinum auxiliary electrode and a Ag/AgCl reference electrode at room temperature using cyclic voltammetry (CV) and/or electrochemical impedance spectroscopy (EIS) methods as described by Burrs et al. (2015) using a CHI 600E potentiostat/impedance analyzer. CV test was conducted in a 4 mM $Fe(CN)_6^{3-}$ in 1 mM KNO_3 solution with a 10 sec quiet time, a 650 mV switching potential and 50, 100, 150, and 200 mV/s scan rates. CV was used to obtain the electroactive surface area (ESA in cm^2) of the electrodes via Randles-Sevcik theory using the slope of the current versus the square root of scan rate (i_p versus $v^{1/2}$), as previously reported (Taguchi et al., 2016; Vanegas et al., 2014). The ESA values were used to determine the best deposition parameters (ALG-thiomer concentration, voltage and number of sonoelectrodeposition cycles, as described in 2.3.2.), as well as to characterize brush actuation, and to determine aptamer loading concentration (see Appendix A for details).

For the actuation tests, a negatively charged probe ($KFeCN_6^{3-}$), a neutral probe ($C_6H_4(OH)_2$), and a positively charged probe $Ru(NH_3)_6^{3+}$ were used. The pH of the redox probe solution was adjusted to pH 7 or pH 3 using a 1 M HCl or NaOH solution. The pH of the redox solution was monitored during the CV tests to ensure reported pH did not change by more than 0.5 pH units. Actuation tests were also carried out in the presence of a constant background *Listeria* concentration of 10^3 CFU mL^{-1} in phosphate

buffer saline (PBS) using EIS to determine the most efficient capture and measurement strategy between extended and collapsed conformation of the brushes.

2.2.6. Pathogen sensing

EIS was used to determine the limit of detection (LOD), sensitivity and range of detection of the biosensor when exposed to bacteria at concentrations varying from 10^1-10^6 CFU mL^{-1} (standard curve). For functionalization procedure of ALG-thiomer/Pt brushes with aptamers, see Appendix A for the details. The analysis was performed with a frequency range of 1-1000,000 Hz, AC amplitude of 100 mV and initial DC potential of 0 V. Sensitivity testing was initially performed in PBS and then again in commercially sterile vegetable broth. Change in impedance ($\Delta Z = Z_{bacteria} - Z_{no\ bacteria}$) was determined from Bode plots (impedance vs. frequency) and used to obtain the calibration curve consisting of the change in impedance (Ohm) vs. the concentration of cells (log CFU mL^{-1}) at fixed cutoff frequency. Sensitivity to the target bacterium was obtained by slope of the linear portion of the calibration curve ($R^2 > 0.98$) and the limit of detection (LOD) was calculated using the 3σ method (Giacobassi et al., 2021). Selectivity to *L. monocytogenes* was evaluated by determining sensitivity and LOD in the presence of equal background concentration of another Gram-positive bacteria (*S. aureus*) in PBS and in sterile vegetable broth.

2.2.7. Statistical analysis

All experiments were performed in triplicate as independent experiments and results were expressed as mean ± standard deviation. Statistical analysis was performed using SPSS Software. One-way analysis of variance ANOVA was used to test for significance. Statistical significance was expressed at the $p < 0.05$ level; significantly different means were separated by the Tukey test.

2.3. Results and discussion

2.3.1. Nanobrush material characterization and morphology

The ALG-thiomer reaction efficiency was first evaluated by Ellman's analysis. The result obtained was 1050 ± 200 μmol of thiol groups g^{-1} of polymer, about 3 times higher than the thiol content of 324.54 μmol g^{-1} presented by Jindal et al. (2010) with a similar procedure. In the approach used in this work, EDC (a carbodiimide compound) reacted with carboxylic acid groups of the alginate to form an active O-acylisourea intermediate that was replaced by the primary amino groups of the cysteine, forming an amide bond with the original carboxyl group (see Figure 2.1). N-hydroxysuccinimide (NHS) can be included in the reaction to improve efficiency as the EDC couples NHS to carboxyls forming a NHS ester that is considerably more stable than the O-acylisourea intermediate (Thermo Scientific, 2012). Marcano & Sabino (2018) reported a higher value of 1939 μmol g^{-1} of thiol groups by including NHS on the activation reaction with EDC. However, this approach introduced additional functional groups which can cross link, reducing the ability to control brush actuation and introducing experimental error.

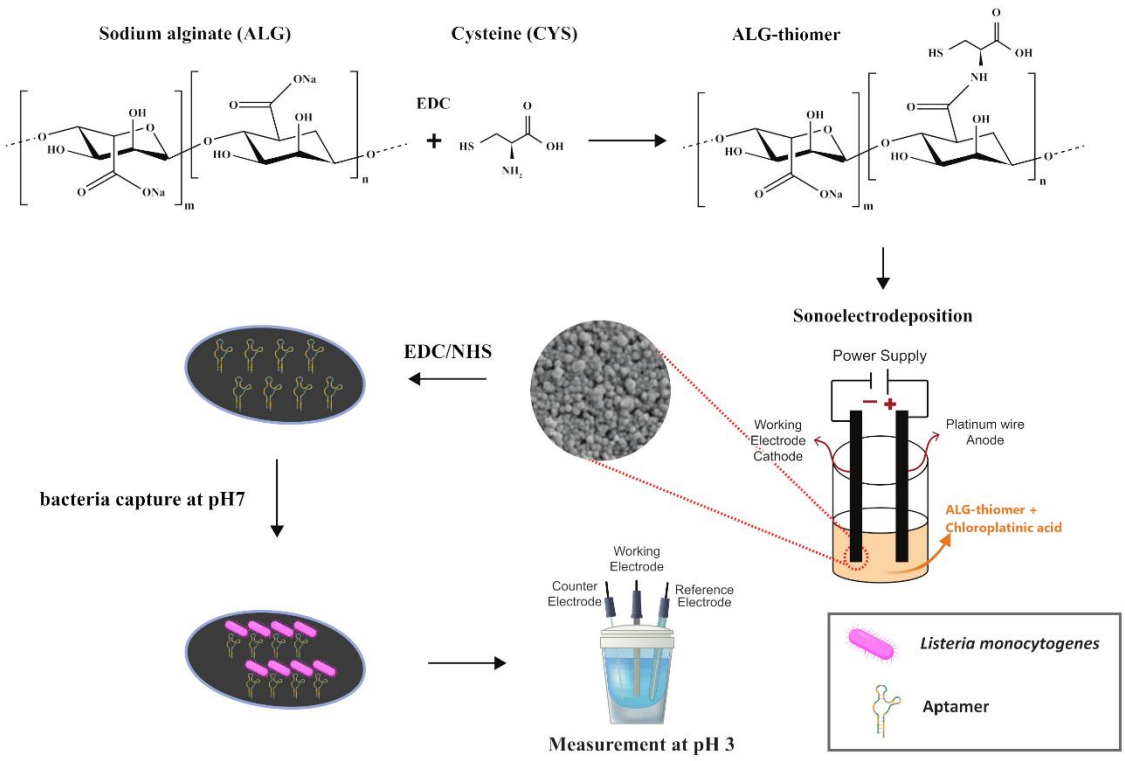

Figure 2.1 Fabrication, biofunctionalization, and sensing scheme of the ALG-thiomer/Pt brushes functionalized with aptamer selective to *L. monocytogenes*. First, ALG-thiomers are formed based on the reaction of sodium alginate with cysteine using N-(3-Dimethylaminopropyl)-N′-ethylcarbodiimide (EDC) chemistry. Then, ALG-thiomer and platinum are sonoelectrodeposited simultaneously onto the working electrode, resulting in ALG-thiomer/Pt brushes that are shown via SEM imaging. Next, the ALG-thiomer/Pt brushes were functionalized with aptamer via carbodiimide crosslinking chemistry. Sensing strategy consisted of ALG-thiomer/Pt brush actuation from collapsed to extended states based on pH changes: bacteria capture was performed at pH 7 with brushes in the extended state followed by measurement (sensing) when brushes are collapsed at pH 3.

The presence of the thiol group in the Ellman's analysis indicates that sulfur is present in the sample but does not provide information about the state of the sulfur (reactive sulfhydryl group or oxidized) as the thiol group is very susceptible to oxidation upon exposure to atmospheric oxygen with possible disulfide-like bond or cross-link (-S-

S-) formation (Marcano & Sabino, 2018). XPS analysis was performed to characterize the chemical bonds. XPS spectrum of the ALG-thiomer/Pt brush deposition (Figure 2.2a) shows the effective deposition of both ALG-thiomer and Pt components, with characteristic peaks of C 1s, O 1s, N 1s and S 2p from ALG-thiomer and Pt 4f from platinum. The N 1s peak at 399 eV fall within the range for cysteine-metal complexes (Srinivasan, Stiefel, Elsberry, & Walton, 1979). The binding energy of 400 eV can be associated with the presence of amine group (Z. Wang et al., 2014) or with the cysteine (Moulder, Stickle, Sobol, & Bomben, 1992). The S 2p binding energy of 164 eV (Figure 2.2b) is characteristic of thiol (Thermo Scientific, 2021) or its coordination to the metal ions (Srinivasan et al., 1979). The peak at 162.5 eV (S 2p) is also within the range expected for metal-sulfur bonds (Thermo Scientific, 2021). B. Yang & Agrios (2018) associated a doublet in the S 2p region of a Pt modified 4-mercaptobenzoic acid at slightly lower values (161.84 eV and 163.04 eV) than the obtained in the present work (162.5 eV and 164 eV) to the formation of a Pt-S bond. Castner, Hinds, & Grainger (1996) also reported the binding energy of 161.9 eV as consistent with the sulfur atoms bound to the gold surface as a thiolate species. The S 2p peak in the neighborhood of 168.5 eV might be due to the presence of oxidized sulfur (Srinivasan et al., 1979; B. Yang & Agrios, 2018). The Pt 4f spectrum (Figure 2.2c) presents two peaks at 71 eV and 74.3 eV corresponding to S-bonded Pt, which is consistent with literature reports for Pt in contact with S atoms (Kwon et al., 2011; B. Yang & Agrios, 2018). Romanchenko, Likhatski, & Mikhlin (2018) assigned the binding energy of 71.5 eV to Pt^0 metallic nanoparticles and 74 eV to Pt(IV)-S compounds, which could also be the case in the

present study as: 1) Pt could be depositing directly onto the electrode's surface as well as binding to ALG-thiomer before depositing, and 2) the electrodeposition using chloroplatinic acid involves Pt(IV) cations and its reduction to Pt^0 (Yasin, Denuault, & Pletcher, 2009). Overall, the XPS spectra shown in Figure 2.2 indicate bonding between the Pt nanoparticles and the S atoms in the ALG-thiomer.

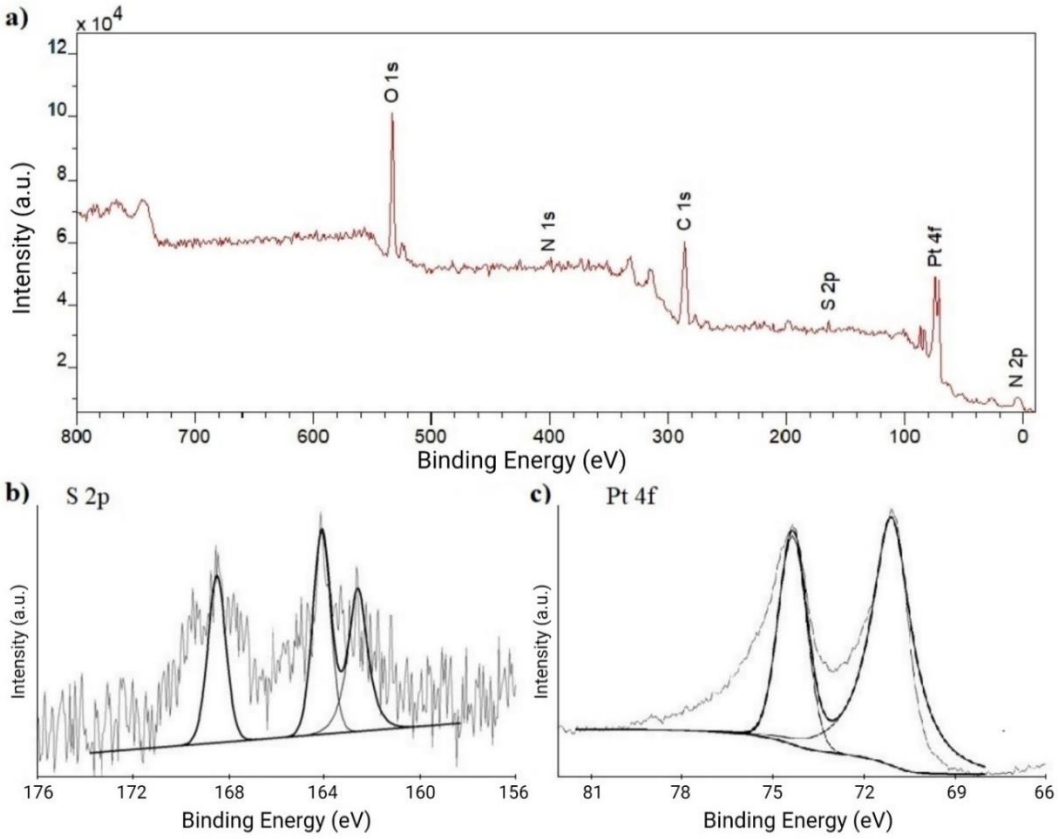

Figure 2.2 X-ray photoelectron spectroscopy (XPS) analysis. a) survey spectrum, b) S 2p spectrum, and c) Pt 4f spectrum showing the successful co-deposition of both ALG-thiomer and Pt onto electrodes.

The morphology of the nanoplatinum and alginate brushes is shown in Figure 2.3. The ALG-thiomer/Pt brush deposition formed juxtaposed spheroids (brush terminal

nodes) with diameters ranging from 80 to 400 nm with a uniform coating with some random cauliflower shape structures distributed throughout the surface. Similar, although smoother, structure was presented by X. Chen et al. (2019) when simultaneously electrodepositing alginate and MnO_2-C composite. Also, similar spheroid structure although more porous and tridimensional was shown by Giacobassi et al. (2021) with the deposition of PNIPAAm brushes over reduced graphene oxide and platinum layers. Similarly to PNIPAAm brushes described by Giacobassi et al. (2021), the electrodeposition of ALG-thiomer/Pt brushes led to homogeneous brush formation with uniform shaft and node sizes distribution. According to Taguchi et al. (2016), the pulsed sonoelectrodeposition method promotes increased mass transfer to the electrode surface which results in uniform material deposition. The relatively large and smooth structures obtained in the present work are expected since the co-deposited ALG-thiomer complex is a significantly large polymeric material, which was also observed by Giacobassi et al. (2021).

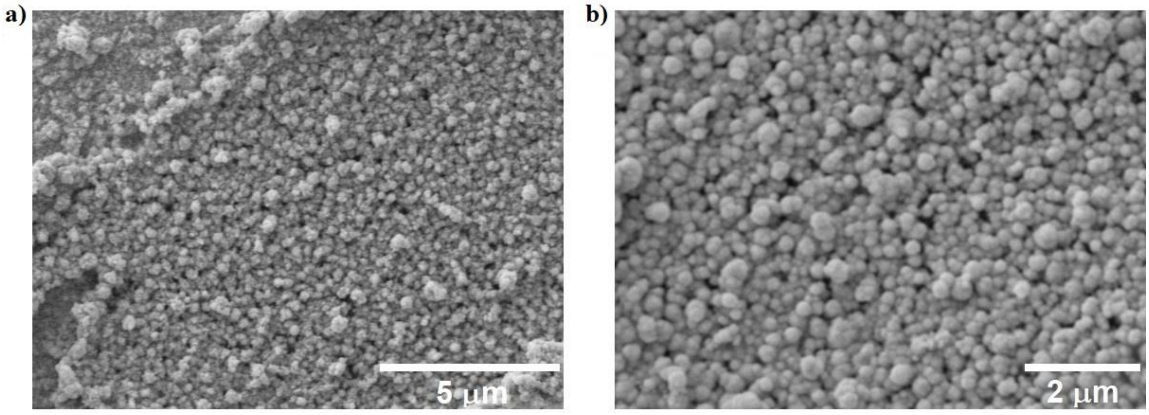

Figure 2.3 SEM images of ALG-thiomer/Pt brush at 10 kV and a) 10,000, and b) 16,100 times magnification, respectively, showing a uniform brush formation and deposition over the electrode surface with terminal nodes ranging between 80 to 400 nm in diameter.

2.3.2. Electrodeposition optimization

During co-deposition of ALG-thiomer and metal, Pt(IV) ions in suspension (Yasin et al., 2009) bind the ALG-thiomer complex and still have charges to be neutralized at the cathode. The electrodeposition of alginate is normally anodic, based on dissociation of sodium alginate forming anionic alginate species followed by its neutralization into alginic acid (H-Alg) due to a localized low pH at the anode (Cheng et al., 2011; Cheong & Zhitomirsky, 2008; Z. Wang et al., 2014). On the other hand, the platinum deposition is cathodic, as the applied direct current induces migration of positively charged platinum ions and subsequent nanoparticle formation on the electrode surface (Grainger & Blunt, 1998). In the present work, both methods were tested, and the cathodic deposition was selected, as no Pt deposited with anodic deposition. Thereby, the incorporation of cysteine to the alginate to provide a thiol termination

facilitated simultaneous cathodic deposition, which was the root of the one-step process applied here.

For optimization of ALG-thiomer/Pt brush deposition on electrodes, three parameters were evaluated using cyclic voltammetry (CV): deposition voltage, deposition time, and polymer concentration. Figure 2.4a shows representative CV curves of the best condition for the ALG-thiomer/Pt brush deposition compared to the curves of the bare Pt/Ir electrode and a dropcoated ALG-thiomer electrode. All treated electrodes demonstrated quasi-reversible redox couples with well-defined redox peaks indicating that the reaction was diffusion controlled at the interface of the electrode-solution (Vanegas et al., 2014). No significant change in current peak value ($p < 0.05$), and consequently on ESA value was observed when ALG-thiomer was dropcoated onto the electrode's surface, which indicates that the presence of thiol groups did not promote sufficient direct attachment of ALG-thiomer to the electrode's surface. Figure 2.4b presents a comparison among ESA values with the different deposition parameters. All conditions resulted in significantly higher ESA values ($p < 0.05$) than the bare electrodes (0.028 ± 0.003 cm^2), indicating that coating the electrodes with ALG-thiomer/Pt brush improves electron transport at the electrode surface. The best condition (5.75 V / 140 cycles / 0.05% w/v ALG-thiomer), increased the ESA value by 7 times from the bare electrode, to 0.20 ± 0.03 cm^2.

An increase in material deposition with increasing time was reported for both platinum (Taguchi et al., 2016) and alginate (Cheong & Zhitomirsky, 2008) but in both cases only one voltage was applied. Other authors also presented increasing deposition

of alginate with time and current density (Cheng et al., 2011; Kingsley, Capuano, & Corr, 2019; Ozawa, Ino, Takahashi, Shiku, & Matsue, 2013; W. Wan, Dai, Zhang, & Shen, 2015). In the present work, the combination of voltage and deposition time presented the best effect on the brush deposition. Even though two of the conditions tested were similar ($p > 0.05$), 5.75 V/ 140 cycles / 0.05% (w/v) ALG-thiomer was chosen for further experiments since: 1) the response surface analysis indicated the best voltage range between 5 V and 8 V; and 2) with 10 V/ 140 cycles/ 0.075% (w/v) ALG-thiomer some "overgrowth" (deposition beyond the working diameter of the electrode) was observed. Taguchi et al. (2016) also reported overgrowth with pure Pt sonoelectrodeposition over 180 seconds considering it to not be stable as it might flake off when immersed in solution. The same authors reported ESA value of 0.3 cm^2 when depositing nanoplatinum at 10 V for 180 seconds using the same pulSED technique (Taguchi et al., 2016). The lower ESA value (0.20 ± 0.03 cm^2) obtained in the present work, despite the longer deposition time (280 seconds), was probably due to steric hindrance to more platinum deposition caused by the presence of the ALG-thiomer material in addition to alginate being a non-conductive material. Besides the steric hindrance, a direct comparison between the sole deposition of platinum or alginate to this work might not be valid as this was a simultaneous deposition of both, done cathodically, while sole alginate electrodeposition is usually anodic, and the alginate was modified to incorporate cysteine for a thiol termination.

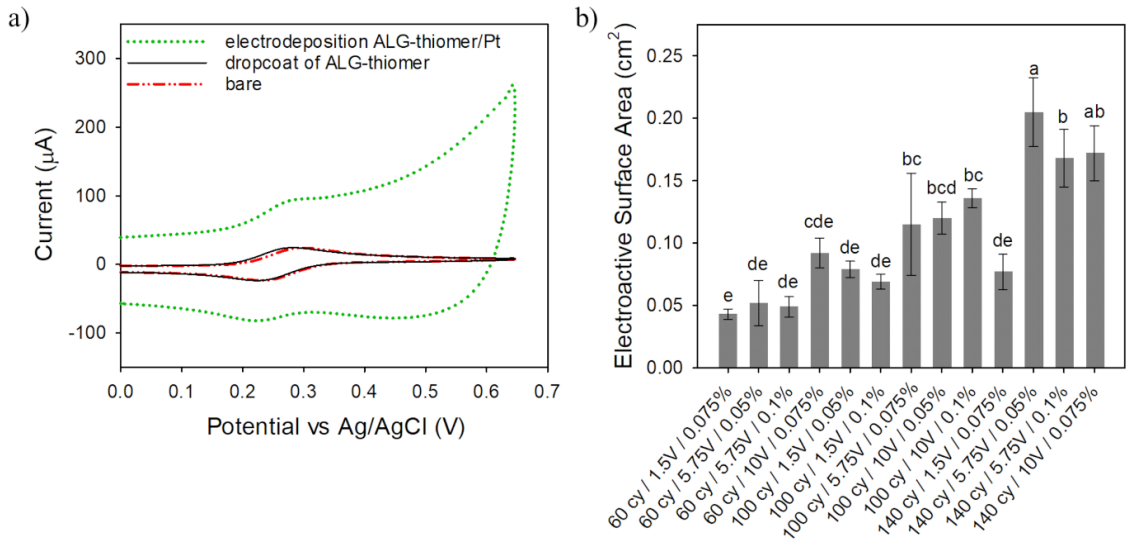

Figure 2.4 Electrochemical characterization of electrodes using 4 mM K_4FeCN_6 as the redox probe (pH ~7). (a) Representative CV curves at 100 mV/s scan rate of bare Pt/Ir, dropcoating of ALG-thiomer, and ALG-thiomer/Pt brush electrodeposition (best condition: 5.75 V/ 140 cycles / 0.05% ALG-thiomer). (b) Average electroactive surface area for various ALG-thiomer/Pt brush deposition conditions with different number of cycles (cy), voltages (V) and ALG-thiomer concentration (% w/v). All data represent the average of three replicates and error bars represent the standard deviation of the arithmetic mean; letters denote significantly different means ($p < 0.05$).

2.3.3. ALG-thiomer/Pt brush actuation and *Listeria* spp. capture

Alginate is an acidic polymer that has a pKa value between 3.2 and 4 (for guluronic and mannuronic acids, respectively) (S. J. Kim, Yoon, Lee, & Kim, 2004; Reddy et al., 2007). Normally, below the pKa of the alginate carboxylic acid groups are protonized in the COOH form and the polymer is collapsed. As the pH of the solution increases, the COOH becomes ionized to COO^-, and the resulting electrostatic repulsion among these groups causes the polymer to extend (Pasparakis & Bouropoulos, 2006; Reddy et al., 2007; J. Yang, Chen, Pan, Wan, & Wang, 2013). To test if the modification of alginate had any effect on its pH-stimuli actuation property and to characterize the

electrostatic interactions during actuation at the electrode's surface, CV tests were carried out with three different redox probes and the ESA values were calculated (Figure 2.5a). A negatively charged probe ($KFeCN_6^{3-}$), a neutral probe ($C_6H_4(OH)_2$), and a positively charged probe $Ru(NH_3)_6^{3+}$ were used. Moreover, CV was carried out at pH of 3 and 7, below and above the polymer's pKa, respectively (Figure 2.5a), for three repetitive cycles.

As shown in Figure 2.5a, above the pKa (pH 7), electron transport decreases with the $KFeCN_6^{3-}$ probe due to charge repulsion/steric hindrance as the alginate carboxylate group is negatively charged; with the neutral probe ($C_6H_4(OH)_2$) the electron transfer is less affected but still some swelling may happen due to intramolecular electrostatic repulsion among the carboxylate groups (COO^-) of the alginate (Pasparakis & Bouropoulos, 2006); and with the $Ru(NH_3)_6^{3+}$ probe, peak current and ESA increase due to electrostatic interactions. The opposite occurs below the pKa (pH 3), the electron transfer is favored with the negative probe increasing the peak current and ESA, while the peak current and ESA reduce with the positive probe. Similar behavior of ESA increasing or reducing due to electrostatic interactions or repulsion, respectively, have also been observed by Hills et al. (2018) for chitosan actuation with the same redox probes. With repetitive actuation, peak current and ESA changed slightly (Figure 2.5a) between repetitions; however, the percent change was not significant with no observable hysteresis, which indicates that ALG-thiomer/Pt brush actuation is reversible and can be repeated multiple times (at least 3 times) from collapsed to extended states. These results are an improvement from Hills et al. (2018) and Giacobassi et al. (2021) brush actuation

of chitosan and PNIPAAm, respectively, that reported actuation hysteresis between repetitions.

The ALG-thiomer/Pt brush was converted into an aptasensor by functionalizing with 400 nM of amino terminated aptamer via carbodiimide cross-linking, as shown in Figure 2.1 (see Appendix A for details). Based on the principle that binding of target bacteria to the aptamer decreases the electron transfer at the electrode's surface, which is measured as an increase of impedance, actuation tests were carried out with EIS to determine the optimum pH values for capturing and sensing *L. monocytogenes*. For these experiments, a constant *L. monocytogenes* concentration of 10^3 CFU mL^{-1} in PBS was used. In Figure 2.5b, the extended brush conformation at pH > 3.5 is noted as (EX), the collapsed brush conformation at pH < 3.5 is noted as (COL), the cell capture state is noted by (cap) and the electrochemical measurement step is noted by (meas). Cell capturing in the extended conformation (pH 7) and sensing at collapsed state (pH 3) provided the highest impedance values ($p < 0.05$) for all cutoff frequencies and, therefore, sensing efficiency (see also Bode plots in Figure A2 in the Appendix A). The optimum capture of targeted bacteria at the extended form can be related to a higher contact area with the tested solution and an increased probability of aptamer-cell interaction, compared to pH 3 at which the brushes are contracted, and the receptor binding site(s) may be inaccessible. Similar to previous works on this capture strategy, it is likely that the cells become entangled in the polymer matrix during the sensing step, where aptamer-target binding may no longer be the mechanism for cell capture but rather entanglement during nanobrush collapse. The specificity for this detection

platform is rooted in the initial affinity between aptamer and target at pH 7 (extended ALG-thiomer nanobrush), where the collapse at pH 3 likely causes secondary structure changes in the aptamer but also entraps cells in the polymer matrix.

This finding is consistent with the results reported by Hills et al. (2018) and Giacobassi et al. (2021) that also presented higher sensing efficiency using the EX/cap → COL/meas strategy for pathogen detection. Additionally, the modification on the alginate with cysteine followed by the aptamer attachment, using its carbonyl groups, seems to neutralize the negative charges of alginate that would normally cause electrostatic repulsion to the highly negatively charged (under most conditions) membrane of *L. monocytogenes* (Briandet, Meylheuc, Maher, & Bellon-Fontaine, 1999). This bacteria capture method is fairly simple compared to others reported in the literature such as the method by Malic et al. (2015) that developed a high gradient magnetic separation device tailored to immunomagnetic nanoparticles based on a 3D magnetic trap integrated into on a polymeric microfluidic device for magnetic capture and release of *L. monocytogenes.*

The dielectric properties of biological tissues are characterized by three dispersions including: a) α-dispersion occurring at low frequency, associated with tissue interfaces, such as membranes; b) β-dispersion at radiofrequency, caused by the polarization of cellular membranes, proteins and other organic macromolecules; and c) γ-dispersion at microwave frequency, associated with the polarization of water molecules (Amini, Hisdal, & Kalvøy, 2018). Cell membranes act as insulating barriers at low frequencies demonstrating resistive pathways, while demonstrating high capacitance

at higher frequencies. Consequently, the EIS actuation data were used to determine the cutoff frequency (CF). This analysis considered frequencies from 1 to 50 Hz, which falls within the alpha frequency dispersion region of biological tissues. The maximum impedance signal ($p < 0.05$) was observed at CF of 1 Hz (Figure 2.5b) and was selected to determine key performance indicators (KPI) for the aptasensor in complex media and mixtures of bacteria in the next section.

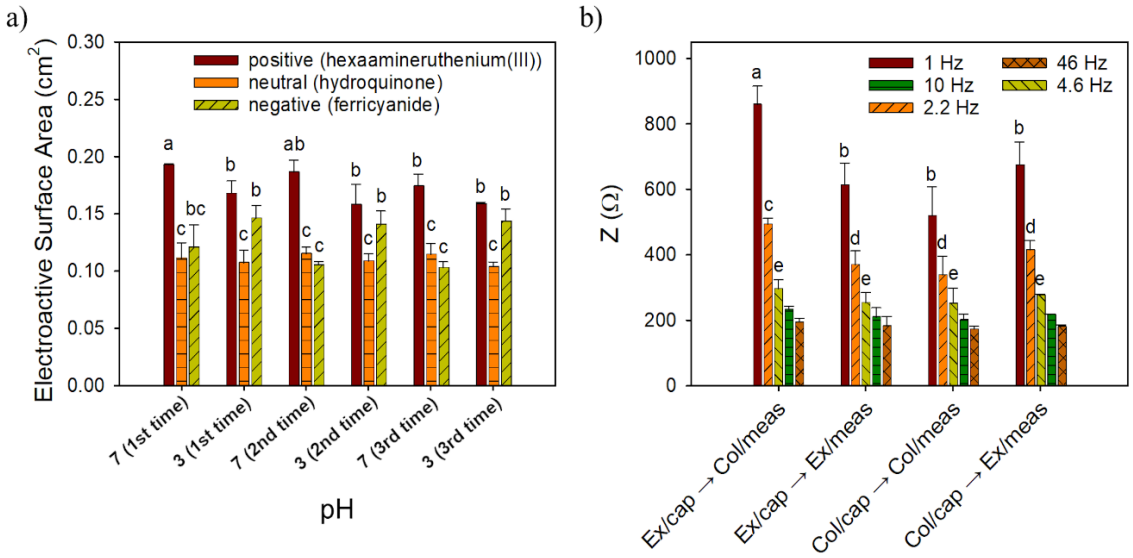

Figure 2.5 a) Electrostatic interactions during actuation of the ALG-thiomer/Pt brushes for various redox probes: a negatively charged probe ($KFeCN_6^{3-}$), a neutral probe ($C_6H_4(OH)_2$), and a positively charged probe ($Ru(NH_3)_6^{3+}$. The average electroactive surface area (ESA) is shown for each redox probe under repeated actuation at pH 3 and pH 7 (n = 3). b) Average total impedance for the ALG-thiomer/Pt brush functionalized with 400 nM aptamer and exposed to 10^3 CFU/mL of *Listeria monocytogenes* at different cutoff frequencies for various capture/measure strategies based on actuation. "EX" refers to extended state (pH 7), "COL" refers to the collapsed brush state (pH 3), "cap" refers to cell capture and "meas" refers to measurement. All data represent the average of three replicates and error bars represent the standard deviation of the arithmetic mean; letters denote significantly different means ($p < 0.05$).

2.3.4. Biosensor performance testing

The ability of the electrodes deposited with ALG-thiomer/Pt brushes functionalized with 400 nM of amino terminated aptamer to detect *L. monocytogenes* was evaluated by EIS. See Appendix A for details on the biosensor functionalization and results on optimum aptamer loading concentration onto ALG-thiomer/Pt brushes (Figure A1). Impedance differences caused by the presence of bacteria (ranging from 10^0 to 10^6 CFU/mL) were obtained using the EX/cap → COL/meas strategy (pH 7 → 3). The total test time was 17 min, which included 15 min for bacteria capture and 2 min for the EIS measurement. Bode plots are shown over a frequency range of 1 Hz to 100 kHz; insets are a zoomed in view of the lower frequency range (1-5 Hz). Based on the cutoff frequency (CF) analysis presented in Figure 2.5b, all calibration curves were developed using data from Bode plots for a CF of 1 Hz.

Figure 2.6 shows ALG-thiomer/Pt/aptamer nanohybrid electrode calibrated for *L. monocytogenes* and in the presence of *S. aureus*. The selectivity test was performed with *Staphylococcus aureus* due to its similarity to *Listeria* as Gram-positive bacteria and to both being known foodborne pathogens. The addition of an equal concentration of *S. aureus* in the testing solution did not show significant interference ($p > 0.05$) on the LOD (4.48 ± 0.82 CFU/mL with *L. monocytogenes* alone and 5.70 ± 2.10 CFU/mL with both bacteria) indicating no cross-reaction between the sensor and *S. aureus*. The sensitivity increased ($p < 0.05$) from 39.21 ± 2.61 Ω/log(CFU/mL) with *L. monocytogenes* alone to 69.34 ± 2.79 Ω/log(CFU/mL) when *S. aureus* was also present. The linear range also changed from 10^1-10^6 CFU/mL with only *L. monocytogenes* in

PBS to 10^1-10^5 CFU/mL in the bacteria mixture. Ohk et al. (2010) presented a LOD of 10^3 CFU/mL using the same aptamer in a fiber-optic biosensor to detect *Listeria* spp. While antibody sensors are reported to be prone to give false-positive reactions with *S. aureus*, which is also a protein A carrier, the aptamer used in the present work was proven to be selective to *L. monocytogenes* (Ohk et al., 2010). This aptamer targets the surface protein Internalin A which is one of the major invasion proteins involved in pathogenesis (Ohk et al., 2010). Despite the fact that this protein is structurally analogous to certain cell-wall proteins with internal repeats identified in members of the genera *Staphylococcus* and *Streptococcus* (Gaillard, Berche, & Frehei, 1991), the present results corroborate that this aptamer can be selective to *L. monocytogenes*.

After confirming the ALG-thiomer/Pt brush sensor ability to detect bacteria in PBS, the sensors were tested in a food product to determine its selectivity to the target bacteria as well as if the sensitivity may be affected by the interference of food components. Chicken broth (Figure 2.7) was used as it contains carbohydrates and proteins, among other components, that could interact with the biosensor through non-specific adsorption resulting in a false-positive signal. The sensitivity toward *L. monocytogenes* in chicken broth was 42.59 ± 2.35 Ω/log(CFU/mL) with LOD of 4.44 ± 0.75 CFU/mL, both similar ($p > 0.05$) to the results in PBS. These results also indicate that the aptamer was able to selectively bind to *L. monocytogenes* even in complex food matrices. Using the same aptamer, Hills et al. (2018) reported a slightly higher LOD of 9.1 CFU/mL in vegetable broth with a layer by layer reduced graphene oxide/nanoplatinum/chitosan brush electrode.

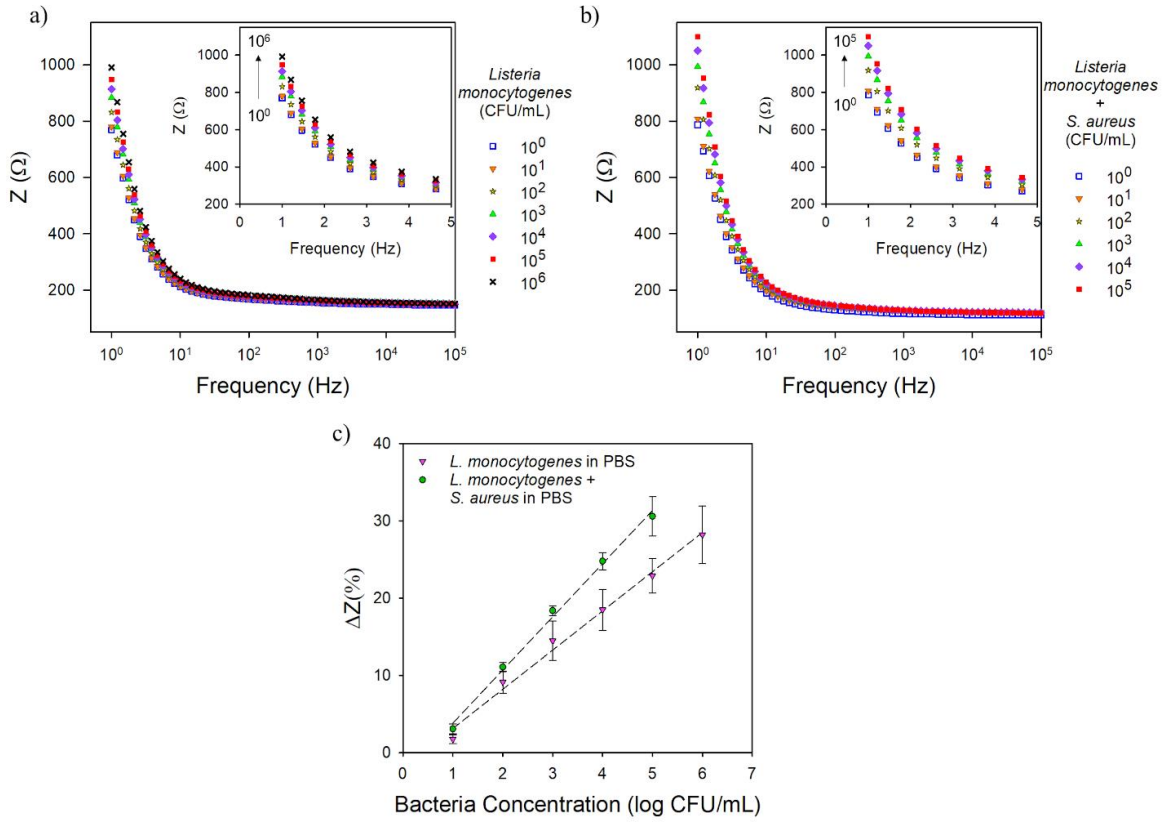

Figure 2.6 Representative Bode plots over the frequency range of 1-100,000 Hz (inset show exploded view over the frequency range from 1-5 Hz) for the ALG-thiomer/Pt brush sensor functionalized with 400 nM aptamer exposed to a) *L. monocytogenes* in PBS and b) *L. monocytogenes* + *S. aureus* in PBS. c) Calibration curves (total impedance change at 1 Hz vs. log bacteria concentration). All data represents the average of three repetitions. Error bars represent the standard deviation.

In order to further evaluate the binding effectiveness of the aptamer and its role on the biosensor performance, the ALG-thiomer/Pt brush sensor absent of aptamers was exposed to increasing concentrations of *L. monocytogenes* in PBS (see Appendix A, Figure A3). The LOD obtained was 28.88 ± 1.31 CFU/mL with sensitivity of 23.27 ± 7.87 Ω/log(CFU/mL), respectively. The performances of the sensor with aptamer

previously presented were significantly ($p < 0.05$) better when compared to the one without aptamer. Despite of some randomly trapping of bacteria onto the nanobrushes, these LOD and sensitivity results demonstrate the aptamer's role of selectively binding to *L. monocytogenes*, and significantly enhancing the performance of the sensor. In addition, these results further demonstrate the actuation protocol effectiveness to capture bacteria applying the ALG-thiomer/Pt brushes, which could be used as an initial step for food safety monitoring (i.e., total bacteria count).

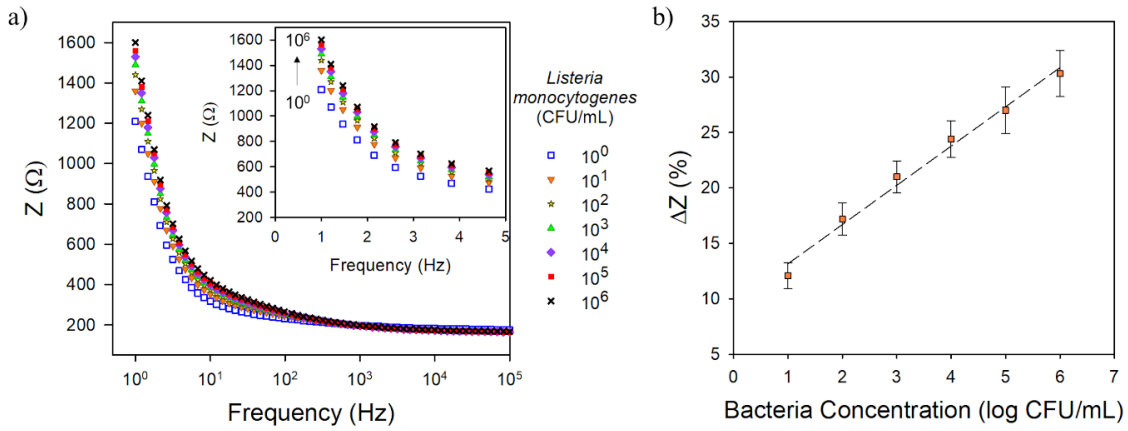

Figure 2.7 a) Representative Bode plot over the frequency range of 1-100,000 Hz (inset show exploded view over the frequency range from 1-5 Hz) and b) calibration curve (total impedance change at 1 Hz vs. log bacteria concentration) for the ALG-thiomer/Pt brush sensor functionalized with 400 nM aptamer exposed to *L. monocytogenes* in chicken broth. All data represents the average of three repetitions. Error bars represent the standard deviation.

Alginate is becoming more popular for biosensors applications due to its biocompatibility and functional groups useful for encapsulation and immobilization of biorecognition agents such for the detection of antibiotics, tumor cells, blood analysis,

among others (Y. Lin et al., 2020; Zhan, Hu, Wagberg, Zhan, & Xu, 2016). Some used encapsulated bacteria to monitor water toxicity (Jung, Seo, Lee, Kim, & Bock, 2014; Wasito, Fatoni, Hermawan, & Sutji, 2019), but still, fewer reports involve bacteria detection. For instance, Kikuchi et al. (2020), used alginate to encapsulate a colorant that was cleaved by β-galactosidase enzyme from *E. coli* for its detection in breast milk, reporting a LOD of 10^2 CFU/mL after 2 to 8 h incubation.

A compilation of current biosensors for the detection of *L. monocytogenes* in different food samples or buffers is presented in Table 2.1. R. Liu et al. (2021) presented good results detecting *L. monocytogenes* in a range of 68 to 68 × 10^6 CFU/mL by using aptamer-functionalized magnetic nanoparticles (as pre-concentration probes) and aptamer-functionalized upconversion nanoparticles (fluorescent signal probes) together; however, the procedure includes an 1 h incubation plus a pre-concentration step. Sidhu et al. (2016) proposed a platinum interdigitated array microelectrode functionalized with the same aptamer used in the present work and reported a LOD of 5.39 CFU/mL of *Listeria* spp. in PBS also with 17 min detection. In another work, Sidhu et al. (2020) applied the same platinum interdigitated array microelectrodes functionalized with aptamers for rapid on-site flow through detection of *Listeria* spp. in irrigation water using a smartphone-based potentiostat and in flow conditions and the reported LOD was 48 CFU/mL. The ALG-thiomer/Pt sensor offers some advantages over most found in the literature, including simpler and faster fabrication with no need for cleanroom fabrication; no labeling nor bacteria pre-concentration required; and short detection time,

being among the most efficient platform for *L. monocytogenes* sensing to date, with low limit of detection and wide linear sensing range relevant to food safety.

Table 2.1 Biosensor performance comparison to other devices in the literature used in the detection of *L. monocytogenes.*

Biorecognition agent and platform	**Detection mode**	**Test medium**	**Detection range* (CFU/mL)**	**Response time (min)**	**Reference**
ALG-thiomer/Pt + aptamer	Impedimetric	PBS	4.5 - 10^6	17	This work
ALG-thiomer/Pt + aptamer	Impedimetric	PBS + *S. aureus*	5.7 - 10^5	17	This work
ALG-thiomer/Pt + aptamer	Impedimetric	Chicken broth	4.4 - 10^6	17	This work
ALG-thiomer/Pt (no aptamer)	Impedimetric	PBS	28.9 - 10^6	17	This work
rGO-nPt + CHI + aptamer	Impedimetric	Vegetable broth	9.1 - 10^2	17	(Hills et al., 2018)
rGO-nPt + CHI + aptamer	Impedimetric	PBS	3 - 10^7	17	(Hills et al., 2018)
rGO-nPt + CHI + antibody	Impedimetric	Vegetable broth	15.6 - 10^4	17	(Hills et al., 2018)

Table 2.1 Continued

Biorecognition agent and platform	**Detection mode**	**Test medium**	**Detection range* (CFU/mL)**	**Response time (min)**	**Reference**
Pt-IDE + aptamer	Impedimetric	PBS	5.4 - 10^6	17	(Sidhu et al., 2016)
UCNP/aptamer + MNP/aptamer	Fluorescence	PBS	68 - 68×10^6	> 60	(R. Liu et al., 2021)
AIE-NP + MNP + aptamer + antibody	Fluorescence	PBS	10 - 10^6	90	(Guo et al., 2020)
GNP + antibody	Dynamic light scattering	PBS	35 - 10^3	120	(X. Huang et al., 2015)
TiO_2 nanowire + antibody	Impedimetric	BHI growth medium	10^2 - 10^7 (non-linear)	60	(R. Wang et al., 2008)

* Includes the lower limit of detection (LOD)
rGO-nPt + CHI: reduced graphene oxide/nano-platinum + chitosan
Pt-IDE: platinum interdigitated array microelectrodes
UCNP: upconversion nanoparticles
MNP: magnetic nanoparticles
AIE-NP: aggregation-induced emission nanoparticles

2.4 Conclusions

Detection of a specific pathogen in any real food sample is time-consuming and laborious, as there are background signals due to impurities in the sample, either from the complex multicomponent structures or the presence of other microorganisms (pathogenic and nonpathogenic) that requires pre-enrichment treatments and laboratory settings. This study reports on a highly sensitive, selective and simple to fabricate impedimetric aptasensors using a one-step fabrication process of alginate thiomer/platinum nanobrushes. For the first time, this work showed that ALG-thiomer modified with nanoplatinum and aptamers maintained stimuli-responsive properties of the alginate while also maintaining the affinity for target bacteria, *L. monocytogenes,* due to aptamer binding. Actuation of the ALG-thiomer/Pt brushes significantly improved bacteria detection due to matrix entrapment in the collapsed state. The detection limit of 5 CFU/mL and linear sensing range varying from 10 to 10^6 CFU/mL in a food sample cover the relevant levels for food safety analysis, enabling food manufacturers to reduce economic and public health implications from recalls of contaminated food. Comparing to other methods available in the literature, this sensor is among the most efficient capture mechanisms for *L. monocytogenes,* in addition to other advantages such as simple one-step fabrication, and no labeling, no pre-incubation nor concentration required and a response time of 17 min. The results presented in this study demonstrated that the developed sensor platform was suitable for its used in food safety monitoring

applications. Furthermore, this ALG-thiomer platform can be further tested for detection of other foodborne pathogens or small molecules sensing. This novel approach demonstrateed a new biosensing platform with combinatorial features that considerably advance detection of targets in complex matrices.

CHAPTER III ONE-STEP FABRICATION OF STIMULI-RESPONSIVE CHITOSAN-PLATINUM BRUSHES FOR *LISTERIA MONOCYTOGENES* DETECTION

3.1. Introduction

Incidents involving foodborne infection continue to be an important concern to consumers and a great financial and marketing burden for the food manufacturers, regardless of the efforts to prevent them. The Centers for Disease Control and Prevention (CDC) estimates that each year in the U.S., about 1 in 6 people (or 48 million) get sick, 128,000 are hospitalized, and 3,000 die from a foodborne illness. *Listeria* spp. is estimated to be on third place on the overall rank of pathogens contributing to domestically acquired foodborne illnesses resulting in death, after *Salmonella enterica* and *Toxoplasma gondii* (CDC, 2018). In 2020, the US Food and Drug Administration (FDA) reported 50 products recalls due to potential contamination with *Listeria* spp. (FDA, 2021). Because of the severity of *Listeria* infection, the prevalence of this bacteria in food products including fresh produce, ready-to-eat, refrigerated and frozen products, it is important to find detection methods that are faster than the current method, such as culturing the bacteria from samples which usually require pre-enrichment steps. The traditional methods that are used to detect foodborne pathogens in the food industry – plate counts, enzyme linked immunosorbent assay (ELISA), polymerase chain reaction (PCR) – are laborious, time consuming and expensive (Alocilja & Radke, 2003). The Food Safety and Modernization Act (FSMA) launched by the FDA in 2011 was designed to improve public health by focusing on

preventing food pathogen outbreaks instead of a reactionary approach. FSMA mandates comprehensive, science-based preventive controls compulsory for all food products (FDA, 2018). Hence, the development of biosensing platforms is a trending area of research for bacteria detection, as these technologies can lead to reliable and rapid screening that conventional techniques are not capable of. The outcome of such screening aims to determine whether foods are contaminated with pathogens in time to prevent them from reaching the public or contributing to food waste (Castell-Perez et al., 2017; Heo et al., 2014).

Electrochemical biosensors are capable of detecting targeted bacteria by sensing the changes in electrical properties caused by biochemical reactions or molecular interactions at the surface of the working electrode (V. S. Somerset, 2011; Vanegas, Gomes, et al., 2017). Among the different possible biorecognition agents (including enzymes and antibodies), several aptamers (oligonucleotide sequences identified through selective evolutionary enrichment) and aptamer-based sensor platforms (aptasensors) have been developed to detect cell-surface targets on intact *Listeria monocytogenes* (V. S. Somerset, 2011). Aptamers show similar or higher affinity for whole cell targets than monoclonal antibodies, and have the advantage of being smaller and allowing higher densities of pathogen-sensing elements leading to higher sensitivity and lower nonspecific adsorption (Vanegas, Gomes, et al., 2017). Additionally, aptamers present better chemical stability under most environmental conditions and longer shelf life than antibodies (V. S. Somerset, 2011). Aptasensors have shown promising results for bacteria sensing, as recently reviewed with fast response time (detection in minutes to

hours), no pre-enrichment requirements, and detection limits ranging from 10 to 10^3 CFU/mL (Vanegas, Gomes, et al., 2017).

Platinum deposited as nanoparticles has been used in sensing as a signal amplification strategy. It improves sensors performance due to higher current densities and faster mass transport compared to larger macro particles as well as increased electrocatalytic behavior (Taguchi et al., 2016). Electrodeposition is a versatile and efficient process in which an imposed electric field is employed to direct charged particles dispersed in a liquid towards an electrode for the assembly of thin films (Z. Wang et al., 2014); however, the use of standard potentiostatic or galvanostatic methods produces an array of nanoparticle sizes and morphologies formed due to the progressive generation of nucleation sites, rather than instantaneous formation (Taguchi et al., 2016). Taguchi et al. (2016) developed pulSED, a method combining pulsing electrodeposition and sonication that provided more uniform deposition of platinum nanostructures resulting in increased mass transfer to the electrode surface.

Chitosan is a natural biodegradable, biocompatible and low-cost pH stimulus-responsive polymer. It is a long-chained molecule extracted from the exoskeletons of crustaceans with pKa of ~6.5 (Elgadir et al., 2015). Chitosan is hydrophilic and positively charged in acidic to neutral solution and readily binds to negatively charged surfaces shifting to hydrophobic at pH values above its pKa (Y. Liu, Yang, Shi, Bentley, & Payne, 2010). This property enables the electrodeposition of chitosan from an aqueous bulk solution onto a conductive surface in response to cathodic signals requiring no crosslinking agents in a relatively quick process at room temperature (Cheng et al., 2010;

Z. Wang et al., 2014). It has also been shown that chitosan exerts multifunctional forces on bacteria such as hydrophobic, hydrogen bond, and electrostatic interactions that are complementary and can reinforce each other (Abdelhamid & Wu, 2013b). This property combined with the pH stimulus response have been shown to be beneficial for sensing bacteria, as it has been demonstrated that the actuation of chitosan (pH stimulus) (Hills et al., 2018) and PNIPAAm (temperature stimulus) (Giacobassi et al., 2021) brushes can improve bacteria detection in complex aqueous media by increasing the probability of target-receptor interaction as a result of microscale structural changes. These previous work demonstrated that actuation of brushes with bacteria capture while brushes were in the extended state followed by brush collapse improve sensing performance (i.e., signal to noise ratio) (Giacobassi et al., 2021).

A wide variety of sensor coating materials have been used in aptasensing. Attachment of aptamers to the sensor surface involves functionalization of the oligomer at the 5’ end with a tag (e.g., biotinylation, thiolation, etc.). Thiolation (conjugation of a thiol group) is one of the most versatile tagging methods and is highly useful in electrochemical sensing due to the coupling with noble metal(s) on the sensor surface (e.g., gold, platinum, etc). Herein, this work showed the development of a rapid, label-free impedimetric aptasensor for real-time detection of *Listeria monocytogenes* in chicken broth based on stimulus response of CHI/Pt brushes through a combination of electrostatic interactions and aptamer-cell binding. Additionally, it was demonstrated that actuation of CHI/Pt brushes resulted in improved *Listeria* spp. capture and controllable electrochemical transduction based on external stimulus (i.e., pH change) in

the presence of interferents from food samples. This effect was likely due to polymer entrapment after initial aptamer binding to target cells.

3.2. Materials and methods

3.2.1. Materials and reagents

Chloroplatinic acid 8 wt.%, chitosan (low molecular weight, 75-85% deacetylated 20-300 cP), hydroquinone, hexaammineruthenium(III) chloride, potassium phosphate monobasic, and sodium phosphate dibasic were purchased from Sigma-Aldrich Co. (St. Louis, MO). Polycrystalline diamond suspensions (1 µm and 3 µm) and alumina slurry (0.05 µm) were obtained from Buehler (Lake Bluff, IL). Lead acetate (30% w/v) was purchased from Fisher Scientific (Pittsburgh, PA). Potassium ferrocyanide trihydrate was purchased from Ward's Science (Rochester, NY). Potassium ferricyanide and cysteine hydrochloride monohydrate were obtained from J.T. Baker (Phillipsburg, NJ). Platinum/iridium working electrodes (Pt/Ir, BASi MF-2013, 1.6 mm diameter, 7.5 cm length), reference electrode (Ag/AgCl) and Pt auxiliary electrode were purchased from BASinc. (West Lafayette, IN).

Sulfo-SMCC (sulfosuccinimidyl 4-(N-maleimidomethyl)cyclohexane-1-carboxylate) and 1-ethyl-3-(3-dimethylaminopropyl)carbodiimide HCl (EDC) were obtained from Thermo Fisher Scientific (Waltham, MA). N-Hydroxysuccinimide (NHS), 2-(morpholino)ethanesulfonic acid (MES) buffer, Ellman's reagent (5,5'-dithiobis-(2-nitrobenzoic acid)), and platinum wire (99.95% Pt, 1.5 mm dia.) were obtained from

Alfa Aesar (Ward Hill, MA). DiaEasy™ dialysis tubing (3.5 kDa MWCO) were purchased from Biovision (Milpitas, CA).

L. monocytogenes aptamer developed by Ohk et al. (2010) (47 DNA bases, K_D = 10^3 CFU/mL, Mw 15,008 g/mol) terminated at the 5' end with a thiol group was purchased from Gene Link (Hawthorne, NY). Commercially sterilized chicken broth was purchased from a local grocery store. Tryptose phosphate broth (TPB) was acquired from HiMedia (Mumbai, India). Tryptic soy broth (TSB), Tryptic soy agar (TSA), yeast extract, and buffered peptone water (BPW) were purchased from Becton, Dickson and Company (Sparks, MD). Potassium nitrate (KNO_3) was purchased from British Drug Houses (ON, Canada). Tris EDTA (TE) buffer pH 7.4 was purchased from Quality Biological (Gaithersburg, MD). Sodium chloride (NaCl) and potassium chloride (KCl) were acquired from EMD Millipore Corporation (Burlington, MA).

3.2.2. Bacteria cultures

Listeria monocytogenes (ATCC 15313) and *Staphylococcus aureus* (ATCC 25923) were resuscitated from frozen culture in TPB and TSB; respectively, using two identical consecutive transfers incubated at 35 °C for 24 hours under aerobic conditions. Total aerobic plate counts were measured in triplicate by serially diluting samples of the bacteria in BPW and plating on TSA and TSAYE for *S. aureus* and *L. monocytogenes*, respectively. Bacteria were maintained on tryptic soy agar (TSA) and TSA with 0.6 wt.% yeast extract (TSAYE) slants for *S. aureus* and *L. monocytogenes*; respectively and stored at 4 °C for no more than 3 months. *L. monocytogenes* and *S. aureus* are

pathogenic microorganisms and must be handled using biosafety level 2 standards established by the National Institute of Health.

3.2.3 Chitosan thiomer synthesis

Chitosan thiomers (CHI-thiomer) were synthesized by modifying chitosan (CHI) with thioglycolic acid (TGA) based on modification of Kast & Bernkop-Schnurch (2001) using sulfo-NHS/EDC reaction to yield a high content of thiol termination on the resulting product. The modification was as follows: TGA carboxylate groups (-COOH) reacted to N-hydroxysulfosuccinimide (sulfo-NHS) in the presence of EDC (1-ethyl-3-[3-dimethylaminopropyl]carbodiimide hydrochloride), resulting in a semi-stable sulfo-NHS ester, which then reacted with primary amines ($-NH_2$) on the chitosan to form amide crosslinks, resulting in a chitosan-TGA complex (CHI-thiomer) that was thiol-terminated.

First, a reaction was performed between TGA, EDC and sulfo-NHS (2:1:2.5 in molar concentration) in MES buffer containing sodium chloride at pH 5-6 for 30 min. The pH was then adjusted to 7.2-7.5 and a solution containing the chitosan (equal mass of TGA) was then added (doubling the volume). The pH was again adjusted to 6 and left to react under agitation for 2.5 hours. After dialysis using 3.5 kDa tubing to eliminate the unbonded TGA and isolate the polymer conjugates, the eluent was freeze dried (-50 °C, -0.120 mBar, 48 h) in a Labconco FreeZone 6 unit (Labconco, Kansas City, MO, USA) to obtain the thiolated complex of chitosan-thioglycolic acid (CHI-thiomer).

The degree of thiolation was quantified using Ellman's Analysis (Thermo Scientific, 2011). Briefly, the reaction between the samples and the Ellman's reagent (5,5'-dithiobis-(2-nitrobenzoic acid)) was performed in a phosphate buffer containing 1mM EDTA (ethylenediamine tetraacetic acid) at pH 8. The absorbance of each sample was measured in a Genesys 10S spectrophotometer (Thermo Scientific, Waltham, MA) at 412 nm against a blank control and the thiol concentration calculated through the correlation with a standard curve of cysteine hydrochloride monohydrate. The result obtained was 40 ± 6 µM thiol groups/g of polymer sample, similar to Kast & Bernkop-Schnurch (2001) that presented 38.23 µM thiol groups/g of polymer sample.

3.2.4. Nanomaterial deposition

The pulsed sonoelectrodeposition method (alternating applied potential and sonication in cycles of 1 second each) (Taguchi et al., 2016) was applied for the simultaneous deposition of chitosan and platinum onto the surface of Pt/Ir electrodes. For the deposition, a platinum wire (positive or anode) and the working electrode (negative or cathode) were connected to the power supply and submerged in the deposition solution composed of 0.72 wt.% chloroplatinic acid, 0.001 wt.% lead acetate and chitosan (non-modified and thiol-modified) at different concentration (see Figure 3.1). Different deposition parameters and concentrations of chitosan were evaluated to determine the optimal deposition conditions. For the chitosan thiomer and platinum co-deposition (CHI-thiomer/Pt) it was used 0.05, 0.15 and 0.25 wt.%; 2, 6 and 10 V for 40, 60 and 80 cycles. Based on the results of the CHI-thiomer/Pt, only 0.05 and 0.15 wt.%, 6

and 10 V, 60 and 80 cycles were used for the non-modified chitosan and platinum simultaneous deposition (CHI/Pt).

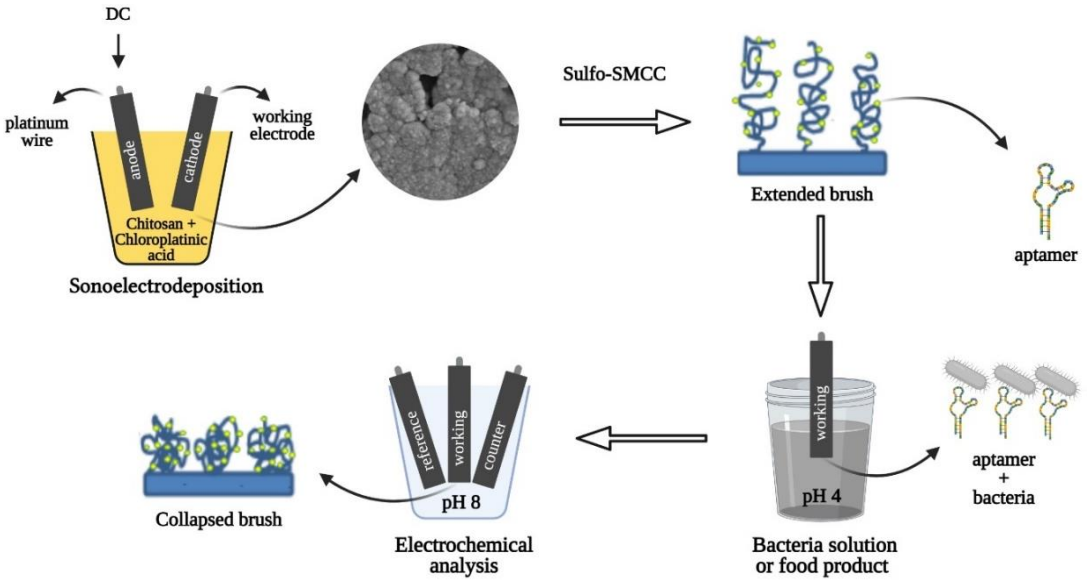

Figure 3.1 Fabrication, biofunctionalization, and sensing scheme of the platinum-decorated (CHI/Pt) aptasensor. CHI/Pt brushes were formed on the working electrode surface by a one-step sonoelectrodeposition method. Biofunctionalization with aptamers that target the protein Internalin A on *Listeria monocytogenes* membrane occurred via bonding between thiolated aptamer and nanoplatinum. Brush actuation for enhanced bacteria capture was facilitated by pH changes before and after electrochemical analysis.

3.2.5. Material characterization

Morphological characterization of the optimized depositions was conducted by scanning electron microscope (SEM) using a Quanta 600 FEG from FEI (Hillsboro, OR). Electrodes were coated with a 5 nm thick layer of platinum using a Cressington sputter coater 208 HR (Watford, UK) and allowed to ventilate for 30 min prior to SEM imaging. Images were taken with an operating voltage of 10 kV at 10,000, 20,000, and

30,100 times magnification for CHI/Pt brush deposition; and 5,000 and 10,000 times for thiomer brushes.

X-ray photoelectron spectroscopy (XPS), also known as electron spectroscopy for chemical analysis (ESCA), was used to analyze the surface chemistry of the selected optimized conditions for the deposition of CHI/Pt and thiomer brushes. XPS was performed in an Omicron ESCA+ (Scienta Omicron, Sweden) equipped with a Mg/Al dual X-ray gun and CN10 electron gun.

3.2.6. Electrochemical analysis

Cyclic voltammetry (CV) and/or electrochemical impedance spectroscopy (EIS) methods, as described by Hills et al. (2018) and Giacobassi et al. (2021), were used as noted. A three-electrode system with a platinum auxiliary electrode and an Ag/AgCl reference electrode at room temperature was used with a CHI 600E potentiostat analyzer. Cottrell plots were used to calculate the electroactive surface area (ESA) via Randles-Sevcik theory based on CV. ESA was used to evaluate the best deposition parameters for each polymer (CHI and CHI-thiomer), pH stimulus (4 and 8) and attachment of different concentrations of aptamers (500 to 1500 nM). CV analysis was conducted in 4 mM $[Fe(CN)_6]^{3-}$ with 1 mM KNO_3 using a 10 sec quiet time, a 650 mV switching potential and scan rates of 50, 100, 150, and 200 mV/s (Taguchi et al., 2016).

Various redox probes were used to study changes in electrochemical behavior that are correlated with electrostatic interactions. Hydroquinone was used as a model neutral probe, hexaaminеruthenium(III) chloride was used as a model positive probe,

and potassium ferrocyanide trihydrate was used as a model negative probe. The actuation tests were conducted with 4 mM redox probes in 1 mM KNO_3 solution, and the pH was adjusted to pH 8 or pH 4, using a 1 M HCl or NaOH solution. The pH of the redox solutions was monitored during the tests to ensure reported pH did not change by more than 0.5 pH units.

EIS was used to measure differences in impedance caused by bacteria presence (ranging from 10^0 to 10^6 CFU/mL). For details of functionalization procedure of CHI/Pt and CHI-thiomer/Pt brushes with aptamers, see Appendix B. Non-Faradaic EIS was performed in phosphate buffer saline (PBS) or chicken broth with a frequency range of 1-100,000 Hz, AC amplitude of 100 mV and initial DC potential of 0 V. Bode plots (total impedance versus frequency) were used to derive calibration curves at cutoff frequencies as noted. The limit of detection (LOD) was calculated using the 3σ method, and the analytical sensitivity was determined by the slope of the linear portion of the calibration curve ($R^2 > 0.98$) at a fixed frequency (Giacobassi et al., 2021). Analysis with the presence of interferents (food components and/or other bacteria) was assessed to determine the selectivity for target bacteria.

3.2.7. Statistical analysis

All experiments were performed at least in triplicate and analyzed using one-way analysis of variance, ANOVA, to test for significance. Statistical significance was expressed at the $p < 0.05$ level; significantly different means were classified using a Tukey test.

3.3. Results and discussion

3.3.1. Nanobrush material characterization

XPS spectrum of the CHI/Pt brushes (Figure 3.2) shows the effective co-deposition of both chitosan and platinum based on the presence of C 1s, O 1s, N 1s, and Pt 4f and Pt 4d peaks. C 1s peaks between 285 eV and 286.5 eV are assigned to CH_2 alkyl chain backbone, C-NH_2 and C-O species (Baio et al., 2009; Hwang et al., 2019). The N 1s binding energy between 399 eV and 401 eV are consistent with that of C-N species of the amine group at 399 eV, and of protonated amine group at 401 eV (Baio et al., 2009; Z. Wang et al., 2014). Hwang et al. (2019) assigned a peak at 399.3 eV to the amino group involved in the hydrogen bond and a peak at 401.7 eV to the chelation between the amino group and bismuth metal. From the platinum co-deposition, the Pt 4f spectrum shows a characteristic doublet with binding energies of 71.5 eV and 74.8 eV (Figure 3.2 inset). Some authors associate the binding energy around 71-71.5 eV with metallic Pt^0 (Moulder et al., 1992; Romanchenko et al., 2018) while others described a doublet as typical for the 7/2 and 5/2 spin states for pure Pt nanoparticle in the zero-valent state at lower binding energies (70 eV and 73.3 eV, respectively) (H. Liu, Feng, Cao, & Yang, 2014; B. Yang & Agrios, 2018). A doublet at 71.1 eV and 74.4 eV was also observed for control studies using only platinum deposited onto the surface from chloroplatinic acid solution (data not shown). See Figure B4 in the Appendix B for the XPS spectrum of the CHI-thiomer/Pt brush.

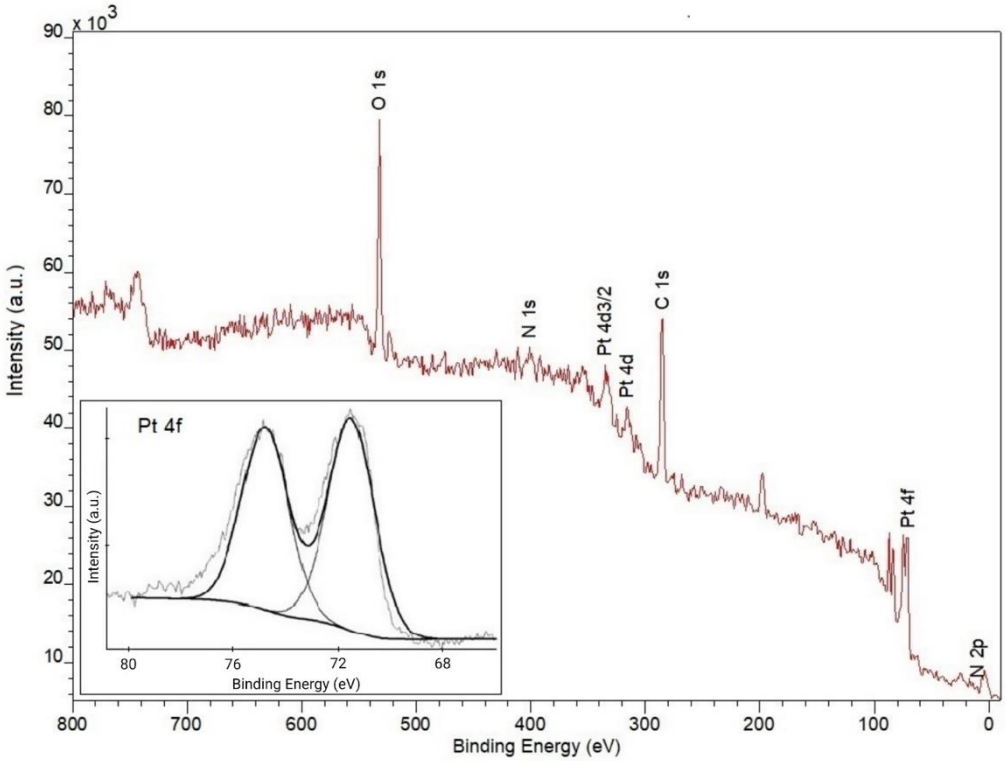

Figure 3.2 X-ray photoelectron spectroscopy (XPS) survey spectrum of the CHI/Pt brush deposition, demonstrating that both chitosan and platinum were successfully deposited with the presence of C 1s, O 1s, N 1s, and Pt 4f and Pt 4d peaks. Inset shows the Pt 4f spectrum.

J. Liu et al. (2013) studied Pt electrodeposition showing that pulse duration affects surface morphology, and for pulses of 1 s, as in the present work, the electrodeposition process was controlled by the diffusion process, since the consumed Pt ions cannot be compensated at this pulse rate. Consequently, the Pt nuclei tend to grow into 2D planer structure, which results in a relatively large electroactive surface area (ESA) (discussed in section 3.3.2). In the present work, the simultaneous deposition of CHI/Pt brushes resulted in heterogeneous distribution of nanobrushes and non-uniform formation of brushes with sizes between 80 and 250 nm on the electrode surface that

resembled of spheroids composed of smaller spheroids (Figure 3.3). Overall, the microstructures were less uniform than what was observed by J. Liu et al. (2013) and the morphology in this work was smoother, which was likely due to the chitosan co-deposition. Hills et al. (2018) showed electrodeposition of chitosan over a reduced graphene/platinum layer presented a more brush-like morphology with visible longitudinal shafts and larger terminal nodes (200-300 nm) than the work here. In a similar paper, Giacobassi et al. (2021) reported the size of PNIPAAm nanobrush terminal nodes between 220 and 1300 nm with similar spheroid structure as the CHI/Pt brushes here, although more uniformly distributed. Additional images for the CHI/Pt brush deposition are available in the Appendix B (Figure B1) as well as images of the CHI-thiomer/Pt brush deposition (Figure B5).

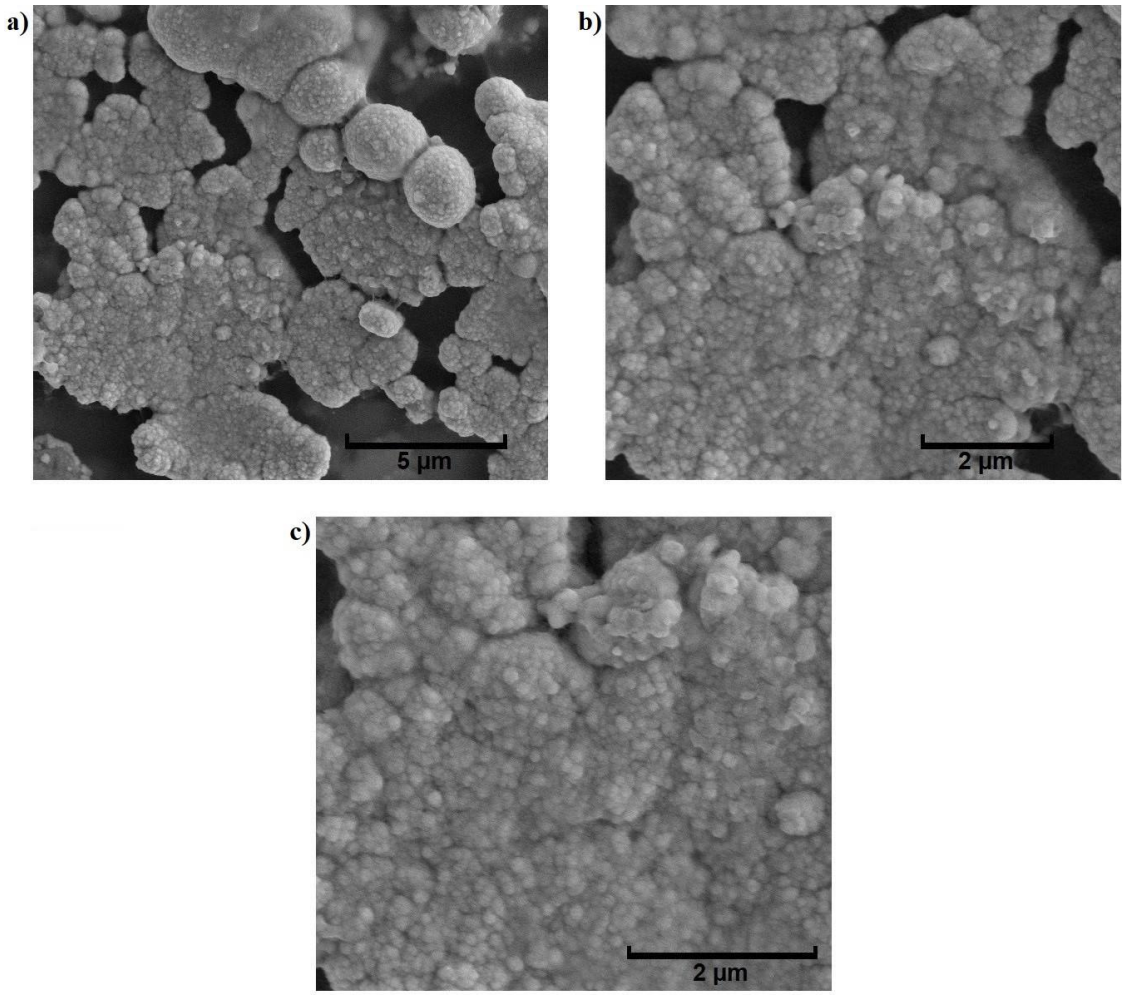

Figure 3.3 Morpholocial characterization by scanning electron miscroscopy (SEM) images of CHI/Pt brushes at 10 kV and a) 10,000, b) 20,000, and c) 30,100 times magnification show a heterogenous surface with irregular distribution of CHI/Pt brushes with sizes between 80 and 250 nm on the electrode surface that resembled of spheroids composed of smaller spheroids

3.3.2. Electrochemical characterization

Cyclic voltammograms in 4 mM K_4FeCN_6 and 1 M KNO_3 (pH = 7.1, T = 25 °C) were obtained in order to determine the optimal brush deposition conditions. Figure 3.4a shows the average electroactive surface area (ESA) for electrode treated with CHI/Pt brushes. Figure 3.4b shows representative cyclic voltammetry (CV) curves of the best

conditions for CHI/Pt and CHI-thiomer/Pt brushes (more results available in Figure B6 in the Appendix B) compared to bare Pt/Ir electrode and dropcoating of CHI-thiomer (chitosan modified with thioglycolic acid (TGA)) without Pt co-deposition at the bare electrode's surface. The thiol groups on the CHI-thiomer did not promote enough attachment onto the electrode's surface by dropcoating, i.e., no significant change ($p < 0.05$) in current peak value (Figure 3.3b) and, consequently, on ESA value. The experiments with CHI-thiomer/Pt brush were the first ones to be performed and results demonstrated that at lower voltage (2 V) and number of cycles (40 cycles) as well as higher CHI-thiomer concentration (0.25% wt.) reduced ($p < 0.05$) ESA values (see Figure B6 in Appendix B), consequently these conditions were eliminated for the experiments with CHI/Pt brushes.

According to Grainger & Blunt (1998), during the electrodeposition of Pt, the applied direct current induces the platinum ions in suspension to migrate towards the cathode where they convert to metal nanoparticles and deposit onto the working electrode surface. Chitosan is positively charged when soluble (below its pKa). Some studies demonstrated that chitosan-based hydrogels could be deposited onto a cathode surface as the voltage applied promotes proton-consuming hydrogen evolution reaction at the cathode surface (Cheng et al., 2010; Fernandes et al., 2003; L. Wu et al., 2002). This leads to a gradual increase of the pH near the cathode surface, and if this localized pH exceeds above 6.3, then chitosan becomes insoluble and deposits at the cathode surface (Fernandes et al., 2003; Luo, Xu, Du, & Chen, 2004). Yet, as the current density increases, the region of high pH is expected to extend further from the cathode surface

into the bulk solution (Fernandes et al., 2003). It has been reported that the thickness of the deposited chitosan film was dependent upon the applied voltage, the chitosan concentration, and the deposition time (Luo et al., 2004; L. Wu et al., 2002). For instance, Luo et al. (2004) found that longer deposition time (10 min) resulted in tight attachment of thick films and longer response time of the resulting biosensors, while shorter deposition time (1 to 3 min) resulted in thin and unstable chitosan film and shorter response time of the resulting biosensors. Hills et al. (2018) stated that electropolymerization of chitosan for 2 min resulted in nanobrushes with no appreciable stimulus-response, while polymerization times longer than 6 min resulted in nanobrushes that did not adhere well to reduced graphene oxide/platinum electrodes. In the present work, on preliminary tests, deposition times longer than 160 seconds (80 cycles) resulted in deposition beyond the working diameter of the electrode. Taguchi et al. (2016) experienced a similar result with pure Pt electrodeposition over 180 seconds and stated that this "overgrowth" might not be stable and flake off when immersed in solution. Cheng et al. (2010) also reported a lateral expanding thickness of electrodeposited chitosan exceeding the electrode edge with increasing deposition times and current densities. As shown in Figure 3.4a (and Figure B6 in Appendix B), despite of all the different deposition conditions tested, there were no significant ($p > 0.05$) differences among the ESA values obtained, consequently 6 V was selected for further experiments of both CHI/Pt and CHI-thiomer/Pt brushes since overgrowth was often observed with 10 V co-deposition. The simultaneous deposition of Pt nanoparticles with the chitosan seems to have a more pronounced effect on overgrowth occurrence.

For the selected optimum condition of 80 cycles / 6 V / 0.05% CHI, the electrodeposition of CHI/Pt brushes onto electrodes increased ($p < 0.05$) the average ESA by 11 times (0.31 ± 0.02 cm^2) from the bare Pt/Ir electrode (0.028 ± 0.003 cm^2). This ESA value was similar to previous work by Taguchi et al. (2016) with ESA value of 0.3 cm^2 when depositing platinum nanoparticles using the same pulSED technique used in the present work with higher voltage and deposition time (10 V and 90 cycles). Hills et al. (2018) presented ESA about 6 times lower (0.048 ± 0.017 cm^2) than the present work with chitosan being electrodeposited onto a reduced graphene oxide/nano-platinum coated electrode. The improved ESA results obtained here with the simultaneous electrodeposition of chitosan and platinum might be attributed to the properties of chitosan related to formation of stable chelates with many transition metal ions due to the presence of hydroxyl and amino groups, which provide enhanced affinity to metal ions and improved detection sensitivity (Berger et al., 2004; Hwang et al., 2019).

Some reports on the use of metals and chitosan together to produce sensors are available in the literature, most of them with two or more steps for the deposition, either layer by layer deposition (Hills et al., 2018) or by forming a metal-chitosan complex prior to deposition (Akhtar, Ilyas, Dlouh, Siska, & Boccaccini, 2020). Hwang et al. (Hwang et al., 2019) performed a co-electrodeposition of bismuth and chitosan for the detection of heavy metals in wastewater. Reduced graphene oxide and chitosan were co-electrodeposited by chronoamperometry (Dinshaw et al., 2017). However, a simultaneous electrodeposition of chitosan and platinum to fabricate stimuli-responsive

biomimetic nanostructures has not been found before, nor its use to detect bacteria in food products. This work focused on applying pulSED to a new one-step simultaneous electrodeposition of nanoplatinum and chitosan (CHI/Pt) to fabricate a biomimetic nanostructure that actuates under pH changes.

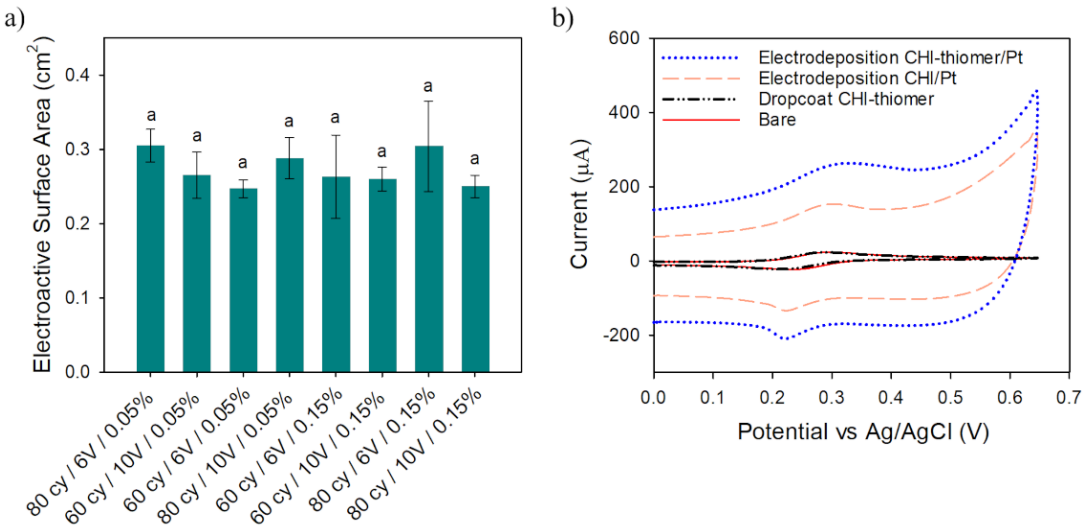

Figure 3.4 Electrochemical characterization of electrodes using 4 mM K_4FeCN_6 as redox probe. (a) Average electroactive surface area (ESA) for various electrode modifications with different number of cycles (cy), voltages (V) and chitosan concentration (wt.%). (b) Representative CV curves at 100 mV/s scan rate of bare Pt/Ir, dropcoated CHI-thiomer and best conditions for CHI/Pt (80 cycles / 6 V / 0.05% CHI) and CHI-thiomer/Pt (60 cycles / 6 V / 0.15% CHI-thiomer) brush depositions. All data represent the average of three replicates and error bars represent the standard deviation of the arithmetic mean; letters denote significantly different means ($p < 0.05$).

3.3.3. Actuation of nanobrushes

Chitosan is a polycationic polymer with pKa around 6.5 (Strand, Tømmeraas, Vårum, & Østgaard, 2001). Below pKa, chitosan's amines are protonated, the polymer has a high charge density and electrostatic repulsions between monomeric units tend to

stiffen the chain leading to an extended conformation (Berger et al., 2004; Cheng et al., 2010). At higher pH, the amines become deprotonated and ionic repulsions are reduced thus allowing the individual chains to collapse (Cheng et al., 2010). To characterize the electrostatic interactions during polymer actuation, CV was performed with three different redox probes at various pH, including a negatively charged probe ($KFeCN_6^{3-}$), a neutral probe ($C_6H_4(OH)_2$), and a positively charged probe $Ru(NH_3)_6^{3+}$. Figure 3.5 shows the average ESA values for replicate sensors at pH 4 or pH 8 during three repetitive cycles. At lower pH, electron transport increased with the negative probe ($KFeCN_6^{3-}$) due to electrostatic interactions with positively charged chitosan; and with the positive probe ($Ru(NH_3)_6^{3+}$) the opposite occurred due to charge repulsion/steric hindrance. Above the pKa (pH 8) the trend in CV data was reversed, with reduction of peak current on the negative probe, while with the positive probe the electron transfer was favored increasing ESA. Due to the lack of charge of the neutral probe the influence of pH was almost negligent. Similar results were observed previously by Hills et al. (2018) with non-modified chitosan electrodeposited onto a reduced graphene oxide/nano-platinum coated electrode, which demonstrated that simultaneous deposition of chitosan with platinum studied here did not affect chitosan's stimulus response to pH changes and actuation properties. Some degree of hysteresis can be observed in Figure 3.5 after repeated actuation of the CHI/Pt brush, as the ESA gradually decreased after each repetition. This behavior was also noticed by Giacobassi et al. (2021) during the actuation of PNIPAAm nanobrushes with temperature stimuli. Actuation tests were also performed with the CHI-thiomer/Pt brush electrodes to test if the modification of

chitosan had any effect on its pH stimuli actuation property (see Figure B6 in Appendix B).

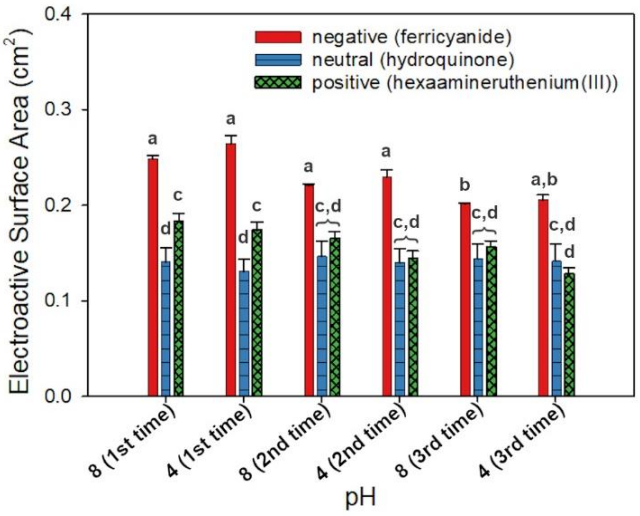

Figure 3.5 Electrostatic interactions during chitosan actuation for various redox probes: a negatively charged probe ($KFeCN_6^{3-}$), a neutral probe ($C_6H_4(OH)_2$), and a positively charged probe ($Ru(NH_3)_6^{3+}$. The average electroactive surface area (ESA) is shown for each redox probe under repeated actuation at pH 4 and pH 8 (n = 3), indicating some degree of hysteresis. Error bars represent the standard error of the arithmetic mean; letters denote significantly different means ($p < 0.05$).

Hills et al. (2018) and Giacobassi et al. (2021) demonstrated that the actuation of stimuli-responsive polymers in stagnant media improves bacteria capture (relative to no actuation). The authors reported improved sensing performance when cell capture was in the extended conformation during capture (EX/cap) followed by collapse of the nanobrush during the measurement (COL/meas). This could be due to 1) the increased probability of aptamer-cell interaction in the extended phase; and 2) electrostatic attraction between the CHI and *L. monocytogenes* below pH 6, as CHI is positively charged and under most conditions *L. monocytogenes* membrane is highly negatively charged (Briandet et al., 1999; Hills et al., 2018). Based on the actuation results obtained

in this study that corroborate with the results obtained by Hills et al. (2018) and Giacobassi et al. (2021), the previously established actuation protocol (i.e., EX/cap followed by COL/meas) was used for the sensing experiments with bacteria described in the next section.

3.3.4. Bacteria sensing

Based on the principle that binding of target bacteria to the aptamer decreases the electron transfer at the electrode, which is measured as an increase of impedance, EIS analysis was performed to determine impedance differences caused by bacteria presence. All tests used the actuation protocol of capture in the extended state at pH 4 and sensing in the collapsed state at pH 8 (Giacobassi et al., 2021; Hills et al., 2018) and included 15 min for bacteria capture and 2 min for the EIS measurement. The CHI/Pt brush electrodes functionalized with an aptamer concentration of 1000 nM were tested with increasing concentration of *L. monocytogenes* (ranging from 100 to 10^6 CFU/mL). See Appendix B for details on the nanobrush functionalization (methods and results, Figure B7). Bode plots (Figures 3.6 and 3.7) are shown over a frequency range of 1 Hz to 100 kHz; insets are a zoomed in view of the lower frequency range (1-5 Hz).

Bacteria detection was first assessed in PBS at room temperature. As it can be observed on the Bode plots (Figures 3.6a and 3.6b) at higher frequencies (above 10 Hz) the impedance values overlapped, while at lower frequencies the impedance values consistently increased with the increase in bacteria concentration. For the frequency cutoff (CF) analysis (Figure 3.6c), the maximum impedance signal was obtained at a CF

of 1 Hz, which was used to determine the calibration curves and limit of detection (LOD, 3 sigma; 99.5% confidence interval). This analysis considered frequencies from 1 to 50 Hz, which falls within the alpha frequency dispersion region in biological tissues (Dean, Ramanathan, Machado, & Sundararajan, 2008).

Figure 3.6d shows that impedance increased linearly for the CHI/Pt-aptamer nanohybrid electrode when calibrated in PBS with *L. monocytogenes* and in the presence of equal background concentration of *S. aureus* (interferent) with range of detection of 10^1 to 10^6 CFU/mL. *S. aureus* was the bacteria chosen for selectivity testing due to its similarity to *Listeria* with both being Gram-positive and both being known foodborne pathogens. The LOD of the CHI/Pt-aptamer brushes when only *Listeria* was present in PBS was 2.5 ± 0.3 CFU/mL and its sensitivity was 21.1 ± 4.4 Ω/log(CFU/mL). The addition of *S. aureus* in the testing solution did not show significant interference ($p > 0.05$) on the CHI/Pt-aptamer brushes performance, with LOD of 2.6 ± 1.6 CFU/mL and sensitivity of 27.8 ± 3.5 Ω/log(CFU/mL), which indicates no cross-reaction between *S. aureus* and the aptamer, and consequently high aptamer selectivity to *L. monocytogenes*. Comparing to the results of the CHI/Pt brush not functionalized with the aptamer (plots presented in Figure B2 in Appendix B), in PBS with only *L. monocytogenes* the LOD and sensitivity (3.1 ± 0.0 CFU/mL and 26.7 ± 5.5 Ω/log(CFU/mL), respectively) are similar ($p > 0.05$) to CHI/Pt-aptamer functionalized brush. While the inclusion of *S. aureus* significantly increased the LOD (11.0 ± 0.4 CFU/mL), reduced the sensitivity (11.3 ± 1.2 Ω/log(CFU/mL)) and the detection range to 10^1 to 10^5 CFU/mL for CHI/PT brush without aptamer functionalization. Abdelhamid & Wu (2013b) showed that the

interactions between chitosan and bacteria are entropically driven and the binding processes are spontaneous. The authors determined that chitosan has multifunctional forces on bacteria (hydrophobic, hydrogen bond, and electrostatic interactions) which are complementary and can reinforce each other. This can explain the higher LOD when the CHI/Pt brushes without aptamer functionalization was tested with both *L. monocytogenes* and *S. aureus* in PBS as both bacteria are prone to bind to chitosan. Additionally, these results demonstrated that the actuation protocol plays a major role on bacteria capture and can be used as a first step in food safety monitoring. These results also reinforced that the aptamer is highly selective to *L. monocytogenes* improving the overall CHI/Pt-aptamer brush sensing performance.

Figure 3.7 shows results of the analysis in chicken broth to evaluate the CHI/Pt-aptamer brush sensing performance in a real food. Chicken broth was chosen as an example of complex media that presents carbohydrates and proteins, among other components, that could interact with the biosensor through non-specific adsorption resulting in a false-positive signal. The LOD remained similar (3.3 ± 0.9 CFU/mL, $p > 0.05$) and the sensitivity significantly increased (89.3 ± 0.4 Ω/log(CFU/mL)) when testing in chicken broth compare to sensing in PBS. When the CHI/Pt platform without aptamer was tested in the same conditions (Figure B3 and Table B1 in the Appendix B), the LOD was significantly higher (22.0 ± 1.3 CFU/mL) and the sensitivity lower (43.1 ± 13.3 Ω/log(CFU/mL)). One more time demonstrating that the aptamer efficiency to selectively bind to *L. monocytogenes* even in the complexity of a food matrix as well as the ability to capture bacteria applying the actuation protocol to the CHI/Pt brushes.

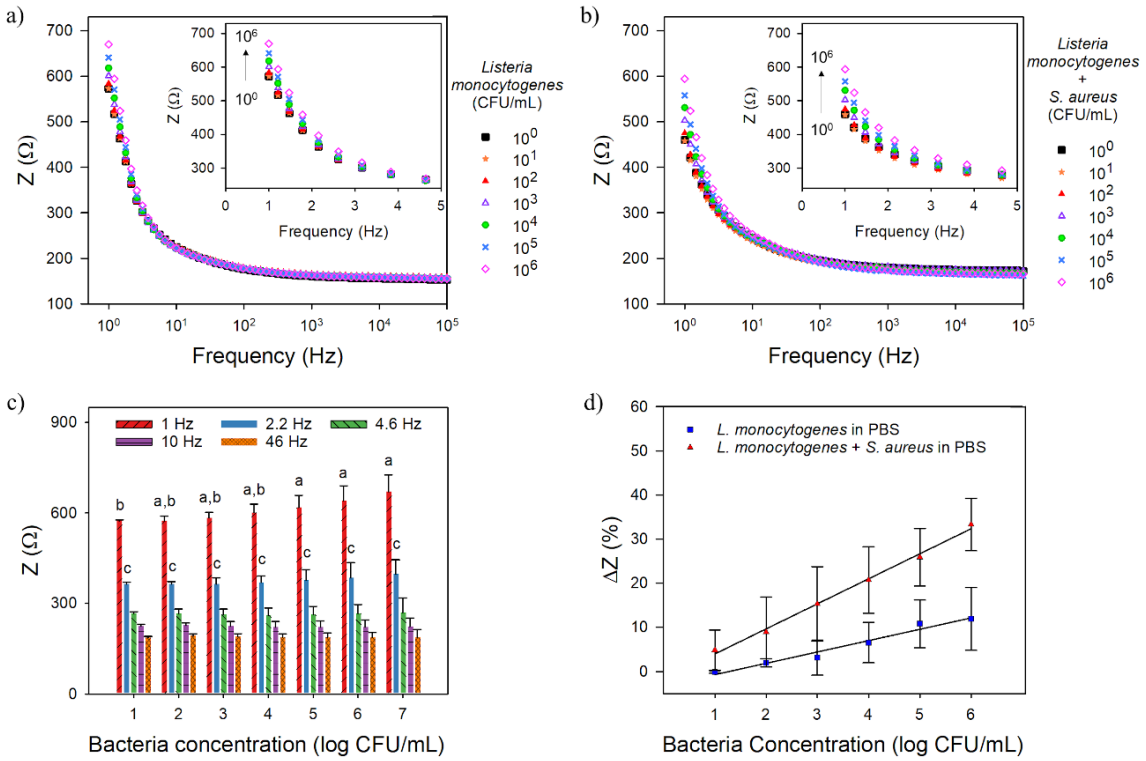

Figure 3.6 Representative Bode plots over the frequency range of 1-100,000 Hz (inset show exploded view over the frequency range from 1-5 Hz) for the CHI/Pt brush sensor functionalized with 1000 nM aptamer exposed to a) *L. monocytogenes* in PBS and b) *L. monocytogenes* + *S. aureus* in PBS. c) Average impedance at different cutoff frequencies with *L. monocytogenes* in PBS. There was no significant difference among frequencies 4.6, 10 and 46 Hz but the other cutoff frequencies (1.0 Hz and 2.2 Hz) are significantly higher. d) Calibration curves (impedance change at 1 Hz vs. log bacteria concentration) for a) and b). All data represents the average of three repetitions. Error bars represent the standard deviation; letters in plot c) denote significantly different means ($p < 0.05$).

The CHI-thiomer/Pt-aptamer nanohybrid electrodes provided very inconsistent results when tested with bacteria (Figure B8 in Appendix B). The electrostatic forces between the negative charges of the bacteria and polycationic sites of chitosan (Abdelhamid & Wu, 2013b) can explain the better performance of the non-modified chitosan compared to the CHI-thiomer, as some of the cationic sites of chitosan were unavailable after the modification.

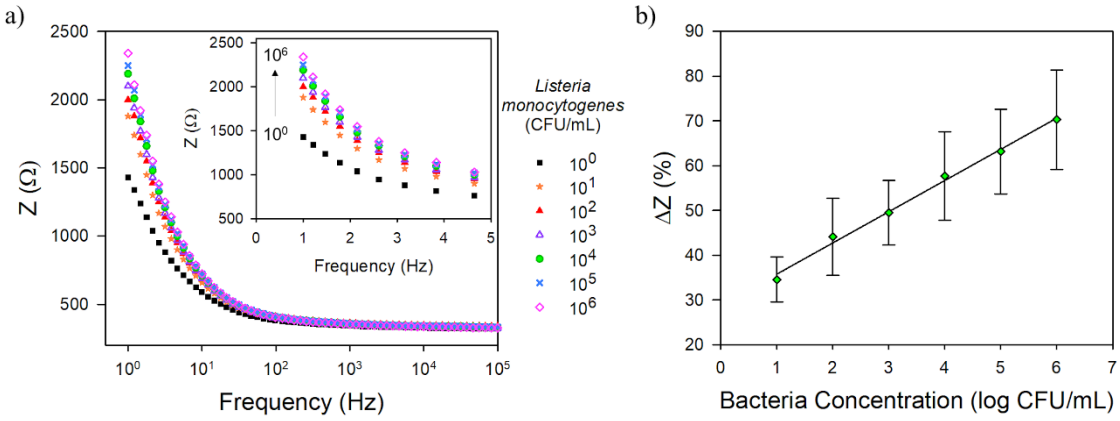

Figure 3.7 a) Representative Bode plot over the frequency range of 1-100,000 Hz (inset show exploded view over the frequency range from 1-5 Hz) and b) calibration curve (impedance change at 1 Hz vs. log bacteria concentration) for the CHI/Pt brush sensor functionalized with 1000 nM aptamer exposed to *L. monocytogenes* in chicken broth. All data represents the average of three repetitions. Error bars represent the standard deviation.

Table 3.1 contains a compilation of the application of chitosan and/or aptamers for the detection of different bacteria in various food samples or buffers. The detection limit and detection time for the actuating CHI/Pt brush sensor studies here was less than or equal to the LODs and response times reported in the literature, except for Zelada-Guillén, Bhosale, Riu, & Rius (2010) who reported an aptasensor for *E. coli* CECT 675 in milk with a LOD of 6 CFU/mL and detection time ranging from 2 to 20 min. For *Listeria* spp. detection, the LOD of CHI/Pt brush sensor was lower than all biosensors shown in Table 3.1 with similar detection times. Radhakrishnan, Jahne, Rogers, & Suni (2013) achieved a LOD of 4 CFU/mL for *L. monocytogenes* in filtered tomato extract with a gold electrode-based immunosensor and EIS acquisition time of 2.8 minutes; however, with an electrode area (0.19 cm^2) ten times larger than the electrode used here.

R. Wang et al. (2008) developed a TiO_2 nanowire bundle based immunosensor functionalized with anti-*Listeria* antibodies that can detect as low as 10^2 CFU/mL and up to 10^7 CFU/mL of *L. monocytogenes* in 1 h without significant interference from other foodborne pathogens; however, no linear correlation was found. Guo et al. (2020) proposed aptamer and antibody-based dual recognition units using aggregation-induced emission nanoparticles and magnetic nanoparticles and reported a range of detection for *L. monocytogenes* of 10-10^6 CFU/mL after a 90 min incubation time. Using the same aptamer as in the present work, Ohk et al. (2010) presented a LOD of 10^3 CFU/mL for a fiber-optic biosensor to detect *L. monocytogenes*. Sidhu et al. (2016) reported a LOD of 5.39 CFU/mL of *L. monocytogenes* in PBS with the same detection time and the same aptamer as in this work using platinum interdigitated array microelectrodes. Hills et al. (2018) studied an actuating nanobrush consisting of reduced graphene oxide/nano-platinum/chitosan functionalized with the same aptamer used in the present work and reported similar LOD values (3.0 and 9.1 CFU/mL in PBS and vegetable broth, respectively). One of the main advantages of the CHI/Pt brush studied here was the faster fabrication with only one-step deposition followed by functionalization, while Hills et al. (2018) used a 3-step fabrication procedure before functionalization. The performance of the nanobrush biosensors develop here demonstrated that this device has potential to be used in similar complex solutions, including brine water, aquaponics water, and other food samples that are suspended in water and diluted. A significant advantage of the biosensors in this work was the lack of bacteria purification or concentration steps, see for example Heo et al. (2014) that required 4 h incubation prior

to DNA extraction to achieve a detection limit of 10^0 to 10^2 CFU/g or mL, depending on the food, by real-time PCR.

Some reports in the literature used chitosan combined with other materials for the detection of heavy metal, food colorants, cancer biomarkers, among others (Hwang et al., 2019; Tabasi, Noorbakhsh, & Shari, 2017). Other authors used the high electrostatic affinity of positively charged chitosan toward negatively charged bacterial cell membranes to detect bacteria. Le, Tran, & Kim (2020) developed a colorimetric method using the peroxidase-like activity of chitosan-coated iron oxide magnetic nanoparticles that allowed the rapid detection of bacterial cells (*Escherichia coli* and *Staphylococcus aureus*) down to 10^4 CFU/mL by the naked eye and 10^2 CFU/mL by spectrophotometry within 10 min. Abdelhamid & Wu (2013a) also reported detection of 10^2 CFU/mL *Pseudomonas aeruginosa* and *S. aureus* in blood samples using a graphene magnetic nanosheet decorated with chitosan biosensor and fluorescence spectroscopy as transduction method. Therefore, the combination of chitosan with other materials such as aptamer offers many research opportunities for the detection of different components and bacteria.

Table 3.1 Biosensor performance comparison to other devices in the literature using chitosan and/or aptamer for bacteria detection.

Biorecognition agent and platform	**Bacteria**	**Detection mode**	**Test medium**	**Detection range* (CFU/mL)**	**Response time (min)**	**Reference**
CHI/Pt + aptamer	*L. monocytogenes*	Impedimetric	PBS	2.5 - 10^6	17	This work
CHI/Pt + aptamer	*L. monocytogenes*	Impedimetric	PBS + *S. aureus*	2.6 - 10^6	17	This work
CHI/Pt + aptamer	*L. monocytogenes*	Impedimetric	Chicken broth	3.3 - 10^6	17	This work
rGO-nPt + CHI + aptamer	*L. monocytogenes*	Impedimetric	Vegetable broth	9.1 - 10^2	17	(Hills et al., 2018)
Pt-IDEs + aptamer	*L. monocytogenes*	Impedimetric	PBS	5.39 - 10^6	17	(Sidhu et al., 2016)
GCE-NCs + aptamer	*P. aeruginosa*	Impedimetric	PBS	3 - 10^7	30	(Sarabaegi & Roushani, 2019)
rGO-CHI + aptamer	*Salmonella Typhimurium*	DPV	PBS	10 - 10^7	Not reported	(Dinshaw et al., 2017)

Table 3.1 Continued

Biorecognition agent and platform	Bacteria	Detection mode	Test medium	Detection range* (CFU/mL)	Response time (min)	Reference
AuNC-chitosan + aptamer	*S. aureus*	Colorimetric	PBS	10^2 - 10^7	> 35	(Xie et al., 2019)
SWCNT + aptamer	*E. coli CECT 675*	Potentiometric	Milk Apple juice	6 - 10^4 26 - 10^4	2 - 20	(Zelada-Guillén et al., 2010)
SWCNT + aptamer	*Salmonella Typhi*	Potentiometric	PBS	1 - 10^3	1 - 30	(Zelada-Guillen, Riu, Düzgün, & Rius, 2009)

* lowest value corresponds to the lower limit of detection (LOD)

rGO: reduced graphene oxide; nPt: platinum nanoparticle; GCE: glassy carbon electrode; NC: nano-sized chitosan particles; AuNC: gold nanoclusters; DPV: differential pulse voltammetry; SWCNT: single-walled carbon nanotubes

3.4. Conclusions

There is an urgent need for a rapid, reliable, and cost-effective method for detection of foodborne pathogens in the food industry as public health and economic losses due to disease outbreaks and recalls of contaminated food are a real concern. A

facile method for fabrication of chitosan-nanoplatinum brush sensing platform using a co-electrodeposition procedure was successfully demonstrated. The use of chitosan with nanoplatinum brush interfaces in combination with aptamers were shown to significantly enhance the capture of target *L. monocytogenes* bacteria and transduction of electrochemical signal as the acquisition method. The actuation protocol consisted of capture bacteria at pH 4 when chitosan nanobrushes were extended, and initiate test sequence at pH 8 when the brushes were collapsed, which demonstrated to be very efficient to capture bacteria even in the absence of a biorecognition agent (i.e., *Listeria* aptamer) and could be used as a first step for food safety monitoring. Expanded brushes exposed both biorecognition agents and chitosan amine groups to bacteria to easily bind, while collapsed brushes assisted in electrochemical signal transduction. The combination of aptamer binding and polymer entrapment are the likely mechanism for the improved sensing performance.

Optimized conditions provided a sensitive, selective, and label-free sensor for the detection of low concentrations of *L. monocytogenes*, even in the presence of interferents. The relatively high sensitivity of the developed sensor could be attributed to the combination of chitosan, which has strong affinity towards bacteria due to the presence of an amine group ($-NH_2$), and aptamers that are developed to bind specifically to a target membrane protein in *L. monocytogenes*. The LOD of CHI/Pt-aptamer brush sensor for *L. monocytogenes* in PBS was 2.5 CFU/mL (sensitivity of 21.1 ± 4.4 Ω/log(CFU/mL)) and, to simulate a real-world complex sample, chicken broth was used, which resulted in a LOD 3.3 CFU/mL (sensitivity of 27.8 ± 3.5 Ω/log(CFU/mL)). Other

sensors in literature may have comparable detection limits and sensitivities obtained in the present work; however, the developed sensor had several advantages: 1) preparation involved only one-step deposition; 2) no labeling necessary; 3) no bacteria concentration required; it only requires control of the pH on the sample and measurement solutions; and 4) it was one of the fastest response times with total response time of 17 minutes including sample exposure and testing. Additionally, the use of aptamers over antibodies in regard to production cost and shelf-life make CHI/Pt-aptamer brush sensor a potential alternative to current detection methods for testing food samples. Overall, the sensing platform developed in this study could be customized with different biorecognition agents for future electrochemical sensing applications.

CHAPTER IV LASER-INDUCED GRAPHENE WITH NICKEL OXIDE NANOPARTICLES ELECTROCHEMICAL IMMUNOSENSOR FOR RAPID AND LABEL-FREE DETECTION OF *SALMONELLA ENTERICA* TYPHIMURIUM

4.1. Introduction

Currently, there are more than 250 diseases that are caused by foodborne pathogens of which 91% are of bacterial origin (Bintsis, 2017; CDC, 2018). The most common illnesses resulting from unsafe food are diarrheal diseases which can be severe, especially for young children. The World Health Organization (WHO) estimates that 550 million people worldwide fall ill each year, including 220 million children under the age of 5 years, with *Salmonella* as one of the four key global causes of diarrheal diseases (WHO, 2018). In the U.S., a reported 35% of those cases were attributed to *Salmonella* (Dewey-Mattia, Manikonda, Hall, Wise, & Crowe, 2018), the most common culprit of foodborne illnesses. An estimated 1.35 million illnesses are thought to be caused every year by *Salmonella* in the United States, with approximately 26,500 hospitalizations and 420 deaths (CDC, 2021b). Additionally, the 2015 report of the Economic Research Service (ERS) of the U.S. Department of Agriculture (USDA) ranked *Salmonella* first in terms of economic burden - estimated at $3.7 billion a year - among the 15 pathogens included in the study (Hoffmann et al., 2015). In 2020 alone, 71 food product recalls happened due to contamination or potential contamination by *Salmonella* (FDA, 2021). Current techniques for detecting pathogens, such as total viable counts (TVC), polymerase chain reaction (PCR), and enzyme-linked immunosorbent assays (ELISA),

are time consuming and costly as they require laboratory conditions with highly trained personnel while some tests require environmentally hazardous reagents. Despite research efforts, the detection of *Salmonella* still takes an average of ~24-48 h due to a required pre-enrichment process usually followed by a selective enrichment step (Vanegas, Gomes, et al., 2017; Vanegas et al., 2016). Amplifying the bacteria is necessary as current testing methods lack sensitivity (~100 CFU/mL limits of detection (LOD)) and cannot detect lower levels (1-5 CFU/mL) of pathogens in complex samples like media, broth, or homogenized tissue (Vanegas, Gomes, et al., 2017; Vanegas et al., 2016). As government regulations become more rigorous, there is a critical need for improved detection tools to monitor food safety before food processors ship to consumers and consequently mitigate the economic burden of recalls and threats to public health.

Most biosensors for targeting pathogens use electrochemical-based sensing, although optical devices have been developed as well (Arora, Sindhu, Kaur, Dilbaghi, & Chaudhury, 2013; McLamore et al., 2021). Electrochemical impedance-based biosensors circumvent the above challenges for non-laboratory-based testing by offering relatively facile fabrication procedures, label-free operation, and rapid (~20 min) in-field sensing (Arora et al., 2013). Electrochemical devices allow for easy miniaturization without compromising signal acquisition and can circumvent the challenges associated with fluorescence/optical based sensors that require complex equipment/processes (e.g., fluorescence microscopes, pre-labeling steps) and can be affected by turbid, optically dense, or autofluorescent biological samples (McLamore et al., 2021). In order to improve biosensor performance in complex food matrices, biorecognition agents are

attached to nanostructure transducer materials including metallic particles (gold, silver, platinum, nickel, copper) and carbon allotropes (carbon nanotubes, graphene, carbon quantum dots), which demonstrate superior electron-transfer kinetics and signal stability, resulting in improved response time, limit of detection, and sensitivity (W. Huang et al., 2017). Nanostructured conducting allotropes of carbon such as carbon nanotubes, carbon quantum dots, graphene, and graphene oxide, have proven to be a promising material for energy and sensing applications due to their mechanical strength, electrochemical properties, and inert nature (Wallace et al., 2010).

Graphene in particular is characterized by high electrical conductivity, high mechanical strength, large surface area, and chemical stability that provides an excellent platform for biosensing (Lawal, 2018). Challenges with realizing graphene-based electronics lie in relatively complex fabrication procedures, which have generally included chemical vapor deposition (CVD) and/or complex substrate-transfer techniques. A promising alternative is laser-induced graphene (LIG), which is produced by a one-step direct CO_2 laser-scribing process applied to carbon-based polymer films (i.e., polyimide) under ambient conditions that forms 3D graphene layers by photothermally converting sp^3-hybridized carbon found in the substrates into sp^2-hybridized carbon, the carbon allotrope found in graphene (J. Lin et al., 2014). Additionally, LIG can be processed with tunable conductivity, 3D nanostructure topology, and superhydrophobicity, enabling the fabrication of distinct circuit patterns (by directly uploading CAD designs to the CO_2 laser), using relatively inexpensive materials (Soares et al., 2020). LIG fabrication is inherently scalable and cost-effective

as it does not require prior patterning of the substrate with a metal catalyst, chemical etching/cleaning techniques, or annealing procedures commonly used on graphene produced through ink-jet printing (Secor, Prabhumirashi, Puntambekar, Geier, & Hersam, 2013), aerosol-jet printing (Parate, Rangnekar, et al., 2020), and chemical vapor deposition (CVD) (Jin et al., 2011) methods to improve the electrical conductivity and electrocatalytic nature (Garland et al., 2018; J. Lin et al., 2014). LIG has become a popular transducer material for electrochemical sensing applications as a result of its rapid and scalable fabrication method and has been used for sensing several targets which includes glucose in 0.1 M NaOH aqueous solution (Tehrani & Bavarian, 2016), ascorbic acid, dopamine, and uric acid in phosphate buffered saline (PBS) (Nayak et al., 2016), tyrosine and uric acid in sweat (Y. Yang et al., 2020), thrombin in serum (Fenzl et al., 2017), nitrogen in soil (Garland et al., 2018), and biogenic amines in fish samples. (Vanegas et al., 2018). Foodborne pathogen sensing with LIG, *Salmonella enterica* was first demonstrated by Soares et al. (Soares et al., 2020) in chicken broth. Results from this study show a broad linear range (25 to 10^5 CFU/mL), a low detection limit (13 ± 7 CFU/mL), and average response time of 22 min (Soares et al., 2020), which demonstrates the feasibility of LIG as a transducer for pathogen immunosensing; however, the low pathogen detection limits (≤ 5 CFU/mL) required for ensuring pathogen-free food products are still needed.

Researchers have combined hybrid nanomaterials with LIG including heteroatom doping (Xia et al., 2020), such as boron and nitrogen and composite self-assembly such as metals (i.e., gold, silver and platinum nanoparticles) (Z. Wan et al., 2020), to further

improve electrochemical performance including enhanced electron transport, surface wettability, stability, and biorecognition agent immobilization (Ye et al., 2015). However, most doping processes require external heteroatom sources including addition of urea as a precursor or plasma treatment with nitrogen gas (Xia et al., 2020). Additionally, the self-assembly process is commonly carried out via electrodeposition and atomic layer deposition (Z. Wan et al., 2020), which require use of multiple reagents, sophisticate equipment, and delicate control of reaction time and temperature. Recently, Xia et al. (2020) demonstrated direct deposition of metal nanoparticles (gold, silver, palladium, lead, and platinum) using a 532-nm laser by laser induced reduction of metal ions on the graphene film. In another study, researchers demonstrated electroless deposition of platinum and nickel oxide nanoparticles into graphene as a simple one-pot synthesis process offering multiple advantages compared to commonly used methods to fabricate electrocatalysts such as solid-phase reaction and hydrothermal processes (Kucherenko et al., 2021). NiO nanoparticles on a graphene platform have been used to fabricate energy storage devices (Chu et al., 2016; D. Wang et al., 2010; Z. Wu et al., 2012), supercapacitors (Zhi et al., 2013), and fuel cells (Kucherenko et al., 2021). Also, this platform has been used for electrochemical sensing applications, including sensing of environmental pollutants, toxic and hazardous gases, NO_2, and related gases (Niavol et al., 2020). However, its application for detecting foodborne pathogens such as *Salmonella enterica* is yet to be shown.

Herein, it was experimentally demonstrated for the first time a LIG-NiO *Salmonella enterica* sensor that was suitable for rapid in-field analysis of food samples.

An impedimetric immunosensor was developed using a two-step direct writing fabrication method to create LIG with NiO nanoparticles (LIG-NiO) under ambient conditions using polyimide and nickel acetate solution as substrates, which was then converted into a label-free sensor for the detection of *Salmonella enterica* serovar Typhimurium by functionalizing the electrodes with anti-*Salmonella* antibody. The LIG-NiO electrodes displayed 3D porous graphene and NiO nanoparticle structures with high electrical conductivity and electroactive surface area (3-fold larger than the geometric area). The resulting immunosensor was capable of selectively sensing *Salmonella Typhimurium* at concentrations as low as 1.3 CFU/mL in real food (i.e., chicken broth) and in the presence of other Gram-negative cells with negligible interference with a response time of only 17 min, over relevant concentration levels (10^1 to 10^5 CFU/mL) as a food safety monitoring analysis.

4.2. Materials and methods

4.2.1. Materials and bacteria cultures

Polyimide film (0.125 mm thick) was acquired from DuPont (USA). Potassium ferrocyanide trihydrate ($K_4Fe(CN)_6.3H_2O$) was purchased from Ward's Science (Rochester, NY). Potassium ferricyanide ($K_3Fe(CN)_6$) was obtained from J.T. Baker (Phillipsburg, NJ). Reference electrode (Ag/AgCl, 3 M KCl liquid junction) and platinum auxiliary electrode (99.95% Pt, 0.5 mm dia.) were purchased from BASinc. (West Lafayette, IN). Conductive silver ink was purchased from Ted Pella, Inc. (Redding, CA). SuperBlock in phosphate buffered saline (PBS), which was used as the

blocking buffer, 1-ethyl-3-(3-dimethylaminopropyl)carbodiimide HCl (EDC), and 2-(N-morpholino)ethanesulfonic acid (MES) were purchased from Thermo Fisher Scientific (Waltham, MA). N-Hydroxysuccinimide (NHS) was obtained from Alfa Aesar (Ward Hill, MA). KPL BacTrace goat anti-*Salmonella* CSA-1 polyclonal antibody was purchased from SeraCare (USA). Commercially sterilized chicken broth was purchased from a local grocery store. Tryptic soy broth (TSB), Tryptic soy agar (TSA), and buffered peptone water (BPW) were purchased from Becton, Dickson and Company (Sparks, MD). Potassium nitrate (KNO_3) was purchased from British Drug Houses (ON, Canada). Tris EDTA (TE) buffer pH 7.4 was purchased from Quality Biological (Gaithersburg, MD). Sodium chloride (NaCl) and potassium chloride (KCl) were acquired from EMD Millipore Corporation (Burlington, MA). Nickel (II) acetate tetrahydrate was purchased from Sigma-Aldrich (St. Louis, MO). All the chemicals used in this study were of analytical grade. Solutions were made using deionized water (18.2 MΩ-cm).

Salmonella enterica subsp. enterica serovar Typhimurium (ATCC 43971) and *Escherichia coli* (ATCC 35218) were stored at -80 ^{o}C and were initially replicated in TSB using two identical consecutive transfers and incubated at 35 °C for 24 hours under aerobic conditions. Total aerobic plate counts were measured in triplicates by serially diluting samples of the bacteria in BPW and plating on TSA. Bacteria were maintained on TSA and stored at 4°C for no more than 3 months. Both bacteria must be handled using biosafety level 2 standards established by the National Institute of Health.

4.2.2. LIG-NiO electrode fabrication

Figure 4.1 shows a schematic of the fabrication of the LIG-NiO electrodes. Initially, polyimide film (0.125 mm thick, DuPont, USA) was fixed on a glass substrate and cleaned with a wipe. CorelDraw was used to draw the electrode pattern submitted to the laser-controlling program. The polyimide was then irradiated with a 75 W Epilog Fusion M2 CO_2 laser (Epilog Laser, Golden, CO, USA) at ambient conditions (23.0 ± 1.0 ^{o}C). Lasing parameters were experimentally selected to achieve the highest quality of graphene and NiO deposition as follows: 7% speed, 7% power, 50% frequency, raster mode, 600 dpi (dots per inch), and all other parameters were selected as "off". The laser beam was defocused by the placement of polyimide sheet 2 mm lower than the focus distance. These lasing settings were used for the first and second lasing steps.
Next, 15 µL of 1 M nickel (II) acetate tetrahydrate ($Ni(CH_3CO_2)_2{\cdot}4H_2O$) was deposited onto each electrode and allowed to dry for 10 minutes at ambient conditions. Then, running the same etching pattern as before, the CO_2 laser irradiated the LIG a second cycle to induce the thermal decomposition of the nickel salt into nickel (II) oxide and other gases, such as oxygenates, hydrogen with hydrocarbons, and carbon oxides. The total fabrication process time was 12 minutes, consisting of 1 min for first lasing step, 10 min for $Ni(CH_3CO_2)_2{\cdot}4H_2O$ solution dropcoating and drying, and 1 min for second lasing step. Contacts of the LIG-NiO were protected with a conductive silver ink to ensure a good electrical connection with the potentiostat. Fast-drying lacquer (nail polish) purchased locally was applied to the electrode stem between the working area (3

mm diameter) and connector ends to keep a constant working surface area of 0.071 cm^2 in contact with the sample solution during electrochemical sensing.

4.2.3. Material characterization

Morphological and chemical characterization of the LIG-NiO electrodes were conducted by scanning electron microscope (SEM) using a Quanta 600 FEG from FEI (Hillsboro, OR) equipped with an energy dispersive spectroscopy (EDS) system. Images were taken with an operating voltage of 20 kV at 2,000, 10,000, 25,000, and 50,000 times magnification. Sheet resistance was measured using a Hall effect measurement system (MMR H5000) at room temperature with a 4-probe set up over 1 cm^2 area. X-ray photoelectron spectroscopy (XPS), also known as electron spectroscopy for chemical analysis (ESCA), was used to analyze the surface chemistry. XPS analysis was performed in an Omicron ESCA+ (Scienta Omicron, Sweden) equipped with a Mg/Al dual X-ray gun and CN10 electron gun. CasaXPS 2.3.23PR1.0 and XPSPEAK 4.1 were used to process raw data files.

Raman characterization was conducted with a Horiba XploRA Plus confocal Raman microscope using a 532 nm laser (1.2 mW). The LIG-NiO electrode was checked with a 50× objective (NA = 0.50) at 12 randomly selected locations. At each location, the Raman spectrum was collected with 30 s acquisition time and 3 accumulations. In total, 12 Raman spectra for the LIG-NiO electrode were collected. Each Raman spectrum was fitted to a Lorentzian function in Igor Pro 6.37 (WaveMetrics, Portland, OR). The average I_D/I_G peak intensity ratio and average I_{2D}/I_G peak intensity ratio were

calculated from the fitting results. The average Raman spectrum for LIG-NiO electrode was plotted in Igor Pro 6.37 (WaveMetrics, Portland, OR).

4.2.4. Sensor functionalization

The working area of the electrodes was covered with the activation solution that consisted of 0.1 M MES buffer (pH 6.0,), 0.5 M NaCl, 75 µM EDC, 25 µM NHS) for 45 min at room temperature, and then rinsed with sterile water to remove the unreacted EDC/NHS. Next, polyclonal antibody anti-*Salmonella* was applied at different concentrations (75, 150, and 225 µg/mL) to the surface of the working electrode for 1.5 h at 4 °C to determine the optimum antibody concentration for functionalization. The electrode was thoroughly rinsed with PBS (pH 7.2). Next, the electrode surface was covered with Superblock in PBS (~ 20 µL) for 15 min to reduce nonspecific binding and rinsed off with PBS prior to testing.

4.2.5. Electrochemical characterization

Cyclic voltammetry (CV) and electrochemical impedance spectroscopy (EIS) methods, as described by Hills et al. (2018) and Giacobassi et al. (2021), were used to electrochemically characterize the LIG-NiO electrodes at room temperature. A three-electrode cell system with a platinum auxiliary electrode, an Ag/AgCl reference electrode, and the LIG-NiO as the working electrode was used. CV analysis was performed on a CHI 600E potentiostat analyzer (CH Instruments, Austin, TX) with a 4 mM $[Fe(CN)_6]^{3-}$ in 1 mM KNO_3 solution, 10 sec quiet time, 650 mV switching potential,

and 0.05, 0.10, 0.15, 0.20 and 0.25 V/s scan rates to obtain Cottrell plots and the electroactive surface area (ESA) via Randles-Sevcik theory (Vanegas et al., 2018). EIS analysis was performed in a 4 mM $[Fe(CN)_6]^{3-}/[Fe(CN)_6]^{4-}$ in 1 mM KCl solution with a frequency range of 1-100,000 Hz, 10 mV AC amplitude, and 0 V initial DC potential using a PalmSens4 potentiostat (PalmSens, Netherlands). Complex plane diagrams (Nyquist plots) were used to determine the charge transfer resistance (R_{ct}), the solution resistance (R_s), the double-layer capacitance (C_{dl}), and the Warburg element (Z_w) by fitting the EIS data sets to a Randles equivalent circuit through an EIS spectrum analyzer from ABC Chemistry (Minsk, Belarus) (Soares et al., 2020).

4.2.6. Biosensor performance testing

EIS analysis was used to determine the limit of detection (LOD), range, sensitivity, and selectivity of each immunosensor when exposed to bacteria at concentrations ranging from 10^0 to 10^6 CFU/mL with an incubation time of 15 min under 200 rpm and analysis time of 2 min. Between each measurement, the immunosensors were washed thoroughly with PBS to remove unbound bacteria. Calibration plots were obtained by measuring the charge transfer resistance (R_{ct}) for each successive bacteria concentration using the same EIS parameters as previously described. Sensitivity testing was performed in PBS and sterile chicken broth. Selectivity to the target bacteria was measured by determining sensitivity, LOD, and range in the presence of Gram-negative bacteria, *E. coli* spp., in PBS.

4.2.7. Data analysis

All experiments were performed at least in triplicates and analyzed using one-way analysis of variance ANOVA to test for significance. Results were expressed as mean ± standard deviation. Statistical significance was expressed at the $p < 0.05$ level; significantly different means were separated by the Tukey test. The slope of the linear portion of the calibration curve was used to determine the sensitivity, the LOD was calculated using the 3σ method (99.5% confidence interval), and the range was calculated as the linear portion of the calibration curve ($R^2 > 0.98$) (Soares et al., 2020).

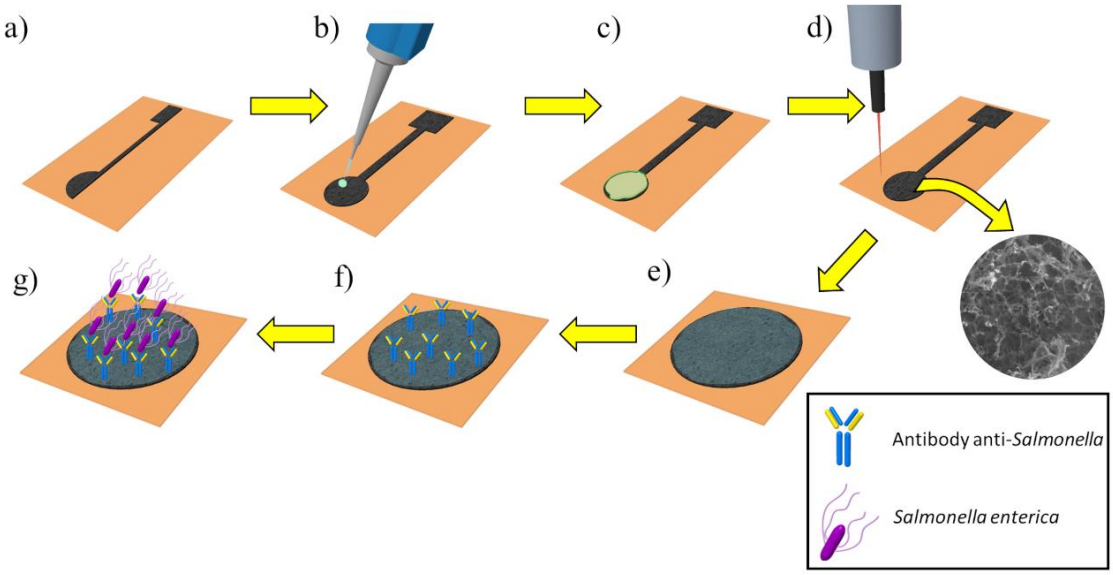

Figure 4.1 Fabrication and functionalization schematic of LIG-NiO sensor for *Salmonella* spp. detection. a) First laser treatment of polyimide film to create LIG working electrode; b) dropcoating of nickel (II) acetate solution; c) air drying of electrode surface; d) second laser treatment to convert nickel (II) acetate solution into NiO, SEM image showing LIG-NiO surface; e) EDC/NHS surface activation; f) antibody anti-*Salmonella* functionalization via carbodiimide crosslinking chemistry; and g) *Salmonella* Typhimurium binding to the electrode for subsequent electrochemical detection.

4.3. Results and discussion

4.3.1. Material characterization

XPS analysis was performed on the LIG-NiO electrodes to determine the elemental composition. The XPS survey spectrum (Figure 4.2a) shows peaks of C 1s, O 1s, and Ni 2p. The C 1s spectrum show a characteristic peak of LIG at 284.3 eV, corresponding to the sp^2 carbon from graphene (Bianchi, Cattania, & Villa, 1993). Figure 4.2b shows the Ni 2p spectrum with a doublet at 853.7 and 855.5 eV and another peak at 861 eV, similar to peaks previously observed in NiO (Bianchi et al., 1993; K. S. Kim & Davis, 1972; Payne, Biesinger, & Mcintyre, 2012; J. Zhang, Ren, Li, & Tour, 2018). The O 1s spectrum (Figure 4.2c) presents a doublet with peaks at 529.5 and 531.4 eV. J. Zhang et al. (2018) attributed a peak at ~532 eV to oxygen-containing moieties such as C−O and C=O from LIG and a peak at ~530 eV to metal oxides. The same authors assigned a peak at ~853 eV to the existence of a small amount of elemental nickel (Ni^0) resulting from the reduction of Ni^{2+} at high temperatures induced by the laser. According to Bianchi et al. (1993) and K. S. Kim & Davis (1972), the O 1s peak at 529.5 eV derives from oxygen in NiO, while the peak at 531.4 eV is associated with the more intense peak of Ni 2p at 855.5 eV and could indicate the presence of Ni_2O_3, related to the formation of ion Ni^{3+} possibly due to a cation defect in the lattice.

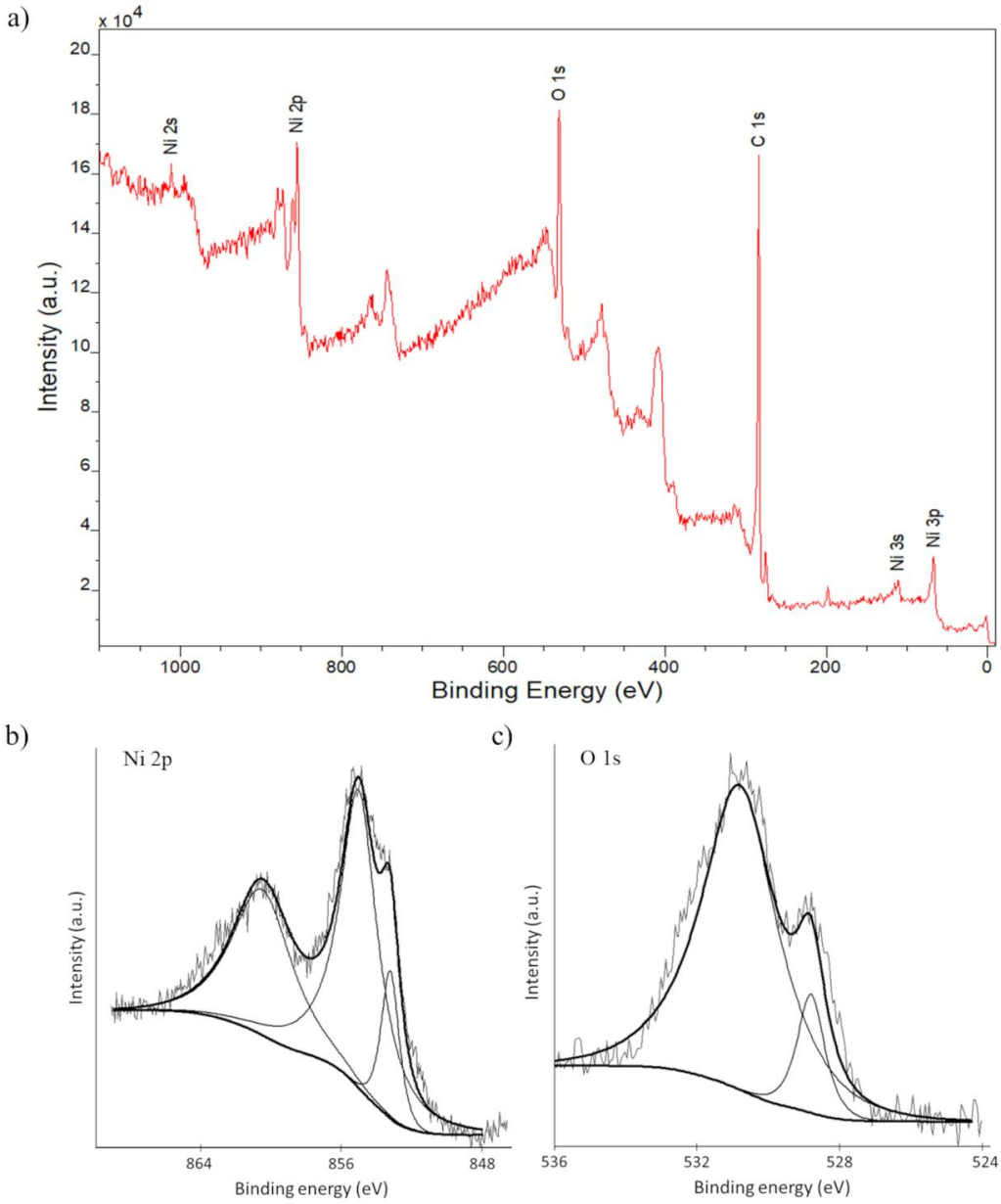

Figure 4.2 X-ray photoelectron spectroscopy (XPS) analysis of LIG-NiO electrode. a) survey spectrum, b) Ni 2p spectrum, and c) O 1s spectrum showing predominantly sp^2 carbon and NiO in the LIG-NiO electrode.

Figure 4.3 shows SEM images used to characterize the surface topography of the LIG-NiO electrodes. A highly porous 3D honeycomb like structure with pores ranging

from 200 nm to 14 µm can be observed in Figure 4.3a-c. Similar porous structures were presented by Soares et al. (2020) for LIG and J. Zhang et al. (2018) for LIG and LIG-NiFe as the lasing process converts the carbon of aromatic compounds from polyimide film into porous graphitic structures (J. Lin et al., 2014). The energy from the first laser irradiation results in lattice vibrations leading to extremely high localized temperature that converts the sp^3 carbon into sp^2 by photothermal effects (J. Lin et al., 2014) while the second lasing induces the thermal decomposition of nickel acetate tetrahydrate into nickel oxide (NiO). NiO nanoparticles with estimated size of 25 nm can be observed in Figure 4.3d. An enhanced electrochemical capacity is attributed to the 3D network of highly conductive graphene as it confers a larger and more accessible electrochemical surface area, allowing electrolyte penetration more easily into the active area (J. Lin et al., 2014). This 3D porous network also allows the deposition of the NiO nanoparticles which can also improve the electron transfer (Nayak et al., 2016). The high temperature induced by the laser can break C−O, C−N, and C=O originally present in the polyimide film with N_2, H_2, and O_2 being released as gases (J. Lin et al., 2014). The EDS performed on the LIG-NiO electrodes (see Figure C1 in the Appendix C) shows the elements carbon, oxygen and nickel confirming the presence of NiO, while the absence of nitrogen and hydrogen corroborates with the successfully conversion of polyimide into LIG by the laser induction process.

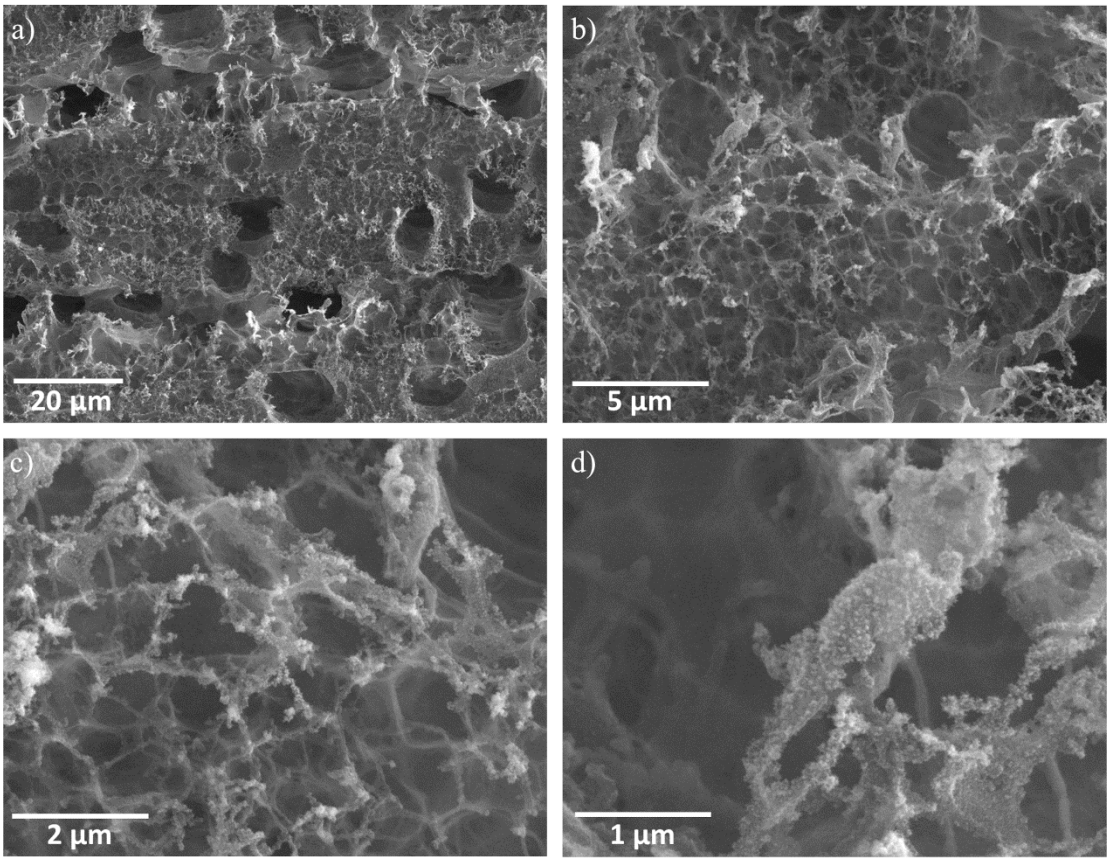

Figure 4.3 Morphological characterization by scanning electron microscopy (SEM) images of the LIG-NiO electrode at 20 kV and a) 2,000, b) 10,000, c) 25,000, and d) 50,000 times magnification showing a highly porous 3D honeycomb like structure with pores ranging from 200 nm to 14 µm and NiO nanoparticles with size of approximately 25 nm.

Raman spectroscopy is a useful technique to determine graphitic properties, including disorder in the resultant sp^2 carbon lattice. The Raman spectra of graphene-based materials predominantly consist of three peaks referred to as D, G, and 2D bands. The extension of the sp^3 to sp^2 conversion can be inferred from the position, shape, and intensity ratio of these peaks (Kurra, Jiang, Nayak, & Alshareef, 2019). Raman characterization of the LIG-NiO electrode (Figure C2 in the Appendix C) revealed three

prominent peaks: 1) the D band at ~1,345 cm^{-1} which suggests the existence of sp^3 centers correlated to defects due to breaking of the translational symmetry of the sp^2 carbon lattice; 2) the G band at ~1,585 cm^{-1} due to C−C stretching vibration of the sp^2 carbon lattice present on all graphitic materials; and 3) the 2D band at ~2,690 cm^{-1} that is distinctive of graphene structures originating from the stacking of graphene sheets along c-axis (Fenzl et al., 2017; Kurra et al., 2019). Kucherenko et al. (2021) attributed the presence of the 2D band in the Raman spectra to the graphitization of a polyimide substrate and formation of graphene layers due to the high local heating by the CO_2 laser. The I_D/I_G ratio and I_{2D}/I_G ratio from Raman analysis can be used to estimate the defects and the number of graphene layers, respectively. The obtained I_D/I_G ratio (0.97 ± 0.06) and I_{2D}/I_G ratio (0.48 ± 0.03) indicate a high degree of disorder and formation of multilayer graphene in the LIG-NiO electrode (Garland et al., 2018; Soares et al., 2020).

4.3.2. Electrochemical analysis

The electrochemical performance of the bare LIG-NiO electrodes was evaluated to determine its ability to act as an electrochemical transducer. Cyclic voltammetry and electrochemical impedance spectroscopy (EIS) analyses were performed in a negatively charged redox probe (4 mM ferricyanide-ferrocyanide mixture). Cyclic voltammograms (see Figure 4.4a) displayed well-defined redox peaks, a quasi-reversible behavior for all scan rates, and a linear increase of anodic peak current (oxidation) and decrease of cathodic peak current (reduction) with scan rates (Figure 4.4b). The electroactive surface area (ESA) of 0.22 ± 0.01 cm^2 was two times higher than reported by Soares et al.

(2020) and Nayak et al. (2016) (ESA = 0.104 ± 0.032 cm^2 and 0.092 ± 0.015 cm^2, respectively) for the same geometric area of the electrode (0.071 cm^2). This result is likely because of the 3D porous structure of graphene, allowing for more exposure of the edge planes to the redox solution (Soares et al., 2020), in addition to the direct electron-transfer between the conductive network of graphene and the NiO nanoparticles, which enhances the electron-transfer kinetics and therefore, increases the ESA (W. Huang et al., 2017). Furthermore, the separation between oxidation and reduction peaks (ΔE_p) ranged from 76 mV at scan rate of 0.05 V/s to 142 mV at scan rate of 0.25 V/s (Figure 4.4a), indicating faster electron transfer rate than reported by Soares et al. (2020) (ΔE_p = 166-245 mV with similar scan rates) and Garland et al. (2018) (ΔE_p = 250 mV with scan rate of 0.025 V/s) for the LIG without NiO. Nayak et al. (2016) reported that platinum nanoparticles improved the electrochemical properties of LIG, including higher ESA and lower peak potential separation, as it seems to be the case in the present work with NiO nanoparticles. These results demonstrate the effective electron transfer kinetics of LIG-NiO fabricated in this study and its suitability for electrochemical sensing. A more efficient electron transfer process is desirable for biosensing applications, specifically affinity-based sensors, since the output signal depends on surface chemistry changes, which are proportional to the ESA as a result of target-biorecognition agent binding and the corresponding change in the electron transfer behavior (Kong, Xu, Xu, & Chen, 2011). Additionally, the LIG-NiO electrodes showed a sheet resistance of 0.13 ± 0.03 $k\Omega\ sq^{-1}$ which is significantly lower than previously reported values of LIG-based electrodes (13-20 $k\Omega\ sq^{-1}$) (Garland et al., 2018; Soares et al., 2020) in addition to being

lower than printed electrodes based on aerosol-jet printed graphene (1.5 kΩ sq^{-1}) (Parate, Pola, et al., 2020), inkjet-printed graphene (0.2 to 1.1 kΩ sq^{-1}) (Das et al., 2016; Secor et al., 2013), and thicker printed graphene films that have been fabricated without binders through polymer casting (0.2 kΩ sq^{-1}) (Uz et al., 2019). Therefore, the sheet resistance further indicates that LIG-NiO electrodes are well-suited for electrochemical sensing (as will be shown in detail in the next section). For EIS analysis of bare LIG-NiO, see Appendix C for the corresponding figure and discussion.

Next, the LIG-NiO electrodes were functionalized with polyclonal anti-*Salmonella* antibodies via EDC/NHS covalent binding chemistry (see Materials and Methods and Figure 4.1) prior to subsequent *Salmonella* Typhimurium sensing. After functionalization, the obtained Nyquist plots were used to calculate the charge transfer resistance (R_{ct}) values (using the Randles equivalent circuit and calculated as the diameter of the semi-circular shaped portion of the plot). The R_{ct} was used to determine the optimum antibody concentration to be used in the experiments with bacteria. Figure 4.4d shows significant difference ($p < 0.05$) in percent R_{ct} change ($\Delta R_{ct,}$ %) among the antibody loading concentrations tested (75, 150, and 225 µg/mL). Probably, the 225 µg/mL concentration was too high, causing the antibody to dissociate from the surface of electrode resulting in negative ΔR_{ct} and inconsistent impedance readings during the bacteria testing (data not shown). The concentration of 75 and 150 µg/mL of antibody produced the positive ΔR_{ct} ($p < 0.05$) percent R_{ct} change and therefore, were selected for further experiments with *Salmonella* Typhimurium.

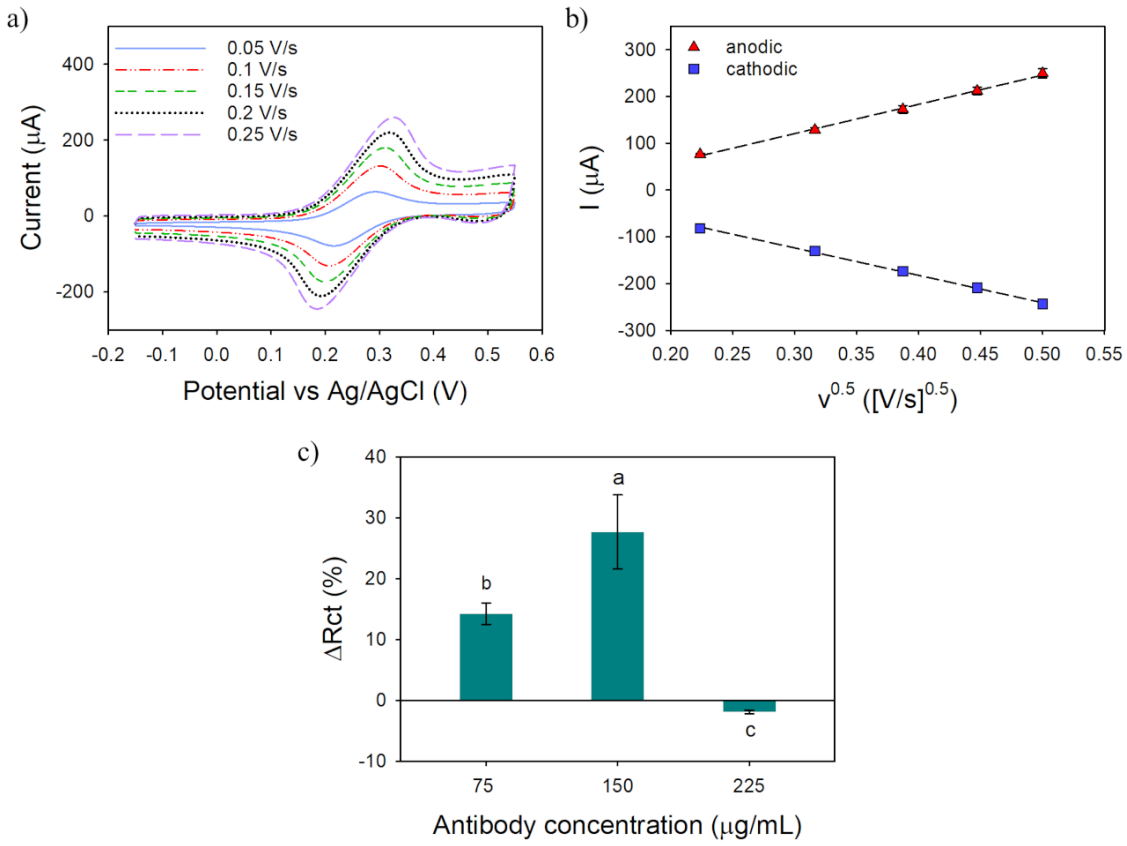

Figure 4.4 a) Representative cyclic voltammogram of the LIG-NiO electrode vs Ag/AgCl in 0.1 M KCl containing 4 mM $K_3[Fe(CN)_6]/K_4[Fe(CN)_6]$ at scan rates from 0.05 to 0.25 V s^{-1}; b) Cottrell plot of the LIG-NiO electrode vs Ag/AgCl generated from graph a) corresponding values of ESA = 0.22 ± 0.01 cm^2; and c) optimization of antibody concentration showing that 75 µg/mL and 150 µg/mL of anti-*Salmonella* antibody produced positive ($p < 0.05$) percent R_{ct} change and were selected for further experiments. Error bars represent the standard deviation of the arithmetic mean; letters denote significantly different means ($p < 0.05$).

4.3.3. Biosensor performance testing in buffer

Based on the principle that binding of target bacteria to the biofunctionalized region of the electrode decreases the electron transfer at the electrode, which can be measured as an increase of charge transfer resistance (R_{ct}) (Mutreja et al., 2016), EIS analysis was performed to determine impedance differences caused by bacteria presence.

All tests included 15 min for bacteria capture and 2 min for the EIS measurement performed over a frequency range of 1 Hz to 100 kHz. The LIG-NiO electrodes functionalized with 75 µg/mL and 150 µg/mL of antibody were tested with increasing concentration of *Salmonella* Typhimurium (ranging from 10^0 to 10^6 CFU/mL), and the change in R_{ct} (with respect to the R_{ct} value measured for zero concentration of bacteria) was used to produce the calibration curves in pristine buffer, presence of interferent bacteria, and in complex media (i.e., chicken broth) as shown in Figures 4.5 to 4.7. During the capture step, the *Salmonella* bacteria bind to the antibody epitope, forming an insulating layer on the electrode surface. With more *Salmonella* bacteria binding to the antibodies on the electrode, the insulating layer increases, which limits the access of the electrolyte to the electrode surface, resulting in the proportional increase of R_{ct} (Mutreja et al., 2016).

Salmonella Typhimurium detection was first assessed in PBS at room temperature for LIG-NiO electrodes without antibody and functionalized with 75 µg/mL antibody. Figure 4.5a shows the bare LIG-NiO without antibody functionalization with little change in R_{ct} with increasing bacteria concentration, which is reflected in a flat line in Figure 4.5c and high LOD of 30.8 ± 3 CFU/mL. Functionalization of the LIG-NiO electrode with 75 µg/mL antibody (Figure 4.5b) resulted in the consistent increase of the R_{ct} values with increasing bacteria concentration up to 10^6 CFU/mL in addition to a lower ($p < 0.05$) LOD of 7.46 ± 0.62 CFU/mL (sensitivity of 2.10 ± 0.21 Ω/(log CFU/mL)). This could be expected as the purpose of antibody functionalization is to promote bacteria binding and improve performance of the sensor; however, opposed to

what was anticipated, the higher concentration of antibody loading of 150 μg/mL (Figures 4.6 a and b) presented no significant ($p > 0.05$) difference in LOD (6.52 ± 0.34 CFU/mL) and sensitivity (2.20 ± 0.75 Ω/(log CFU/mL)) compared to a 75 μg/mL loading over the same range of bacteria concentration (10^1 to 10^6 CFU/mL) in PBS. Nevertheless, the antibody concentration of 150 μg/mL was used on further selectivity and food sample experiments as more available active sites are expected to enhance bacteria binding when in the presence of interferents (i.e., other bacteria and food components).

Lower sensing ranges and higher limits of detection have been reported in the literature using other electrochemical devices that also require longer response times for detection of *S.* Typhimurium in buffer, including the study by Wen et al. (2017) that developed a portable impedance immunosensing system consisting of a gold interdigitated array microelectrode (IDAM) functionalized with antibodies, showing a higher LOD (10^3 CFU/mL), longer detection time (1 h), and a sensing range between 10^3 and 10^7 CFU/mL. Similar to this study, Dinshaw et al. (2017) reported an LOD of 10 CFU/mL using a reduced graphene-chitosan sensor functionalized with *S.* Typhimurium-specific aptamers with a sensing range between 10 and 10^7 CFU/mL in PBS when applying differential pulse voltammetry to interrogate the sensors (no response time reported). Ma et al. (2014) demonstrated an impedimetric sensor with an LOD of 3 CFU/mL in physiological saline using a glassy carbon electrode modified with graphene oxide, gold nanoparticles, and functionalized with a *Salmonella*-specific aptamer; however, the response time was longer (35 min), and the sensing range was limited (3 to

10^3 CFU/mL). In contrast, the sensing range presented by the LIG-NiO immunosensor in PBS confirmed its capacity for efficient detection of *S.* Typhimurium that is comparable to the plate counting standard method (~ 5 CFU/mL) (N et al., 2016) with an overall response time of 17 min (including incubation of electrode with the sample).

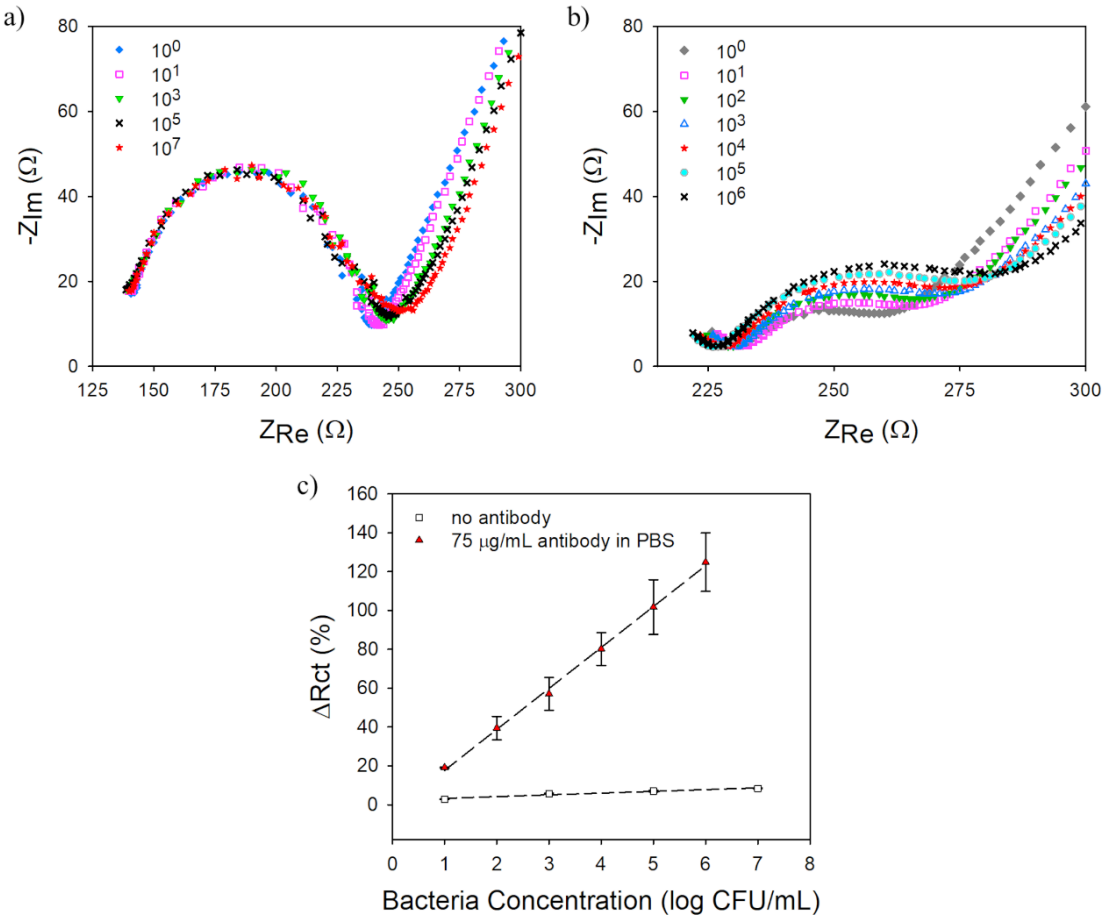

Figure 4.5 Representative Nyquist plots of impedance spectra of the LIG-NiO sensor functionalized with a) no antibody; and b) with 75 µg/mL anti-*Salmonella* antibody exposed to increasing concentration (CFU/mL) of *Salmonella* Typhimurium in PBS. c) Linear calibration curves of charge transfer resistance change (ΔR_{ct}) vs bacteria concentrations (log CFU/mL) generated from graphs (a, b); data represents the average of three repetitions and error bars represent the standard deviation. Note: standard deviation values under 0.3 CFU/mL are not visible in graph c due to scale.

The selectivity test was performed with *E. coli* spp. as an interferent bacterium due to its similarity to *Salmonella* spp. as Gram-negative bacteria and to both being known foodborne pathogens. The tests with 150 µg/mL anti-*Salmonella* antibody for *S.* Typhimurium alone and in the presence of *E. coli* (Figures 4.6 c and d) presented similar performances ($p > 0.05$) with a linear sensing range from 10^1 to 10^6 CFU/mL and sensitivities of 2.20 ± 0.75 Ω/(log CFU/mL) for the *S.* Typhimurium alone and 1.98 ± 0.25 Ω/(log CFU/mL) for *S.* Typhimurium in the presence of *E. coli* spp. With the addition of equal concentrations of *E. coli* in the testing solution, the LOD decreased ($p < 0.05$) to 4.48 ± 1.21 CFU/mL indicating no cross-reaction between the sensor and *E. coli* spp., which demonstrates the high specificity of the anti-*Salmonella* antibody and consequently the immunosensor to the targeted pathogen, *S.* Typhimurium, over a broad concentration that is range relevant to food safety. In the next section, the LIG-NiO sensors are challenged against *S.* Typhimurium in food samples.

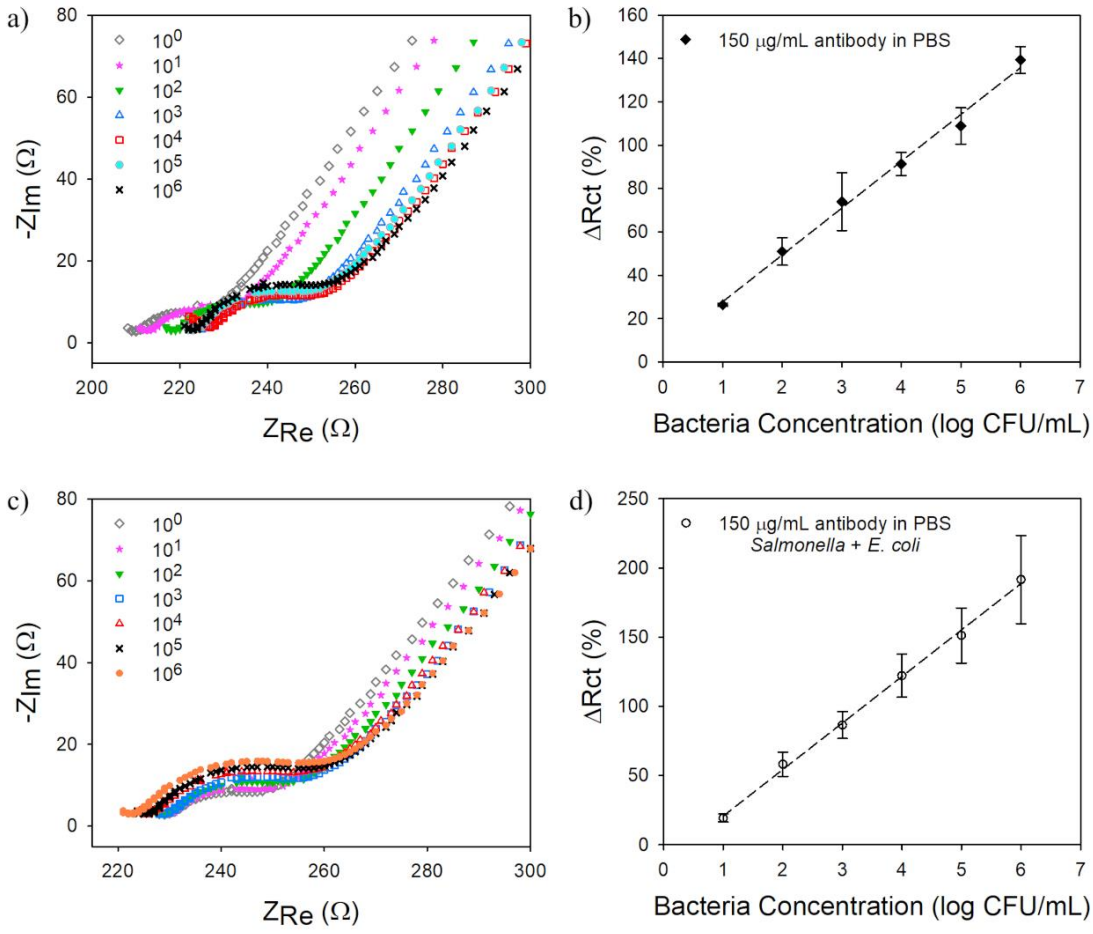

Figure 4.6 Representative Nyquist plots of impedance spectra of the LIG-NiO immunosensor functionalized with 150 µg/mL of anti-*Salmonella* antibody exposed to a) increasing concentration *(CFU/mL)* of *Salmonella* Typhimurium*;* and c) equal concentrations of *E. coli* and *Salmonella* Typhimurium (CFU/mL) in PBS, respectively. The corresponding linear calibration curves of charge transfer resistance change ($\Delta R_{ct,}$) vs. *S.* Typhimurium concentrations (log CFU/mL) for LIG-NiO immunosensor exposed to b) *S.* Typhimurium and d) *S.* Typhimurium and *E. coli* spp.; data represents the average of three repetitions and error bars represent the standard deviation.

4.3.4. Biosensor performance testing in food samples

Next, the LIG-NiO immunosensor was evaluated in a real food sample (i.e., chicken broth). The increase in *Salmonella* Typhimurium in spiked chicken broth resulted in an increase in R_{ct}, as observed from the Nyquist plot in Figure 4.7a and the calibration plot in Figure 4.7b. Based on the calibration curve, the linear sensing range for *S.* Typhimurium in chicken broth is 10^1 to 10^5 CFU/mL ($R^2 = 0.983$), which is narrower than the previous tests in PBS, with a linear range from 10^1 to 10^6 CFU/mL, and $R^2 = 0.993$ and $R^2 = 0.998$ for *S.* Typhimurium alone and in the presence of *E. coli*, respectively. Nevertheless, the range is still relevant to food safety. Testing the sensor in a food product can also determine its selectivity to the target bacteria as well as if the sensitivity may be affected by the interference of food components, such as carbohydrates and proteins, among other components in the chicken broth, that could interact with the biosensor through non-specific adsorption resulting in a false-positive signal. The LIG-NiO immunosensor sensitivity in chicken broth was 2.04 ± 0.54 Ω/(log CFU/mL) and was comparable ($p > 0.05$) to the sensitivity observed in buffer. In addition, the limit of detection of 1.28 ± 0.21 CFU/mL was obtained for chicken broth samples, which is lower ($p < 0.05$) than the detection limit observed in buffer. These results demonstrate the versatility and stability of the LIG-NiO biosensor even when used in complex samples such as chicken broth.

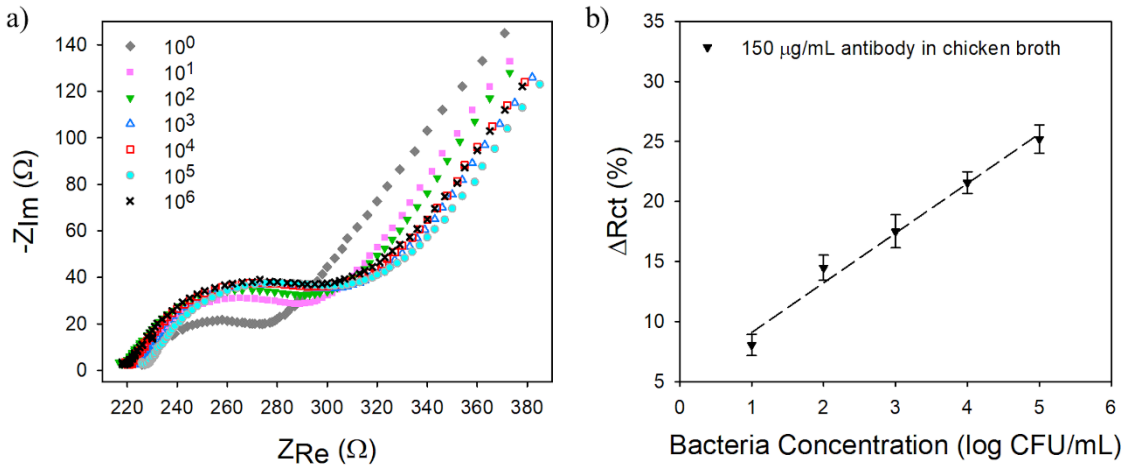

Figure 4.7 a) Representative Nyquist plot of impedance spectra of the LIG-NiO immunosensor functionalized with 150 µg/mL of anti-*Salmonella* antibody exposed to increasing concentration (CFU/mL) of *Salmonella* Typhimurium in chicken broth. b) The corresponding linear calibration curve of charge transfer resistance change (ΔR_{ct}) vs. bacteria concentrations (log CFU/mL) in chicken broth for the LIG-NiO immunosensor; data represents the average of three repetitions and error bars represent the standard deviation.

The detection limit and response time for the LIG-NiO immunosensor were lower than or similar to all biosensors shown in Table 4.1 for detection of *Salmonella* Typhimurium. For instance, one of the best performances was from the graphene-graphene oxide (G-GO) screen printed carbon electrode (SPE) immunosensor developed by Mutreja et al. (2016) that was able to specifically detect *S.* Typhimurium in spiked water and juice samples with a detection limit of ~10 CFU/mL in approximately 12 min using a specific biomarker, OmpD, although with a longer sensor fabrication process. Appaturi et al. (2020) also reported an excellent LOD and analysis time (10^1 CFU/mL and 10 min, respectively) with a reduced graphene oxide-carbon nanotubes (rGO-CNT) aptasensor, however, with a substantially more complex and longer fabrication process than reported in this work. Zhu et al. (2014) reported a low LOD of 6 CFU/mL for *S.*

Typhimurium in milk samples with an electrochemical sensing strategy that combined the rolling circle amplification and DNA functionalized gold nanoparticles, however, with a particularly complicated sensor fabrication process and total analysis time of over 90 min. Soares et al. (2020) reported a label-free LIG-based biosensor functionalized with *Salmonella* specific antibodies that detected *S.* Typhimurium in chicken broth across a similar range of detection (25 to 10^5 CFU/mL) and with a slightly higher detection limit (13 ± 7 CFU/mL). The addition of NiO on the present work significantly improved electron transfer (see Section 3.2) and, consequently, the sensor performance metrics for bacteria detection compared to Soares et al. (2020). The performance of the biosensor developed here indicates that this sensor has potential to be used in other food samples that are suspended in water or diluted with the advantages of not requiring bacteria purification or concentration steps or labeling steps, short response time (17 min), small physical working area (0.071 cm^2) for portability, and, most importantly, relatively simple fabrication that allows mass production. The excellent performance of the sensor was attributed to the 3D porous graphene and nickel oxide nanoparticle composite that enhanced electron transport and stability for improved signal transduction along with a biorecognition agent such as bacteria-specific antibodies that added another layer of engineered performance.

Table 4.1 Biosensor performance comparison to other devices in the literature for *Salmonella* Typhimurium detection.

Platform and biorecognition agent	**Detection mode**	**Test medium**	**Detection range* (CFU/mL)**	**Response time (min)**	**Reference**
LIG-NiO + antibody	Impedimetric	PBS	6.5 - 10^6	17	This work
LIG-NiO + antibody	Impedimetric	PBS + *E. coli*	4.6 - 10^6	17	This work
LIG-NiO + antibody	Impedimetric	Chicken broth	1.3 - 10^5	17	This work
rGO-CHI + aptamer	DPV	PBS	10 - 10^7	Not reported	(Dinshaw et al., 2017)
Gold IDAM + antibody	Impedimetric	PBS	10^3 - 10^7	60	(Wen et al., 2017)
rG-GO/SPE + antibody	Impedimetric	Orange juice	10.7 - 10^5	~12	(Mutreja et al., 2016)
LIG + antibody	Impedimetric	Chicken broth	13 - 10^5	22	(Soares et al., 2020)
GCE/GO/GNP + aptamer	Impedimetric	Physiological saline	3 - 10^3	35	(Ma et al., 2014)
RCA + DNA-AuNP	Amperometric	Milk	6 - 10^5	> 90	(Zhu et al., 2014)

Table 4.1 Continued

Platform and biorecognition agent	Detection mode	Test medium	Detection range* (CFU/mL)	Response time (min)	Reference
rGO-CNT + aptamer	DPV	Chicken in BPW	10 - 10^8	10	(Appaturi et al., 2020)

* Lowest value corresponds to the lower limit of detection (LOD)
rGO-CHI: reduced graphene oxide-chitosan; DPV: differential pulse voltammetry; IDAM: interdigitated array microelectrode; rG-GO/SPE: reduced graphene-graphene oxide embedded on screen printed carbon electrodes; GCE/GO/GNP: glassy carbon electrode modified with graphene oxide and gold nanoparticles; RCA + DNA-AuNP: rolling circle amplification + DNA functionalized gold nanoparticles; rGO-CNT: reduced graphene oxide-carbon nanotubes.

4.4. Conclusions

In this study, a LIG-NiO immunosensor for *S.* Typhimurium detection was developed. LIG-NiO was fabricated under ambient conditions by a low-cost, two-step writing fabrication process using polyimide and nickel acetate solution as substrates. The fabrication procedure is easily scalable for mass production of electrochemical sensors, eliminating the need for further modification or treatments with nanomaterials, such as electrodeposition or sputtering process as previously reported for printed electrodes (Simoska & Stevenson, 2019; Vu et al., 2021; Xuan et al., 2018; Yuhan Zhang et al., 2019), since the solution phase deposition of the NiO precursor can be integrated into roll-to-roll processing. Characterization of the LIG-NiO showed the presence of 3D porous graphene and nickel oxide nanoparticle structures (Kucherenko et al., 2021; Soares et al., 2020) with high electrical conductivity and electroactive surface area (ESA

= 0.22 ± 0.01 cm^2, 3-fold larger than the working electrode geometric area) that were conducive to electrochemical sensing. Building on these results, LIG-NiO electrodes were functionalized with polyclonal anti-*Salmonella* antibody via EDC/NHS chemistry. *S.* Typhimurium was tested in buffer and in chicken broth to validate sensor performance. The LIG-NiO immunosensor platform could detect *S.* Typhimurium in PBS and chicken broth over relevant levels for food safety analysis of 10^1 to 10^6 CFU/mL and 10^1 to 10^5 CFU/mL, respectively. The immunosensors also showed a rapid response time of only 17 min without the need for pre-labeling nor pre-treatment of the tested chicken broth sample. Additionally, the immunosensor sensitivity was not significantly influenced by the presence of interferent bacteria, *E. coli* spp., nor by the presence of other food components found in chicken broth. Other sensors in literature may have comparable response times and sensing ranges; however, the sensor developed here has advantages such as simple and scalable fabrication under ambient conditions, no labeling, and no bacteria concentration required being among the most efficient platform for *S.* Typhimurium sensing to date, with limits of detection of 6.52 ± 0.34 CFU/mL and 1.28 ± 0.21 CFU/mL in PBS and chicken broth, respectively. The LIG-NiO platform developed here can likely be used in other biosensing applications where rapid monitoring of target compounds is desired using the developed sensing protocol. More specifically, these results demonstrate the potential applicability of LIG-NiO sensing platform as it could be customized with other biorecognition agents for real-time and in-field monitoring of different pathogens, which reinforces its important contribution to food safety.

CHAPTER V CONCLUSIONS AND RECOMMENDATIONS FOR FUTURE WORK

5.1. Conclusions

Current commercially available detection methods for foodborne pathogens in food samples are still laborious and time consuming. As foodborne pathogens are a constant concern in the food industry for purposes of food safety, public health, food quality, and economic losses due to disease outbreaks and recalls of contaminated food, there is an urgent need for a rapid, reliable, and cost-effective detection method. In this study, three different impedance biosensor platforms were developed and tested for the real-time detection of bacteria pathogens in a buffer solution (PBS), with another interferent bacterium, as well as in a real-world scenario simulated by a food matrix, chicken broth. Each sensor tested had a detection time of approximately 17 minutes, including the time that the sensors were allowed to sit in the bacteria suspension (15 minutes) and how long it took to run an EIS test (approximately 2 minutes). *Listeria monocytogenes* and *Salmonella* Typhimurium were chosen as target bacteria due to their importance in food safety. All the developed biosensors had a wide detection range of at least 10^1-10^5 CFU/mL of bacteria (*Listeria* and *Salmonella*, depending on the platform used) which covers the relevant levels for food safety analysis enabling food manufacturers to reduce economic and public health implications due to recalls of contaminated food or the extra time to release the product, and consequently contributing to food safety.

For the detection of *Listeria monocytogenes* two sensors were fabricated using a simple one-step sonoelectrodeposition method to create hybrid composites of platinum and pH-responsive polymers, alginate modified with cysteine and chitosan, combined with aptamers as biorecognition agents. The deposition conditions and the loading of the biorecognition agent were optimized to create stimuli-responsive nanobrushes with platinum nanoparticles and aptamers, which showed to enhance the capture of target *L. monocytogenes* bacteria and sensors performance. The best pH conditions for testing were identified through actuation tests based on pH changes for extension and contraction of the polymer brushes. The actuation protocol consisted of capture bacteria when both polymers nanobrushes were expanded (4 and 7 for chitosan and alginate, respectively), and signal acquisition when the brushes were collapsed (8 and 3 for chitosan and alginate, respectively), which demonstrated to be very efficient to capture bacteria. Expanded brushes exposed the biorecognition agent, while collapsed brushes assisted in electrochemical signal transduction. The developed biosensors were tested in three different media and had a wide detection range of at least 10^1-10^5 CFU/mL of *L. monocytogenes* which covers the relevant levels for food safety monitoring. The limits of detection (LOD) for *L. monocytogenes* in the food sample, chicken broth, were 3.3 CFU/mL and 4.4 CFU/mL for the CHI/Pt-aptamer and ALG-thiomer/Pt-aptamer sensors, respectively. The results demonstrated that the incorporation of aptamers, pH-responsive polymers and nanoplatinum resulted in highly sensitive, selective, rapid and label-free electrochemical biosensors that can be used for real-time detection of *L. monocytogenes*.

For the detection of *Salmonella* Typhimurium, a sensing platform based on laser-induced graphene with nickel oxide nanoparticles (LIG-NiO) functionalized with *Salmonella*-specific antibodies was developed. This platform is easily fabricated by a two-step process using polyimide film and nickel acetate solution as substrates. Characterization of the LIG-NiO platform showed the presence of 3D porous graphene and nickel oxide composite structures with high electrical conductivity and surface area that were conducive to electrochemical sensing. The LIG-NiO sensor was able to detect *S.* Typhimurium in chicken broth in a wide detection range of 10^1-10^5 CFU/mL with a limit of detection of 1.3 CFU/mL, demonstrating the potential applicability of the LIG-NiO sensing platform in food safety monitoring.

All the sensors developed in this study are among the most efficient compared to the best sensors reported in the literature in terms of limit of detection and detection time in real food samples. However, the sensors studied here have several advantages: 1) easy fabrication; 2) no labeling necessary; 3) no bacteria concentration required; and 4) one of the fastest response times with total response time of 17 minutes including sample exposure and testing. Although further validation studies with other food products and interferents are still necessary to replace the current methods with these sensing platforms. This research also has unforeseen broad applications in areas other than food, including biomedical, public health and environmental, such as hospital infection and water quality monitoring, disease tracking in ecosystems, food allergen detection, among others. It is fully expected that this technology and the platforms studied could be applied to other foodborne pathogens, such as e.g., *E. coli* and *S. aureus*, as the

application of other biorecognition agents in a similar manner can be used to detect other specific pathogens. With the data obtained and a better understanding of the sensing methods developed, it is possible that in the future a biosensor could detect multiple pathogens that are mostly prevalent in food products and be able to differentiate exactly the pathogen present by functionalizing the sensor with multiple biorecognition agents specific to each pathogen.

5.2. Recommendations for future work

Recommendations for future research on real-time detection of bacteria using biosensors functionalized with biorecognition agents include:

- Explore the use of other biorecognition agents and other bacteria using the same platforms studied here.
- Determine sensor performance with various food products and interferents, different sample types and sizes, and distinct collection techniques such as swab, broth, and slurry to validate sensor performance in various sample media and the effect they have on bacteria capture and sensitivity.
- Design experiments to evaluate sensor shelf-life and optimize storage conditions for best sensor performance and cost efficiency.
- Test sensor reusability and the effect of different washing techniques for bacteria removal post detection on sensor performance and reliability related to the sensor platform integrity after washing steps on subsequent bacteria capture and detection.

- Explore the attachment of multiple capture probes on one sensor surface to create a multiplex sensor capable of detecting and differentiating among different bacteria present.
- Test the performance of the biosensors in the presence of non-viable cells to understand the effect caused on sensor performance.
- Test the combination with other biological components such as enzymes to determine viability of cells.

REFERENCES

Abdelhamid, H. N., & Wu, H. (2013a). Multifunctional graphene magnetic nanosheet decorated with chitosan for highly sensitive detection of pathogenic bacteria. *Journal of Materials Chemistry B*, 3950–3961. https://doi.org/10.1039/c3tb20413h

Abdelhamid, H. N., & Wu, H. (2013b). Probing the interactions of chitosan capped CdS quantum dots with pathogenic bacteria and their biosensing application. *Journal of Materials Chemistry B*, 6094–6106. https://doi.org/10.1039/c3tb21020k

Acquah, C., Agyei, D., Monney, I., Pan, S., & Danquah, M. (2018). Aptameric Sensing in Food Safety. In Food Control and Biosecurity. In H. & Grumezescu (Ed.), *Handbook of Food Bioengineering (Vol. 16)* (pp. 259–277). Elsevier.

Acquah, C., Danquah, M. K., Agyei, D., Moy, C. K. S., Sidhu, A., Ongkudon, C. M., … Ongkudon, C. M. (2016). Deploying aptameric sensing technology for rapid pandemic monitoring Deploying aptameric sensing technology for rapid pandemic monitoring. *Critical Reviews in Biotechnology*, *36*(6), 1010–1022. https://doi.org/10.3109/07388551.2015.1083940

Adeloju, S. B., & Hussain, S. (2016). Potentiometric sulfite biosensor based on entrapment of sulfite oxidase in a polypyrrole film on a platinum electrode modified with platinum nanoparticles. *Microchimica Acta*, *183*(4), 1341–1350. https://doi.org/10.1007/s00604-016-1748-0

Akhtar, M. A., Ilyas, K., Dlouh, I., Siska, F., & Boccaccini, A. R. (2020). Electrophoretic Deposition of Copper (II)– Chitosan Complexes for Antibacterial Coatings. *International Journal of Molecular Sciences*, *21*, 2637.

Ali, M. H., Elsherbiny, M. E., & Emara, M. (2019). Updates on Aptamer Research. *International Journal of Molecular Sciences*, *20*, 2511.

Alocilja, E. C., & Radke, S. M. (2003). Market analysis of biosensors for food safety. *Biosensors and Bioelectronics*, *18*(5–6), 841–846. https://doi.org/10.1016/S0956-5663(03)00009-5

Amini, M., Hisdal, J., & Kalvøy, H. (2018). Applications of bioimpedance measurement techniques in tissue engineering. *Journal of Electrical Bioimpedance*, *9*, 142–158.

Appaturi, J. N., Pulingam, T., Thong, K. L., Muniandy, S., Ahmad, N., & Leo, B. F. (2020). Rapid and sensitive detection of Salmonella with reduced graphene oxide-carbon nanotube based electrochemical aptasensor. *Analytical Biochemistry*, *589*, 113489.

Arora, P., Sindhu, A., Dilbaghi, N., & Chaudhury, A. (2011). Biosensors as innovative tools for the detection of food borne pathogens. *Biosensors and Bioelectronics*, *28*(1), 1–12. https://doi.org/10.1016/j.bios.2011.06.002

Arora, P., Sindhu, A., Kaur, H., Dilbaghi, N., & Chaudhury, A. (2013). An overview of transducers as platform for the rapid detection of foodborne pathogens. *Applied Microbiology and Biotechnology*, *97*, 1829–1840. https://doi.org/10.1007/s00253-013-4692-5

Augst, A. D., Kong, H. J., & Mooney, D. J. (2006). Alginate hydrogels as biomaterials. *Macromolecular Bioscience*, *6*(8), 623–633. https://doi.org/10.1002/mabi.200600069

Baio, J. E., Weidner, T., Brison, J., Graham, D. J., Gamble, L. J., & Castner, D. G.

(2009). Amine Terminated SAMs: Investigating Why Oxygen is Present in these Films. *J Electron Spectros Relat Phenomena*, *172*, 2–8. https://doi.org/10.1016/j.elspec.2009.02.008.Amine

Balamurugan, S., Obubuafo, A., Soper, S. A., & Spivak, D. A. (2008a). Surface immobilization methods for aptamer diagnostic applications. *Analytical and Bioanalytical Chemistry*, *390*(4), 1009–1021. https://doi.org/10.1007/s00216-007-1587-2

Balamurugan, S., Obubuafo, A., Soper, S. A., & Spivak, D. A. (2008b). Surface immobilization methods for aptamer diagnostic applications. *Analytical and Bioanalytical Chemistry*, *390*(4), 1009–1021. https://doi.org/10.1007/s00216-007-1587-2

Baraket, A., Lee, M., Zine, N., Sigaud, M., Bausells, J., & Errachid, A. (2017). A fully integrated electrochemical biosensor platform fabrication process for cytokines detection. *Biosensors and Bioelectronics*, *93*, 170–175.

Berger, J., Reist, M., Mayer, J. M., Felt, O., Peppas, N. A., & Gurny, R. (2004). Structure and interactions in covalently and ionically crosslinked chitosan hydrogels for biomedical applications. *European Journal of Pharmaceutics and Biopharmaceutics*, *57*(1), 19–34. https://doi.org/10.1016/S0939-6411(03)00161-9

Berney, H. (2004). Capacitance Affinity Biosensors. In *Ultrathin Electrochemical Chemo- and Biosensors*. Springer Berlin Heidelberg.

Bianchi, C. L., Cattania, M. G., & Villa, P. (1993). XPS characterization of Ni and MO oxides before and after “in situ” treatments. *Applied Surface Science*, *70/71*, 211–

216.

Bintsis, T. (2017). Foodborne pathogens. *AIMS Microbiology*, *3*(3), 529–563. https://doi.org/10.3934/microbiol.2017.3.529

Bockrath, M., Markovic, N., Shepard, A., Tinkham, M., Gurevich, L., Kouwenhoven, L. P., … Sohn, L. L. (2002). Scanned Conductance Microscopy of Carbon Nanotubes and λ -DNA. *Nano Letters*, *2*(3), 187–190.

Briandet, R., Meylheuc, T., Maher, C., & Bellon-Fontaine, M. N. (1999). Listeria monocytogenes Scott A: Cell Surface Charge, Hydrophobicity, and Electron Donor and Acceptor Characteristics under Different Environmental Growth Conditions. *Applied and Environmental Microbiology*, *65*(12), 5328–5333.

Burrs, S. L., Vanegas, D. C., Bhargava, M., Mechulan, N., Hendershot, P., Yamaguchi, H., … Mclamore, E. S. (2015). A comparative study of graphene–hydrogel hybrid bionanocomposites for biosensing. *Analyst*, *140*, 1466–1476. https://doi.org/10.1039/c4an01788a

Cardoso, A. R., Marques, A. C., Santos, L., Carvalho, A. F., Costa, F. M., Martins, R., … Fortunato, E. (2019). Molecularly-imprinted chloramphenicol sensor with laser-induced graphene electrodes. *Biosensors and Bioelectronics*, *124–125*, 167–175. https://doi.org/https://doi.org/10.1016/j.bios.2018.10.015

Carriedo, G. a. (1988). The use of cyclic voltammetry in the study of the chemistry of metal-carbonyls: An introductory experiment. *Journal of Chemical Education*, *65*(11), 1020. https://doi.org/10.1021/ed065p1020

Castell-Perez, E., Gomes, C., Tahtouh, J., Moreira, R., Mclamore, E. S., & Knowles III,

H. S. (2017). Food Processing and Waste Within the Nexus Framework. *Current Sustainable/Renewable Energy Reports*, *4*, 99–108. https://doi.org/10.1007/s40518-017-0079-z

Castner, D. G., Hinds, K., & Grainger, D. W. (1996). X-ray Photoelectron Spectroscopy Sulfur 2p Study of Organic Thiol and Disulfide Binding Interactions with Gold Surfaces, *7463*(26), 5083–5086.

CDC. (2018). Burden of Foodborne Illness: Findings. Retrieved April 3, 2021, from https://www.cdc.gov/foodborneburden/2011-foodborne-estimates.html

CDC. (2019). *Surveillance for Foodborne Disease Outbreaks United States, 2017: Annual Report*. Retrieved from https://www.cdc.gov/fdoss/pdf/2017_FoodBorneOutbreaks_508.pdf

CDC. (2021a). Listeria Outbreaks. Retrieved November 7, 2021, from https://www.cdc.gov/listeria/outbreaks/index.html

CDC. (2021b). Salmonella. Retrieved from https://www.cdc.gov/salmonella/index.html

Chen, X., Yan, H., Sun, W., Shi, Z., & Zhang, W. (2019). Electrodeposition of alginate – MnO 2 – C composite film on the carbon ionic liquid electrode for the direct electrochemistry and electrocatalysis of myoglobin. *Polymer Bulletin*, *76*(8), 3971–3987. https://doi.org/10.1007/s00289-018-2589-2

Chen, Y., Xiang, J., Liu, B., & Chen, Z. (2020). Gold nanoparticle-engineered electrochemical aptamer biosensor for ultrasensitive detection of thrombin. *Analytical Methods*, *12*, 3729. https://doi.org/10.1039/d0ay01163k

Cheng, Y., Luo, X., Betz, J., Buckhout-White, S., Bekdash, O., Payne, G. F., … Rubloff,

G. W. (2010). In situ quantitative visualization and characterization of chitosan electrodeposition with paired sidewall electrodes. *Soft Matter*, *6*, 3177–3183. https://doi.org/10.1039/c0sm00124d

Cheng, Y., Luo, X., Betz, J., Payne, G. F., Bentley, E., & Rubloff, G. W. (2011). Mechanism of anodic electrodeposition of calcium alginate. *Soft Matter*, *7*, 5677–5684. https://doi.org/10.1039/c1sm05210a

Cheong, M., & Zhitomirsky, I. (2008). Electrodeposition of alginic acid and composite films. *Colloids and Surfaces A : Physicochemical and Engineering Aspects*, *328*, 73–78. https://doi.org/10.1016/j.colsurfa.2008.06.019

Chu, L., Li, M., Wang, Y., Li, X., Wan, Z., Dou, S., & Chu, Y. (2016). Multishelled NiO Hollow Spheres Decorated by Graphene Nanosheets as Anodes for Lithium-Ion Batteries with Improved Reversible Capacity and Cycling Stability. *Journal of Nanomaterials*, 4901847. https://doi.org/s http://dx.doi.org/10.1155/2016/4901847

Cinti, S., Volpe, G., Piermarini, S., Delibato, E., & Palleschi, G. (2017). Electrochemical Biosensors for Rapid Detection of Foodborne Salmonella: A Critical Overview. *Sensors*, *17*(8), 1910. https://doi.org/10.3390/s17081910

Claussen, J. C., Kumar, A., Jaroch, D. B., Khawaja, M. H., Hibbard, A. B., Porterfield, D. M., & Fisher, T. S. (2012). Nanostructuring platinum nanoparticles on multilayered graphene petal nanosheets for electrochemical biosensing. *Advanced Functional Materials*, *22*(16), 3399–3405. https://doi.org/10.1002/adfm.201200551

Cooper, D. R., D'Anjou, B., Ghattamaneni, N., Harack, B., Hilke, M., Horth, A., … Yu, V. (2012). Experimental Review of Graphene. *ISRN Condensed Matter Physics*,

501686. https://doi.org/10.5402/2012/501686

Das, S. R., Nian, Q., Cargill, A. A., Hondred, J. A., Ding, S., Saei, M., … Claussen, J. C. (2016). 3D nanostructured inkjet printed graphene via UV-pulsed laser irradiation enables paper-based electronics and electrochemical devices. *Nanoscale*, *8*, 15870. https://doi.org/10.1039/c6nr04310k

Dean, D. A., Ramanathan, T., Machado, D., & Sundararajan, R. (2008). Electrical Impedance Spectroscopy Study of Biological Tissues. *Journal of Electrostatics*, *66*, 165–177. https://doi.org/10.1016/j.elstat.2007.11.005.Electrical

Dewey-Mattia, D., Manikonda, K., Hall, A. J., Wise, M. E., & Crowe, S. J. (2018). *Surveillance for Foodborne Disease Outbreaks - United States, 2009 - 2015. CDC (Centers for Disease Control and Prevention), MMWR Surveillance Summaries; 67(No. SS-10):1–11. DOI: http://dx.doi.org/10.15585/mmwr.ss6710a1* (Vol. 67). https://doi.org/http://dx.doi.org/10.15585/mmwr.ss6710a1

Dhillon, S., & Kant, R. (2017). Theory for electrochemical impedance spectroscopy of heterogeneous electrode with distributed capacitance and charge. *Journal of Chemical Sciences*, *129*(8), 1277–1292. https://doi.org/10.1007/s12039-017-1335-x

Dinshaw, I. J., Muniandy, S., Teh, S. J., Ibrahim, F., Leo, B. F., & Thong, K. L. (2017). Development of an aptasensor using reduced graphene oxide chitosan complex to detect Salmonella. *Journal of Electroanalytical Chemistry*, *806*, 88–96.

Duncan, T. V. (2011). Applications of nanotechnology in food packaging and food safety: Barrier materials, antimicrobials and sensors. *Journal of Colloid and Interface Science*, *363*(1), 1–24. https://doi.org/10.1016/j.jcis.2011.07.017

Elgadir, M. A., Uddin, S., Ferdosh, S., Adam, A., Chowdhury, A. J. K., & Sarker, Z. I. (2015). Impact of chitosan composites and chitosan nanoparticle composites on various drug delivery systems : A review. *Journal of Food and Drug Analysis*, *23*, 619–629. https://doi.org/10.1016/j.jfda.2014.10.008

Elgrishi, N., Rountree, K. J., Mccarthy, B. D., Rountree, E. S., Eisenhart, T. T., & Dempsey, J. L. (2018). A Practical Beginner's Guide to Cyclic Voltammetry. *Journal of Chemical Education*, *95*, 197–206. https://doi.org/10.1021/acs.jchemed.7b00361

Elieh-Ali-Komi, D., & Hamblin, M. R. (2016). Chitin and Chitosan: Production and Application of Versatile Biomedical Nanomaterials. *International Journal of Advanced Research*, *4*(3), 411–427.

FDA. (2012). *US Food and Drug Administration: Bad Bug Book, Foodborne Pathogenic Microorganisms and Natural Toxins* (Second edi). https://doi.org/10.1016/S1872-2040(10)60451-3

FDA. (2018). US Food and Drug Administration: Food Safety Modernization Act (FSMA). Retrieved February 5, 2018, from https://www.fda.gov/Food/GuidanceRegulation/FSMA/

FDA. (2021). US Food and Drug Administration: Recalls, Market Withdrawals, & Safety Alerts. Retrieved February 10, 2021, from https://www.fda.gov/safety/recalls-market-withdrawals-safety-alerts

Fenzl, C., Nayak, P., Hirsch, T., Wolfbeis, O. S., Alshareef, H. N., & Baeumner, A. J. (2017). Laser-Scribed Graphene Electrodes for Aptamer-Based Biosensing. *ACS*

Sensors, *2*, 616–620. https://doi.org/10.1021/acssensors.7b00066

Fernandes, R., Wu, L., Chen, T., Yi, H., Rubloff, G. W., Ghodssi, R., … Payne, G. F. (2003). Electrochemically Induced Deposition of a Polysaccharide Hydrogel onto a Patterned Surface. *Langmuir*, *19*(10), 4058–4062.

Frye, D. M., Zweig, R., Sturgeon, J., Tormey, M., Lecavalier, M., Lee, I., … Mascola, L. (2002). An Outbreak of Febrile Gastroenteritis Associated with Delicatessen Meat Contaminated with Listeria monocytogenes, *90005*, 943–949.

Gaillard, J., Berche, P., & Frehei, C. (1991). Entry of L. monocytogenes into cells is mediated by Internalin, a repeat protein reminiscent of surface antigens from Gram-Positive Cocci. *Cell*, *65*(7), 1127–1141.

Garland, N. T., Mclamore, E. S., Cavallaro, N. D., Mendivelso-perez, D., Smith, E. A., Jing, D., & Claussen, J. C. (2018). Flexible Laser-Induced Graphene for Nitrogen Sensing in Soil. *ACS Applied Materials and Interfaces*, *10*, 39124–39133. https://doi.org/10.1021/acsami.8b10991

Garrote, B. L., Santos, A., & Bueno, P. R. (2019). Perspectives on and Precautions for the Uses of Electric Spectroscopic Methods in Label-free Biosensing Applications. *ACS Sensors*, *4*, 2216–2227. other. https://doi.org/10.1021/acssensors.9b01177

Giacobassi, C. A., Oliveira, D. A., Pola, C. C., Xiang, D., Tang, Y., Palit, S., … Gomes, C. L. (2021). Sense–Analyze–Respond–Actuate (SARA) Paradigm: Proof of Concept System Spanning Nanoscale and Macroscale Actuation for Detection of Escherichia coli in Aqueous Media. *Actuators*, *10*(1), 2.

Gómez-Navarro, C., Moreno-Herrero, F., Pablo, P. J. de, Colchero, J., Gómez-Herrero,

J., & Baró, A. M. (2002). Contactless experiments on individual DNA molecules show no evidence for molecular wire behavior. *Proceedings of the National Academy of Sciences*, *99*(13), 8484–8487.

Grainger, S., & Blunt, J. (1998). *Engineering Coatings: Design and Application* (2nd ed.). Cambridge: Abington Publishing. Retrieved from https://books.google.com/books?id=Rj4t1JNxU10C&printsec=frontcover&source=gbs_ge_summary_r&cad=0#v=onepage&q&f=false

Grieshaber, D., Mackenzie, R., Vörös, J., & Reimhult, E. (2008). Electrochemical Biosensors -Sensor Principles and Architectures. *Sensors*, *8*(January), 1400–1458. https://doi.org/10.3390/s8031400

Gu, F., Amsden, B., & Neufeld, R. (2004). Sustained delivery of vascular endothelial growth factor with alginate beads. *Journal of Controlled Release*, *96*(3), 463–472. https://doi.org/10.1016/j.jconrel.2004.02.021

Guo, Y., Zhao, C., Liu, Y., Nie, H., Guo, X., Song, X., … Wang, J. (2020). A novel fluorescence method for the rapid and effective detection of Listeria monocytogenes. *Analyst*, *145*, 3857–3863. https://doi.org/10.1039/d0an00397b

Heo, E. J., Song, B. R., Park, H. J., Kim, Y. J., Moon, J. S., Wee, S. H., … Yoon, Y. (2014). Rapid detection of Listeria monocytogenes by real-time PCR in processed meat and dairy products. *Journal of Food Protection*, *77*(3), 453–458. https://doi.org/10.4315/0362-028X.JFP-13-318

Hills, K. D., Oliveira, D. A., Cavallaro, N. D., Gomes, C. L., & McLamore, E. S. (2018). Actuation of chitosan-aptamer nanobrush borders for pathogen sensing. *Analyst*,

143(7), 1650–1661. https://doi.org/10.1039/c7an02039b

Hitchins, A., Jinneman, K., & Chen, Y. (2017). Bacteriological Analytical Manual Chapter 10: Detection of Listeria monocytogenes in Foods and Environmental Samples , and Enumeration of Listeria monocytogenes in Foods. United States Food and Drug Administration. Retrieved from https://www.fda.gov/food/laboratory-methods-food/bam-chapter-10-detection-listeria-monocytogenes-foods-and-environmental-samples-and-enumeration

Hoffmann, S., Maculloch, B., & Batz, M. (2015). *Economic Burden of Major Foodborne Illnesses Acquired in the United States, EIB-140, U.S. Department of Agriculture, Economic Research Service*. Retrieved from https://www.ers.usda.gov/webdocs/publications/43984/52807_eib140.pdf?v=4823.4

Hrapovic, S., Liu, Y., Male, K. B., & Luong, J. H. T. (2004). Electrochemical Biosensing Platforms Using Platinum Nanoparticles and Carbon Nanotubes. *Analytical Chemistry*, *76*(4), 1083–1088. https://doi.org/10.1021/ac035143t

Hu, L., Zhang, Q., Li, X., & Serpe, M. J. (2019). Materials Horizons and actuation. *Materials Horizons*, *6*, 1774–1793. https://doi.org/10.1039/c9mh00490d

Huang, W., Ding, S., Chen, Y., Hao, W., Lai, X., & Peng, J. (2017). 3D NiO hollow sphere/reduced graphene oxide composite for high- performance glucose biosensor. *Scientific Reports*, *7*, 5220. https://doi.org/10.1038/s41598-017-05528-1

Huang, X., Xu, Z., Mao, Y., Ji, Y., Xu, H., Xiong, Y., & Li, Y. (2015). Gold nanoparticle-based dynamic light scattering immunoassay for ultrasensitive

detection of Listeria monocytogenes in lettuces. *Biosensors and Bioelectronics*, *66*(November), 184–190. https://doi.org/10.1016/j.bios.2014.11.016

Hwang, J., Pathak, P., Wang, X., Rodriguez, K. L., Cho, H. J., & Lee, W. H. (2019). A Novel Bismuth-Chitosan Nanocomposite Sensor for Simultaneous Detection of Pb (I), Cd (II) and Zn (II) in Wastewater. *Micromachines*, *10*, 511.

Jantra, J., Kanatharana, P., Asawatreratanakul, P., Hedstrom, M., Mattiasson, B., & Thavarungkul, P. (2011). Real-time label-free affinity biosensors for enumeration of total bacteria based on immobilized concanavalin A. *Journal of Environmental Science and Health - Part A Toxic/Hazardous Substances and Environmental Engineering*, *46*(13), 1450–1460. https://doi.org/10.1080/10934529.2011.609022

Jin, Z., McNicholas, T. P., Shih, C., Wang, Q. H., Paulus, G. L. C., Hilmer, A. J., … Strano, M. S. (2011). Click Chemistry on Solution-Dispersed Graphene and Monolayer CVD Graphene. *Chemistry of Materials*, *23*, 3362–3370.

Jindal, A. B., Wasnik, M. N., & Nair, H. A. (2010). Synthesis of Thiolated Alginate and Evaluation of Mucoadhesiveness, Cytotoxicity and Release Retardant Properties. *Indian Journal of Pharmaceutical Sciences*, *72*(6), 766–774. https://doi.org/10.4103/0250

Joung, C. K., Kim, H. N., Lim, M. C., Jeon, T. J., Kim, H. Y., & Kim, Y. R. (2013). A nanoporous membrane-based impedimetric immunosensor for label-free detection of pathogenic bacteria in whole milk. *Biosensors and Bioelectronics*, *44*(1), 210–215. https://doi.org/10.1016/j.bios.2013.01.024

Ju, H. K., Kim, S. Y., & Lee, Y. M. (2001). pH/temperature-responsive behaviors of

semi-IPN and comb-type graft hydrogels composed of alginate and poly(N-isopropylacrylamide). *Polymer*, *42*(16), 6851–6857. https://doi.org/10.1016/S0032-3861(01)00143-4

Jung, I., Seo, B., Lee, J., Kim, C., & Bock, M. (2014). A dip-stick type biosensor using bioluminescent bacteria encapsulated in color-coded alginate microbeads for detection of water toxicity †. *Analyst*, *139*, 4696–4701. https://doi.org/10.1039/c4an00308j

Kärkkäinen, R. M., Drasbek, M. R., McDowall, I., Smith, C. J., Young, N. W. G., & Bonwick, G. A. (2011). Aptamers for safety and quality assurance in the food industry: Detection of pathogens. *International Journal of Food Science and Technology*, *46*(3), 445–454. https://doi.org/10.1111/j.1365-2621.2010.02470.x

Kast, C. E., & Bernkop-Schnurch, A. (2001). Thiolated polymers - thiomers: development and in vitro evaluation of chitosan-thioglycolic acid conjugates. *Biomaterials*, *22*, 2345–2352.

Kedzierski, S., Khoshnejad, M., & Caltagirone, G. T. (2013). Synthetic Antibodies: The Emerging Field of Aptamers. *Bioprocessing Journal*, *11*(4), 45–49.

Kikuchi, N., May, M., Zweber, M., Madamba, J., Stephens, C., Kim, U., & Mobed-miremadi, M. (2020). Sustainable , Alginate-Based Sensor for Detection of Escherichia coli in Human Breast Milk, 1–15.

Kim, K. S., & Davis, R. E. (1972). Electron Spectroscopyof the Nickel-Oxygen System. *Journal of Electron Spectroscopy and Related Phenomena*, *1*, 251–258.

Kim, S. J., Yoon, S. G., Lee, Y. H., & Kim, S. I. (2004). Bending behavior of hydrogels

composed of poly (methacrylic acid) and alginate by electrical stimulus. *Polymer International*, *53*, 1456–1460. https://doi.org/10.1002/pi.1560

Kingsley, D. M., Capuano, J. A., & Corr, D. T. (2019). On-Demand Radial Electrodeposition of Alginate Tubular Structures. *Biomaterials Science & Engineering*, *5*, 3184–3189. https://doi.org/10.1021/acsbiomaterials.9b00415

Kissinger, P. T., & Heineman, W. R. (1983). Cyclic Voltammetry. *Journal of Chemical Education*, *60*(9), 702–706. https://doi.org/10.1002/0471266965.com050.pub2

Kong, F.-Y., Xu, M.-T., Xu, J.-J., & Chen, H.-Y. (2011). A novel lable-free electrochemical immunosensor for carcinoembryonic antigen based on gold nanoparticles-thionine-reduced graphene oxide nanocomposite film modified glassy carbon electrode. *Talanta*, *85*, 2620– 2625.

Kucherenko, I. S., Chen, B., Johnson, Z., Wilkins, A., Sanborn, D., Figueroa-Felix, N., … Claussen, J. C. (2021). Laser-induced graphene electrodes for electrochemical ion sensing, pesticide monitoring, and water splitting. *Analytical and Bioanalytical Chemistry*, *in press*.

Kurra, N., Jiang, Q., Nayak, P., & Alshareef, H. N. (2019). Laser-derived graphene: A three-dimensional printed graphene electrode and its emerging applications. *Nano Today*, *24*, 81–102. https://doi.org/10.1016/j.nantod.2018.12.003

Kwon, K., Jin, S., Pak, C., Chang, H., Joo, S. H., Lee, H. I., … Kim, J. M. (2011). Enhancement of electrochemical stability and catalytic activity of Pt nanoparticles via strong metal-support interaction with sulfur-containing ordered mesoporous carbon. *Catalysis Today*, *164*, 186–189.

Lavecchia, T., Tibuzzi, A., & Giardi, M. T. (2010). Biosensors for Functional Food Safety and Analysis. In *Bio-Farms for Nutraceuticals: Functional Food and Safety Control by Biosensors* (pp. 267–281).

Lawal, A. T. (2018). Biosensors and Bioelectronics Progress in utilisation of graphene for electrochemical biosensors. *Biosensors and Bioelectronic*, *106*, 149–178. https://doi.org/10.1016/j.bios.2018.01.030

Le, T. N., Tran, T. D., & Kim, M. Il. (2020). A Convenient Colorimetric Bacteria Detection Method Utilizing Chitosan-Coated Magnetic Nanoparticles. *Nanomaterials*, *10*(92).

Lee, K. Y., & Mooney, D. J. (2012). Alginate: properties and biomedical applications. *Progress in Polymer Science*, *37*(1), 106–126. https://doi.org/10.1016/j.progpolymsci.2011.06.003.Alginate

Lin, J., Peng, Z., Liu, Y., Ruiz-Zepeda, F., Ye, R., Errol, L. G., … Tour, J. M. (2014). Laser-induced porous graphene films from commercial polymers. *Nature Communications*, *5*, 5714. https://doi.org/10.1038/ncomms6714.Laser-induced

Lin, Y., Sun, Y., Dai, Y., Sun, W., Zhu, X., Liu, H., … Wang, X. (2020). A "signal-on" chemiluminescence biosensor for thrombin detection based on DNA functionalized magnetic sodium alginate hydrogel and metalloporphyrinic metal-organic framework nanosheets.pdf. *Talanta*, *207*, 120300.

Lipman, N. S., Jackson, L. R., Trudel, L. J., & Weis-Garcia, F. (2005). Monoclonal Versus Polyclonal Antibodies: Distinguishing Characteristics, Applications, and Information Resources. *ILAR Journal*, *46*(3), 258–268.

https://doi.org/10.1093/ilar.46.3.258

Lisdat, F., & Schäfer, D. (2008). The use of electrochemical impedance spectroscopy for biosensing. *Analytical and Bioanalytical Chemistry*, *391*, 1555–1567. https://doi.org/10.1007/s00216-008-1970-7

Liu, A., Zhao, L., Bai, H., Zhao, H., Xing, X., & Shi, G. (2009). Polypyrrole Actuator with a Bioadhesive Surface for Accumulating Bacteria from Physiological Media. *ACS Applied Materials and Interfaces*, *1*(4), 951–955. https://doi.org/10.1021/am9000387

Liu, H., Feng, Y., Cao, H., & Yang, J. (2014). Pt-Containing Ag2S-Noble Metal Nanocomposites as Highly Active Electrocatalysts for the Oxida- tion of Formic Acid. *Nano-Micro Letters*, *6*(3), 252–257.

Liu, J., Zhong, C., Du, X., Wu, Y., Xu, P., Liu, J., & Hu, W. (2013). Pulsed electrodeposition of Pt particles on indium tin oxide substrates and their electrocatalytic properties for methanol oxidation. *Electrochimica Acta*, *100*, 164–170.

Liu, R., Zhang, Y., Ali, S., Haruna, S. A., He, P., Li, H., … Chen, Q. (2021). Development of a fluorescence aptasensor for rapid and sensitive detection of Listeria monocytogenes in food.pdf. *Food Control*, *122*, 107808.

Liu, S. Q. (2007). *Bioregenerative Engineering: Principles and Applications*. John Wiley & Sons, Inc.

Liu, Y., Yang, X., Shi, X.-W., Bentley, W. E., & Payne, G. F. (2010). Biofabrication Based on the Enzyme-Catalyzed Coupling and Crosslinking of Pre-Formed

Biopolymers. *American Chemical Society Symposium Series, Green Polymer Chemistry: Biocatalysis and Biomaterials*.

López-León, T., Carvalho, E. L. S., Seijo, B., Ortega-Vinuesa, J. L., & Bastos-González, D. (2005). Physicochemical characterization of chitosan nanoparticles: Electrokinetic and stability behavior. *Journal of Colloid and Interface Science, 283*(2), 344–351. https://doi.org/10.1016/j.jcis.2004.08.186

Luo, X. L., Xu, J. J., Du, Y., & Chen, H. Y. (2004). A glucose biosensor based on chitosan-glucose oxidase-gold nanoparticles biocomposite formed by one-step electrodeposition. *Analytical Biochemistry, 334*(2), 284–289. https://doi.org/10.1016/j.ab.2004.07.005

Lvovich, V. F. (2012). *Impedance Spectroscopy : Applications to Electrochemical and Dielectric Phenomena*. New Jersy: John Wiley & Sons. Retrieved from https://books.google.com/books?id=FGFcCwAAQBAJ&pg=PA89&lpg=PA89&dq=nyquist+Diagram+for+Mixed+Control+Circuit&source=bl&ots=2whxBAj2ek&sig=xbMgugwHo7oGxU8cSTIUQMfiRKI&hl=en&sa=X&ved=0ahUKEwjkqvrp8Z_TAhXG7YMKHVhmDk8Q6AEISzAL#v=onepage&q=nyquist Diagram

Ma, X., Jiang, Y., Jia, F., Yu, Y., Chen, J., & Wang, Z. (2014). An aptamer-based electrochemical biosensor for the detection of Salmonella. *Journal of Microbiological Methods, 98,* 94–98.

Mabbott, G. A. (1983). An introduction to cyclic voltammetry. *Journal of Chemical Education, 60*(9), 697. https://doi.org/10.1021/ed060p697

Malic, L., Zhang, X., Brassard, D., Clime, L., Daoud, J., Luebbert, C., … Veres, T.

(2015). Polymer-based microfluidic chip for rapid and efficient immunomagnetic capture and release of Listeria monocytogenes. *Lab on a Chip*, *15*, 3994. https://doi.org/10.1039/c5lc00852b

Marcano, Y. C., & Sabino, M. A. (2018). Chemical modification of alginate with L-cysteine to extend its use in drug delivery systems. *Cellulose Chemistry and Technology*, *52*, 559–567.

McLamore, E. S., Alocilja, E., Gomes, C., Gunasekaran, S., Jenkins, D., Datta, S. P. A., … Zhou, A. (2021). FEAST of biosensors: Food, environmental and agricultural sensing technologies (FEAST) in North America. *Biosensors and Bioelectronics*, *178*, 113011.

Mclamore, E. S., Palit, S., Datta, A., Morgan, V., Cavallaro, N., Kiker, G., … Alocilja, E. C. (2019). SNAPS: Sensor Analytics Point Solutions for Detection and Decision Support Systems. *Sensors*, *19*, 4935.

Mirsky, V. M. (2004). *Ultrathin Electrochemical Chemo- and Biosensors*. (O. S. Woltbeis, Ed.) (Springer S). Springer.

Moulder, J. F., Stickle, W. F., Sobol, P. E., & Bomben, K. D. (1992). *Handbook of X-ray Photoelectron Spectroscopy Edited by*. (J. Chastain, Ed.). Perkin-Elmer Corporation.

Mutreja, R., Jariyal, M., Pathania, P., Sharma, A., Sahoo, D. K., & Suri, C. R. (2016). Novel surface antigen based impedimetric immunosensor for detection of Salmonella typhimurium in water and juice samples. *Biosensors and Bioelectronics*, *85*, 707–713. https://doi.org/10.1016/j.bios.2016.05.079

N, W., M, B., S F, B., H, T., L, W., C, B., … M., S. (2016). Evaluating best practices for Campylobacter and Salmonella reduction in poultry processing plants. *Poultry Science*, *95*, 306–315.

Nayak, P., Kurra, N., Xia, C., & Alshareef, H. N. (2016). Highly Efficient Laser Scribed Graphene Electrodes for On-Chip Electrochemical Sensing Applications. *Advanced Electronic Materials*, *2*, 1600185.

Niavol, S. S., Budde, M., Papadogianni, A., Heilmann, M., Moghaddam, H. M., Aldao, C. M., … Schipani, F. (2020). Conduction mechanisms in epitaxial NiO Graphene gas sensors. *Sensors and Actuators: B. Chemical*, *325*, 128797.

Nigam, S., Chandra, S., & Bahadur, D. (2015). Dendrimers based Electrochemical Biosensors, *2*(1), 21–36.

Noordhout, C. M. De, Devleesschauwer, B., Angulo, F. J., Geert, V., Haagsma, J., Kirk, M., … Speybroeck, N. (2014). The global burden of listeriosis: a systematic review and meta- analysis. *Lancet Infect Dis.*, *14*(11), 1073–1082. https://doi.org/10.1016/S1473-3099(14)70870-9

Ohk, S. H., Koo, O. K., Sen, T., Yamamoto, C. M., & Bhunia, A. K. (2010). Antibody-aptamer functionalized fibre-optic biosensor for specific detection of Listeria monocytogenes from food. *Journal of Applied Microbiology*, *109*, 808–817. https://doi.org/10.1111/j.1365-2672.2010.04709.x

Ozawa, F., Ino, K., Takahashi, Y., Shiku, H., & Matsue, T. (2013). Electrodeposition of alginate gels for construction of vascular-like structures, *115*(4), 459–461.

Parate, K., Pola, C. C., Rangnekar, S. V, Mendivelso-Perez, D. L., Smith, E. A., Hersam,

M. C., … Claussen, J. C. (2020). Aerosol-jet-printed graphene electrochemical histamine sensors for food safety monitoring Aerosol-jet-printed graphene electrochemical histamine sensors for food safety monitoring. *2D Materials*, *7*, 034002.

Parate, K., Rangnekar, S. V, Jing, D., Mendivelso-Perez, D. L., Ding, S., Secor, E. B., … Claussen, J. C. (2020). Aerosol-Jet-Printed Graphene Immunosensor for Label-Free Cytokine Monitoring in Serum. *ACS Applied Materials & Interfaces*, *12*, 8592−8603.

Pasparakis, G., & Bouropoulos, N. (2006). Swelling studies and in vitro release of verapamil from calcium alginate and calcium alginate–chitosan beads. *International Journal of Pharmaceutics*, *323*, 34–42.

Payne, B. P., Biesinger, M. C., & Mcintyre, N. S. (2012). Use of oxygen/nickel ratios in the XPS characterisation of oxide phases on nickel metal and nickel alloy surfaces. *Journal of Electron Spectroscopy and Related Phenomena*, *185*, 159–166.

Pendergrast, P. S., Marsh, H. N., Grate, D., Healy, J. M., & Stanton, M. (2005). Nucleic Acid Aptamers for Target Validation and Therapeutic Applications. *Journal of Biomolecular Techniques*, *16*(3), 224–234.

Radhakrishnan, R., Jahne, M., Rogers, S., & Suni, I. I. (2013). Detection of listeria monocytogenes by electrochemical impedance spectroscopy. *Electroanalysis*, *25*(9), 2231–2237. https://doi.org/10.1002/elan.201300140

Ramaswamy, V., Cresence, V. M., Rejitha, J. S., Lekshmi, M. U., Dharsana, K. S., Prasad, S. P., & Vijila, H. M. (2007). Listeria - Review of Epidemiology and

Pathogenesis. *Journal of Microbiology, Immunology, and Infection*, *40*, 4–13.

Reddy, K. M., Babu, V. R., Rao, K. S. V. K., Subha, M. C. S., Rao, K. C., Sairam, M., & Aminabhavi, T. M. (2007). Temperature Sensitive Semi-IPN Microspheres from Sodium Alginate and N-Isopropylacrylamide for Controlled Release of 5-Fluorouracil. *Journal of Applied Polymer Science*, *107*(5), 2820–2829.

Romanchenko, A., Likhatski, M., & Mikhlin, Y. (2018). X-ray Photoelectron Spectroscopy (XPS) Study of the Products Formed on Sulfide Minerals Upon the Interaction with Aqueous Platinum (IV) Chloride Complexes, (Iv). https://doi.org/10.3390/min8120578

Sarabaegi, M., & Roushani, M. (2019). A nano-sized chitosan particle based electrochemical aptasensor for sensitive detection of P. aeruginosa. *Analytical Methods*, *11*, 5591–5597. https://doi.org/10.1039/c9ay01509d

Schild, H. G. (1992). Poly(N-isopropylacrylamide): experiment, theory and application. *Progress in Polymer Science*, *17*(2), 163–249. https://doi.org/10.1016/0079-6700(92)90023-R

Secor, E. B., Prabhumirashi, P. L., Puntambekar, K., Geier, M. L., & Hersam, M. C. (2013). Inkjet Printing of High Conductivity, Flexible Graphene Patterns. *The Journal of Physical Chemistry Letters*, *4*, 1347−1351.

Sharma, S. (2018). Glassy Carbon: A Promising Material for Micro- and Nanomanufacturing. *Materials*, *11*, 1857. https://doi.org/10.3390/ma11101857

Sidhu, R., Cavallaro, N. D., Pola, C. C., Danyluk, M. D., Mclamore, E. S., & Gomes, C. L. (2020). Planar Interdigitated Aptasensor for Flow-Through Detection of Listeria

spp. in Hydroponic Lettuce Growth Media. *Sensors*, *20*, 5773.

Sidhu, R., Rong, Y., Vanegas, D. C., Claussen, J., McLamore, E. S., & Gomes, C. (2016). Impedance biosensor for the rapid detection of Listeria spp. based on aptamer functionalized Pt-interdigitated microelectrodes array. In *SPIE* (Vol. 9863, p. 98630F). https://doi.org/10.1117/12.2223443

Simoska, O., & Stevenson, K. J. (2019). Electrochemical sensors for rapid diagnosis of pathogens in real time. *Analyst*, *144*, 6461–6478.

Singh, S. P., Li, Y., Be, A., Oren, Y., Tour, J. M., & Arnusch, C. J. (2017). Laser-Induced Graphene Layers and Electrodes Prevents Microbial Fouling and Exerts Antimicrobial Action. *ACS Applied Materials and Interfaces*, *9*, 18238−18247. https://doi.org/10.1021/acsami.7b04863

Soares, R. R. A., Hjort, R. G., Pola, C. C., Parate, K., Reis, E. L., Soares, N. F. F., … Gomes, C. L. (2020). Laser-Induced Graphene Electrochemical Immunosensors for Rapid and Label-Free Monitoring of Salmonella enterica in Chicken Broth. *ACS Sensors*, *5*, 1900–1911.

Somerset, V. S. (2011). *Environmental Biosensors*. (V. Somerset, Ed.). Rijeka, Croatia: InTech.

Srinivasan, V., Stiefel, E. I., Elsberry, A., & Walton, R. A. (1979). Sulfur 2p Chemical Shifts Associated with the Binding of Thiol and Thioether Groups to Transition Metal Ions. *Journal of the American Chemical Society*, *101*(10), 2611–2614.

Stapleton, S., Kennedy, R. O., & Tully, E. (2005). IMMUNOASSAYS | Production of Antibodies. In *Encyclopedia of Analytical Science* (Second, pp. 306–316). Elsevier.

Strand, S. P., Tømmeraas, K., Vårum, K. M., & Østgaard, K. (2001). Electrophoretic Light Scattering Studies of Chitosans with Different Degrees of N-acetylation. *Biomacromolecules*, *2*, 1310–1314. https://doi.org/10.1021/bm015598x

Subash, V. S., Alagumalai, K., & Chen, S. (2020). Ultrasonication assisted synthesis of NiO nanoparticles anchored on graphene oxide : an enzyme-free glucose sensor with ultrahigh sensitivity. *New Journal of Chemistry*, *44*, 15071. https://doi.org/10.1039/d0nj02127j

Tabasi, A., Noorbakhsh, A., & Shari, E. (2017). Biosensors and Bioelectronics Reduced graphene oxide-chitosan-aptamer interface as new platform for ultrasensitive detection of human epidermal growth factor receptor 2. *Biosensors and Bioelectronics Journal*, *95*, 117–123. https://doi.org/10.1016/j.bios.2017.04.020

Taguchi, M., Schwalb, N., Rong, Y., Vanegas, D. C., Garland, N., Tan, M., … McLamore, E. S. (2016). PulSED: pulsed sonoelectrodeposition of fractal nanoplatinum for enhancing amperometric biosensor performance. *The Analyst*, *141*(11), 3367–3378. https://doi.org/10.1039/c6an00069j

Tan, S. Y., Acquah, C., Sidhu, A., Ongkudon, C. M., Yon, L. S., Danquah, M. K., … Techniques, B. (2016). SELEX Modifications and Bioanalytical Techniques for Aptamer – Target Binding Characterization. *Critical Reviews in Analytical Chemistry*, *46*(6), 521–537. https://doi.org/10.1080/10408347.2016.1157014

Tehrani, F., & Bavarian, B. (2016). Facile and scalable disposable sensor based on laser engraved graphene for electrochemical detection of glucose. *Scientific Reports*, *6*, 27975. https://doi.org/10.1038/srep27975

Teng, J., Yuan, F., Ye, Y., Zheng, L., Yao, L., Xue, F., & Chen, W. (2016). Aptamer-Based Technologies in Foodborne Pathogen Detection. *Frontiers in Microbiology*, *7*, 1426. https://doi.org/10.3389/fmicb.2016.01426

Thermo Scientific. (2011). Ellman's Reagent.

Thermo Scientific. (2012). Crosslinking technical handbook. Retrieved from https://tools.thermofisher.com/content/sfs/brochures/1602163-Crosslinking-Reagents-Handbook.pdf

Thermo Scientific. (2021). XPS - Sulfur. Retrieved from https://xpssimplified.com/elements/sulfur.php

Thevenot, D. R., Toth, K., Durst, R. A., & Wilson, G. S. (2001). Electrochemical biosensors: recommended definitions and classifications. *Biosensors & Bioelectronics*, *16*, 121–131. https://doi.org/10.1016/S0956-5663(01)00115-4

Torres-Chavolla, E., & Alocilja, E. C. (2009). Aptasensors for detection of microbial and viral pathogens. *Biosensors and Bioelectronics*, *24*, 3175–3182.

USDA. (2014). FSIS Compliance Guideline: Controlling Listeria monocytogenes in Post-lethality Exposed Ready-to-Eat Meat and Poultry Products. *Food Safety and Inspection Service (FSIS)*. Retrieved from http://www.fsis.usda.gov/wps/wcm/connect/d3373299-50e6-47d6-a577-e74a1e549fde/Controlling-Lm-RTE-Guideline.pdf?MOD=AJPERES

USDA. (2019). Pathogen Reduction – Salmonella and Campylobacter Performance Standards Verification Testing. Retrieved from https://www.fsis.usda.gov/wps/wcm/connect/b0790997-2e74-48bf-9799-

85814bac9ceb/28_IM_PR_Sal_Campy.pdf?MOD=AJPERES

USFDA. (2016). *The Reportable Food Registry: A Five Year Overview of Targeting Inspection Resources and Identifying Patterns of Adulteration. United Stated Food and Drug Agency*.

Uz, M., Jackson, K., Donta, M. S., Jung, J., Lentner, M. T., Hondred, J. A., … Mallapragada, S. K. (2019). Fabrication of High-resolution Graphene-based Flexible Electronics via Polymer Casting. *Scientific Reports*, *9*, 10595.

Valderrama, W. B., Dudley, E. G., Doores, S., & Cutter, C. N. (2016). Commercially Available Rapid Methods for Detection of Selected Food-borne Pathogens. *Critical Reviews in Food Science and Nutrition*, *56*(9), 1519–1531. https://doi.org/10.1080/10408398.2013.775567

Vanegas, D. C., Claussen, J., Mclamore, E., & Gomes, C. (2017). Microbial Pathogen Detection Strategies. In *Encyclopedia of Agricultural, Food, and Biological Engineering* (2nd ed., pp. 1–4). CRC Press. https://doi.org/10.1081/E-EAFE2-120051868

Vanegas, D. C., Gomes, C. L., Cavallaro, N. D., Giraldo-Escobar, D., & McLamore, E. S. (2017). Emerging Biorecognition and Transduction Schemes for Rapid Detection of Pathogenic Bacteria in Food. *Comprehensive Reviews in Food Science and Food Safety*, *16*(6), 1188–1205. https://doi.org/10.1111/1541-4337.12294

Vanegas, D. C., Gomes, C., & Mclamore, E. S. (2016). Biosensors for Indirect Monitoring of Foodborne Bacteria. *Biosensors Journal*, *5*(1), 1–3. https://doi.org/10.4172/2090-4967.1000137

Vanegas, D. C., Patiño, L., Mendez, C., de Oliveira, D. A., Torres, A. M., Gomes, C. L., & McLamore, E. S. (2018). Laser scribed graphene biosensor for detection of biogenic amines in food samples using locally sourced materials. *Biosensors*, *8*(2). https://doi.org/10.3390/bios8020042

Vanegas, D. C., Taguchi, M., Chaturvedi, P., Burrs, S., Tan, M., Yamaguchi, H., & McLamore, E. S. (2014). A comparative study of carbon-platinum hybrid nanostructure architecture for amperometric biosensing. *The Analyst*, *139*(3), 660–667. https://doi.org/10.1039/c3an01718d

Velusamy, V., Arshak, K., Korostynska, O., Oliwa, K., & Adley, C. (2010). An overview of foodborne pathogen detection: In the perspective of biosensors. *Biotechnology Advances*, *28*(2), 232–254. https://doi.org/10.1016/j.biotechadv.2009.12.004

Vigués, N., Pujol-Vila, F., Marquez-Maqueda, A., Muñoz-Berbel, X., & Mas, J. (2018). Electro-addressable conductive alginate hydrogel for bacterial trapping and general toxicity determination. *Analytica Chimica Acta*, *1036*, 115–120. https://doi.org/10.1016/j.aca.2018.06.062

Volckova, E., Dudones, L. P., & Bose, R. N. (2002). HPLC Determination of Binding of Cisplatin to DNA in the Presence of Biological Thiols : Implications of Dominant Platinum-Thiol Binding to Its Anticancer Action, *19*(2), 124–131.

Vu, Q. K., Tran, Q. H., Vu, N. P., Anh, T.-L., Dang, T. T. Le, Matteo, T., & Nguyen, T. H. H. (2021). A label-free electrochemical biosensor based on screen-printed electrodes modified with gold nanoparticles for quick detection of bacterial

pathogens. *Materials Today Communications*, *26*, 101726.

Walcarius, A., Minteer, S. D., Wang, J., Lin, Y., & Merkoçi, A. (2013). Nanomaterials for bio-functionalized electrodes: recent trends. *Journal of Materials Chemistry B*, *1*, 4878. https://doi.org/10.1039/c3tb20881h

Wallace, G. G., Chen, J., Li, D., Moulton, S. E., & Razal, J. M. (2010). Nanostructured carbon electrodes. *Journal of Materials Chemistry*, *20*, 3553–3562. https://doi.org/10.1039/b918672g

Wan, W., Dai, G., Zhang, L., & Shen, Y. (2015). Paper-based electrodeposition chip for 3D alginate hydrogel formation. *Micromachines*, *6*(10), 1546–1559. https://doi.org/10.3390/mi6101438

Wan, Z., Umer, M., Lobino, M., Thiel, D., Nguyen, N.-T., Trinchi, A., … Li, Q. (2020). Laser induced self-N-doped porous graphene as an electrochemical biosensor for femtomolar miRNA detection. *Carbon*, *163*, 385–394.

Wang, D., Kou, R., Choi, D., Yang, Z., Nie, Z., Li, J., … Aksay, lhan A. (2010). Ternary self-assembly of ordered metal oxide-graphene nanocomposites for electrochemical energy storage. *ACS Nano*, *4*(3), 1587–1595.

Wang, R., Ruan, C., Kanayeva, D., Lassiter, K., & Li, Y. (2008). TiO 2 Nanowire Bundle Microelectrode Based Impedance Immunosensor for Rapid and Sensitive Detection of Listeria monocytogenes 2008. *Nano Letters*, *8*(0), 2625–2631.

Wang, Y., Ye, Z., & Ying, Y. (2012). New trends in impedimetric biosensors for the detection of foodborne pathogenic bacteria. *Sensors*, *12*(3), 3449–3471. https://doi.org/10.3390/s120303449

Wang, Y., Ye, Z. Z., Si, C. Y., & Ying, Y. Bin. (2012). Application of aptamer based biosensors for detection of pathogenic microorganisms. *Fenxi Huaxue/ Chinese Journal of Analytical Chemistry*, *40*(4), 634–642. https://doi.org/10.1016/S1872-2040(11)60542-2

Wang, Z., Zhang, X., Gu, J., Yang, H., Nie, J., & Ma, G. (2014). Electrodeposition of alginate/chitosan layer-by-layer composite coatings on titanium substrates. *Carbohydrate Polymers*, *103*, 38–45.

Wasito, H., Fatoni, A., Hermawan, D., & Sutji, S. (2019). Ecotoxicology and Environmental Safety Immobilized bacterial biosensor for rapid and e ff ective monitoring of acute toxicity in water. *Ecotoxicology and Environmental Safety*, *170*(November 2018), 205–209. https://doi.org/10.1016/j.ecoenv.2018.11.141

Wen, T., Wang, R., Sotero, A., & Li, Y. (2017). A Portable Impedance Immunosensing System for Rapid Detection of Salmonella Typhimurium. *Sensors*, *17*, 1973. https://doi.org/10.3390/s17091973

White, R. J., Phares, N., Lubin, A. A., Xiao, Y., & Plaxco, K. W. (2008). Optimization of Electrochemical Aptamer-Based Sensors via Optimization of Probe Packing Density and Surface Chemistry. *Langmuir*, *24*, 10513–10518.

WHO. (2018). Salmonella (non-typhoidal) (World Health Organization). Retrieved June 4, 2021, from https://www.who.int/news-room/fact-sheets/detail/salmonella-(non-typhoidal)

Wu, L., Gadre, A. P., Yi, H., Kastantin, M. J., Rubloff, G. W., Bentley, W. E., … Ghodssi, R. (2002). Voltage-Dependent Assembly of the Polysaccharide Chitosan

onto an Electrode Surface. *Langmuir*, *18*(22), 8620–8625.

Wu, W., Fang, Z., Zhao, S., Lu, X., Yu, L., Mei, T., & Zeng, L. (2014). A simple aptamer biosensor for Salmonellae enteritidis based on fluorescence-switch signaling graphene oxide. *RSC Adv.*, *4*(42), 22009–22012. https://doi.org/10.1039/C4RA01901F

Wu, Z., Zhou, G., Yin, L., & Ren, W. (2012). Graphene / metal oxide composite electrode materials for energy storage. *Nano Energy*, *1*(1), 107–131. https://doi.org/10.1016/j.nanoen.2011.11.001

Xia, K., Chiang, W., Fujita, Y., Toyouchi, S., Yuan, H., Su, J., … Uji-i, H. (2020). Photo-induced electrodeposition of metallic nanostructures on graphene. *Nanoscale*, *12*, 11063–11069. https://doi.org/10.1039/d0nr00934b

Xie, X., Tan, F., Xu, A., Deng, K., Zeng, Y., & Huang, H. (2019). UV-induced peroxidase-like activity of gold nanoclusters for differentiating pathogenic bacteria and detection of enterotoxin with colorimetric readout. *Sensors and Actuators B: Chemical*, *279*, 289–297.

Xuan, X., Kim, J. Y., Hui, X., Das, P. S., Yoon, H. S., & Park, J.-Y. (2018). A highly stretchable and conductive 3D porous graphene metal nanocomposite based electrochemical-physiological hybrid biosensor. *Biosensors and Bioelectronics*, *120*, 160–167.

Yang, B., & Agrios, A. G. (2018). Attachment of Pt nanoparticles to a metal oxide surface using a thiol – carboxyl bifunctional molecule OH OH OH. *Journal of Colloid And Interface Science*, *513*, 464–469.

https://doi.org/10.1016/j.jcis.2017.11.058

Yang, H., Li, H., & Jiang, X. (2008). Detection of foodborne pathogens using bioconjugated nanomaterials. *Microfluidics and Nanofluidics*, *5*(5), 571–583. https://doi.org/10.1007/s10404-008-0302-8

Yang, J., Chen, J., Pan, D., Wan, Y., & Wang, Z. (2013). pH-sensitive interpenetrating network hydrogels based on chitosan derivatives and alginate for oral drug delivery. *Carbohydrate Polymers*, *92*, 719–725.

Yang, L., & Bashir, R. (2008). Electrical/electrochemical impedance for rapid detectionof foodborne pathogenic bacteria. *Biotechnology Advances*, *26*, 135–150.

Yang, Y., Song, Y., Bo, X., Min, J., Pak, O. S., Zhu, L., … Gao, W. (2020). A laser-engraved wearable sensor for sensitive detection of uric acid and tyrosine in sweat. *Nature Biotechnology*, *38*, 217–224.

Yasin, H. M., Denuault, G., & Pletcher, D. (2009). Studies of the electrodeposition of platinum metal from a hexachloroplatinic acid bath. *Journal of Electroanalytical Chemistry*, *633*, 327–332.

Ye, R., James, D. K., & Tour, J. M. (2018). Laser-Induced Graphene. *Accounts of Chemical Research*, *51*(7), 1609–1620. https://doi.org/10.1021/acs.accounts.8b00084

Ye, R., Peng, Z., Wang, T., Xu, Y., Zhang, J., Li, Y., & Nilewski, L. G. (2015). In Situ Formation of Metal Oxide Nanocrystals Embedded in Laser-Induced. *ACS Nano*, *9*(9), 9244–9251.

Yu, H., Yu, J., Li, L., Zhang, Y., Xin, S., Ni, X., … Song, K. (2021). Recent Progress of

the Practical Applications of the Platinum Electrochemistry Biosensors. *Frontiers in Chemistry*, *9*, 677876. https://doi.org/10.3389/fchem.2021.677876

Zelada-Guillén, G. A., Bhosale, S. V., Riu, J., & Rius, F. X. (2010). Real-time potentiometric detection of bacteria in complex samples. *Analytical Chemistry*, *82*(22), 9254–9260. https://doi.org/10.1021/ac101739b

Zelada-Guillen, G. A., Riu, J., Düzgün, A., & Rius, F. X. (2009). Immediate Detection of Living Bacteria at Ultralow Concentrations Using a Carbon Nanotube Based Potentiometric Aptasensor. *Angewandte Chemie International Edition Engl*, *48*(40), 7334–7337. https://doi.org/10.1002/anie.200902090

Zhan, X., Hu, G., Wagberg, T., Zhan, S., & Xu, H. (2016). Electrochemical aptasensor for tetracycline using a screen-printed carbon electrode modified with an alginate film containing reduced graphene oxide and magnetite (Fe3O4) nanoparticles. *Microchimica Acta*, *183*, 723–729. https://doi.org/10.1007/s00604-015-1718-y

Zhang, J., Ren, M., Li, Y., & Tour, J. M. (2018). In Situ Synthesis of Efficient Water Oxidation Catalysts in Laser-Induced Graphene. *ACS Energy Letters*, *3*, 677–683. https://doi.org/10.1021/acsenergylett.8b00042

Zhang, Y, Austin, R. H., Kraeft, J., Cox, E. C., & Ong, N. P. (2002). Insulating Behavior of λ-DNA on the Micron Scale. *Physical Review Letters*, *89*, 2–5. https://doi.org/10.1103/PhysRevLett.89.198102

Zhang, Yuhan, Zhu, H., Sun, P., Sun, C., Huang, H., Guan, S., … Qin, K.-R. (2019). Laser-induced Graphene-based Non-enzymatic Sensor for Detection of Hydrogen Peroxide. *Electroanalysis*, *31*, 1334–1341. https://doi.org/10.1002/elan.201900043

Zhao, X., Liu, Y., Lu, J., Zhou, J., & Li, J. (2012). Temperature-responsive polymer/carbon nanotube hybrids: Smart conductive nanocomposite films for modulating the bioelectrocatalysis of NADH. *Chemistry - A European Journal*, *18*(12), 3687–3694. https://doi.org/10.1002/chem.201103259

Zhi, M., Xiang, C., Li, J., Li, M., & Wu, N. (2013). Nanostructured carbon-metal oxide composite electrodes for supercapacitors: a review. *Nanoscale*, *5*, 72–88. https://doi.org/10.1039/c2nr32040a

Zhu, D., Yan, Y., Lei, P., Shen, B., Cheng, W., Ju, H., & Ding, S. (2014). A novel electrochemical sensing strategy for rapid and ultrasensitive detection of Salmonella by rolling circle amplification and DNA – AuNPs probe. *Analytica Chimica Acta*, *846*, 44–50.

APPENDIX A

SUPPORTING INFORMATION CHAPTER II RAPID AND LABEL-FREE *LISTERIA MONOCYTOGENES* DETECTION BASED ON STIMULI-RESPONSIVE ALGINATE-PLATINUM THIOMER NANOBRUSHES

Sensor Biofunctionalization

The biofunctionalization of the ALG-thiomer/Pt brush electrodes was performed using an aptamer that targets the protein Internalin A (A8, 5'-ATC CAT GGG GCG GAG ATG AGG GGG AGG AGG GCG GGT ACC CGG TTG AT-3', 47 mers, GeneLink, Hawthrone, NY) on *Listeria monocytogenes* membrane. For this aptamer, two different functional groups were tested at the 5' end termination, one with thiol and one with amine. The thiol modified aptamers were first reduced using dithiothreitol (DTT) and reconstituted in Tris EDTA (TE) buffer at pH 7.4 according to protocol provided by the manufacturer (GeneLink, 2011). The thiol terminated aptamers were diluted in TE buffer and the electrodes submerged in this suspension for two hours, shaking gently. For the amine-terminated aptamers, EDC/NHS crosslinking reaction was used. The electrodes were individually placed in 500 µL of the activation solution (0.1 M MES buffer (pH 6.0,), 0.5 M NaCl, 75 µM EDC, 25 µM NHS) for 30 min at room temperature. Next, the electrodes were transferred to a TE solution containing amine-terminated aptamers for 2 hours under gentle shaking (Balamurugan, Obubuafo, Soper, & Spivak, 2008a; Jantra et al., 2011). The attachment of different concentrations of each aptamer were evaluated:

200, 400, 800 and 1200 nM for the amino terminated, and 400, 800, 1200 and 1600 nM for the thiol terminated aptamer.

Aptamer loading onto ALG-thiomer/Pt brush electrodes was optimized based on ESA calculated from voltammograms in 4 mM K_4FeCN_6 at pH 7. As expected, the aptamer caused a decrease in ESA due to steric hindrance (Figure A1). It has been shown that DNA acts as an insulator (Bockrath et al., 2002; Gómez-Navarro et al., 2002; Y Zhang, Austin, Kraeft, Cox, & Ong, 2002). This effect caused by aptamer attachment in the ESA was also observed by Hills et al. (2018). The electrodes functionalized with the thiol terminated aptamer presented similar ($p > 0.05$) ESA percentage change for the three lowest loading concentrations, and 800 nM (highest numerical value) was chosen for further tests with bacteria. However, the performance of the electrodes functionalized with the thiol terminated aptamer was highly inconsistent and with poor LOD (21.91 ± 1.24 CFU/mL) on the preliminary tests with bacteria, consequently this aptamer was not used for further experiments. For the amino terminated aptamer, despite no significant difference ($p > 0.05$) between 200 nM and 400 nM loading concentration, 400 nM was chosen for better comparison with previous results from the group when working with alginate. Moreover, aptamer packing density and steric hindrance play an important role in sensing performance (White, Phares, Lubin, Xiao, & Plaxco, 2008) and based on Figure A1, it seems that above 400 nM loading the electrodes have reached a saturation point.

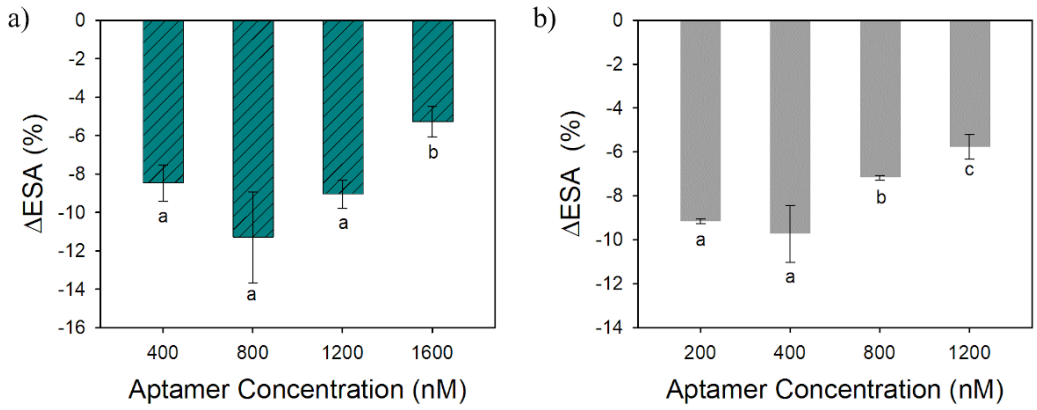

Figure A1 Comparison of electroactive surface area change (%) for the ALG-thiomer/Pt brush at different loading concentrations of a) thiol terminated aptamer, and b) amine terminated aptamer. Based on these results 800 nM of the thiol terminated aptamer and 400 nM of the amine terminated aptamer were used on further experiments with bacteria. Error bars represent the standard deviation. Bars denoted by different letters are significantly different from each other ($p < 0.05$).

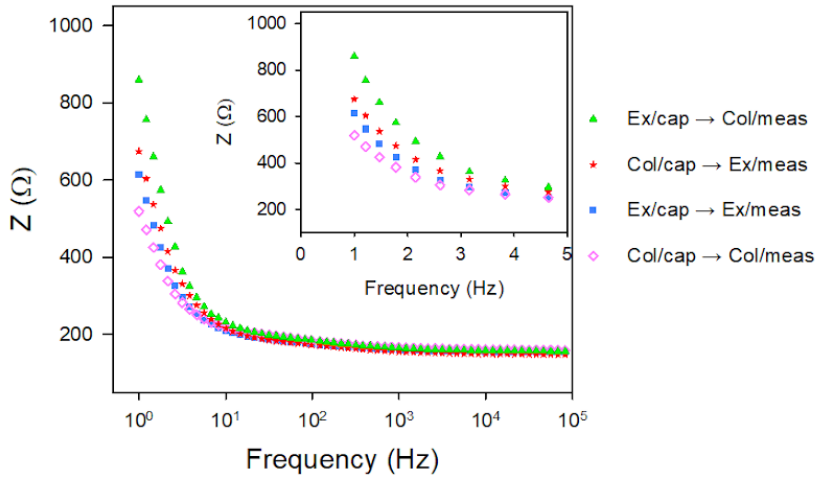

Figure A2 Representative bode plot for different actuation strategies for bacteria capture and sensing over the frequency range of 1–100,000 Hz (inset show exploded view over the frequency range from 1–5 Hz) for the ALG-thiomer/Pt brush sensor functionalized with 400 nM aptamer exposed to 10^3 CFU/mL of *L. monocytogenes*. "EX" refers to extended state (pH 7), "COL" refers to the collapsed brush state (pH 3), "cap" refers to cell capture and "meas" refers to measurement.

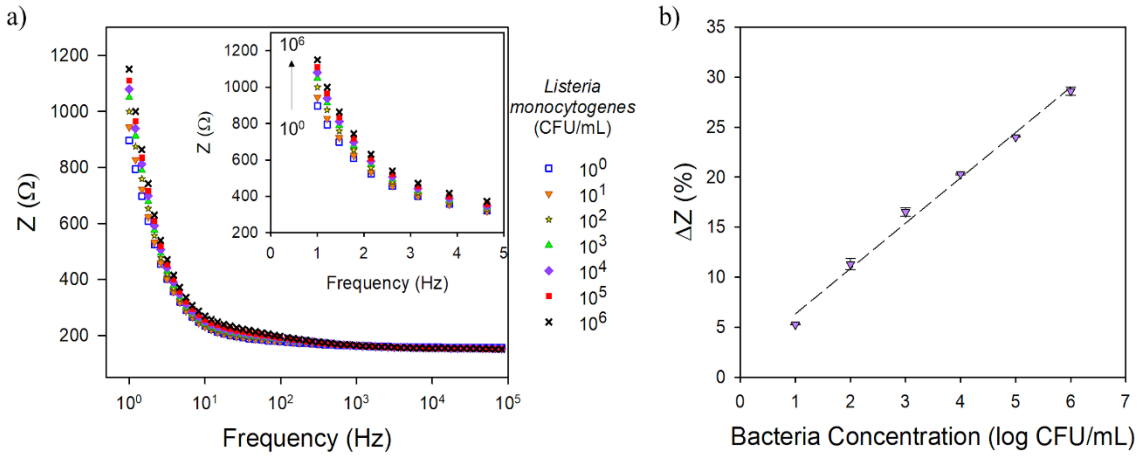

Figure A3 a) Representative Bode plot over the frequency range of 1-100,000 Hz (inset show exploded view over the frequency range from 1-5 Hz) and b) Calibration curve (total impedance change at 1 Hz vs. log bacteria concentration) for the ALG-thiomer/Pt brush sensor without functionalization with aptamer exposed to *L. monocytogenes* in PBS. All data represents the average of three repetitions. Error bars represent the standard deviation.

APPENDIX B

SUPPORTING INFORMATION CHAPTER III ONE-STEP FABRICATION OF STIMULI-RESPONSIVE CHITOSAN-PLATINUM BRUSHES FOR *LISTERIA MONOCYTOGENES* DETECTION

Materials and Methods

Sensor Biofunctionalization

An aptamer that targets the protein Internalin A on *Listeria monocytogenes* membrane known as A8 (5′-ATC CAT GGG GCG GAG ATG AGG GGG AGG AGG GCG GGT ACC CGG TTG AT-3′) was purchased from GeneLink (Hawthrone, NY). Upon receiving, the thiol terminated aptamers were reduced using dithiothreitol (DTT) and reconstituted in Tris EDTA (TE) buffer at pH 7.4, according to protocol provided by the manufacturer (GeneLink). Decapped thiol-terminated A8 aptamer was loaded on the CHI/Pt (non-thiolated) and CHI-thiomer/Pt (thiolated) nanobrushes. For the CHI/Pt brush electrodes, the Sulfo-SMCC crosslinking reaction was used. Briefly, the first step was to individually immerse the CHI/Pt brush electrodes in 500 µL of the Sulfo-SMCC solution (5 mg Sulfo-SMCC dissolved in 100 µL filtered water then diluted in 9.9 mL PBS at pH 7.2) and allowed to react for 45 min at room temperature, shaking gently. Next, the maleimide-activated CHI/Pt brushes were placed in a PBS solution (pH 7.2) containing thiol-terminated aptamers (500, 1000 and 1500 nM) for 1 hour and 15 min, shaking gently (Balamurugan, Obubuafo, Soper, & Spivak, 2008b). Finally, the aptamer-CHI/Pt brushes were rinsed and stored in PBS until further use. For the CHI-thiomer/Pt

brush electrodes, the aptamers were diluted in TE buffer and the electrodes submerged in this solution for two hours, shaking gently.

Results and Discussion

CHI/Pt Material Characterization

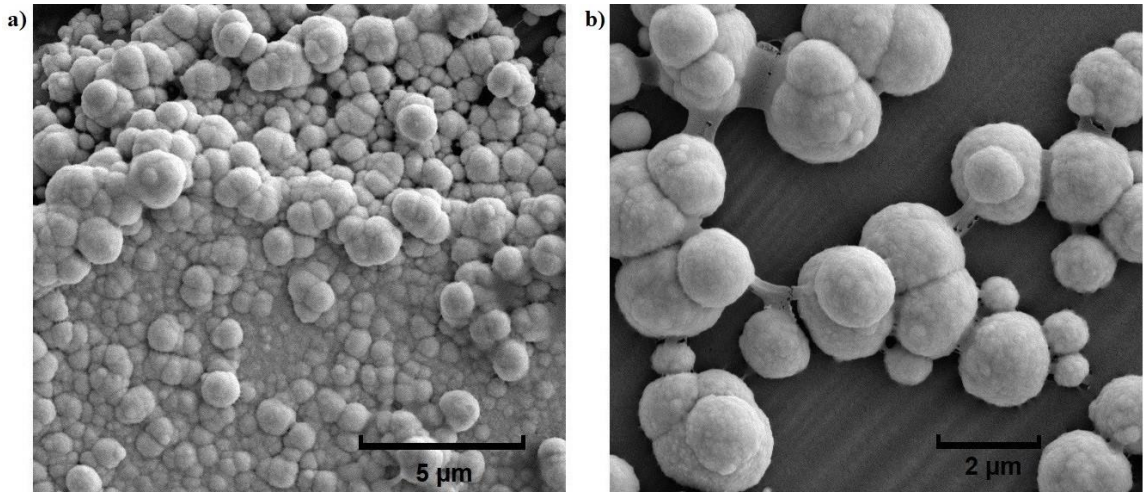

Figure B1 SEM images of CHI/Pt brushes at 10 kV. a) 10,100 and b) 15,000 times magnification showing a heterogeneous surface with non-uniform distribution of CHI/Pt brushes featuring spheroid structures.

CHI/Pt Bacteria Sensing

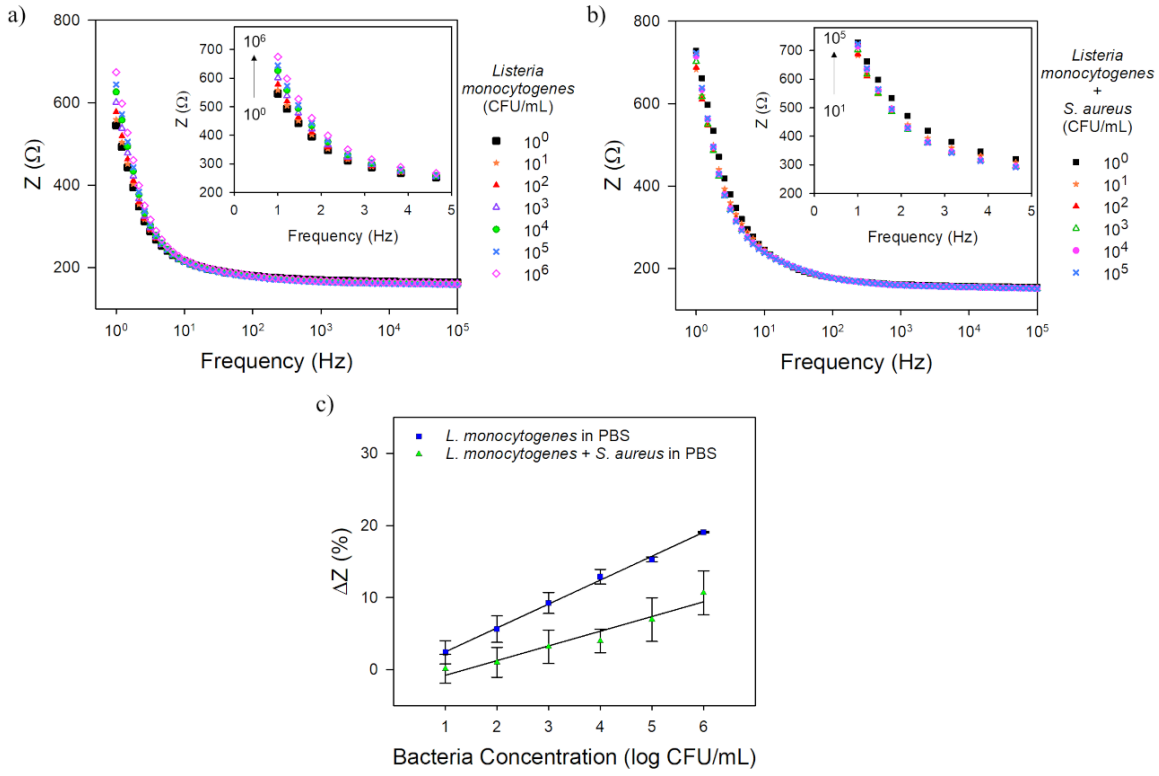

Figure B2 Representative Bode plot over the frequency range of 1–100,000 Hz (inset show exploded view over the frequency range from 1–5 Hz) for the CHI/Pt brush sensor without functionalization with aptamer exposed to a) *L. monocytogenes* in PBS, b) *L. monocytogenes* and *S. aureus* in PBS, and c) calibration curves (impedance change at 1 Hz vs. log bacteria concentration). All data represents the average of three repetitions. Error bars represent the standard deviation.

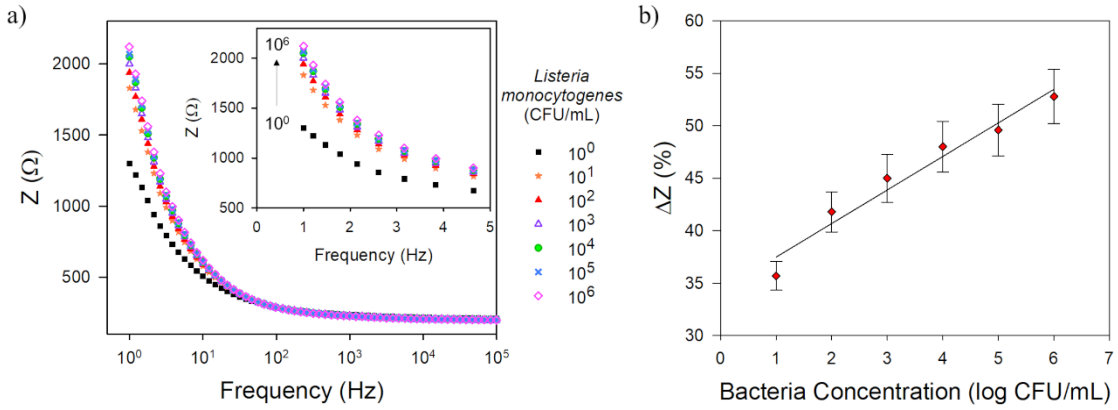

Figure B3 Representative Bode plot over the frequency range of 1–100,000 Hz (inset show exploded view over the frequency range from 1–5 Hz) for the CHI/Pt brush sensor without functionalization with aptamer exposed to a) *L. monocytogenes* in chicken broth, and b) calibration curve (impedance change at 1 Hz vs. log bacteria concentration). All data represents the average of three repetitions. Error bars represent the standard deviation.

Table B1 Performance of the CHI/Pt brush biosensor without functionalization with aptamer when exposed to *Listeria monocytogenes* in different media.

Test medium	**Detection range (CFU/mL)***
PBS	3.1 - 10^6
PBS + *S. aureus*	11 - 10^5
Chicken broth	22 - 10^6

* lowest value corresponds to the lower limit of detection (LOD).

CHI-thiomer Material Characterization

The main differences on the spectra of the CHI-thiomer/Pt (Figure B4) from the CHI/Pt (Figure 3.2 on the main manuscript) brush depositions are: 1) the presence of the S 2p peak and 2) the Pt 4f is deconvoluted into two doublets at 71, 72, 74.4, and 75.3 eV,

which is consistent with literature reports for unbound Pt^0 and S-bonded Pt (Kwon et al., 2011; Romanchenko et al., 2018; B. Yang & Agrios, 2018). This was expected as platinum has tremendous affinity for binding to sulfur donors compared to nitrogen donor ligands (Volckova, Dudones, & Bose, 2002).

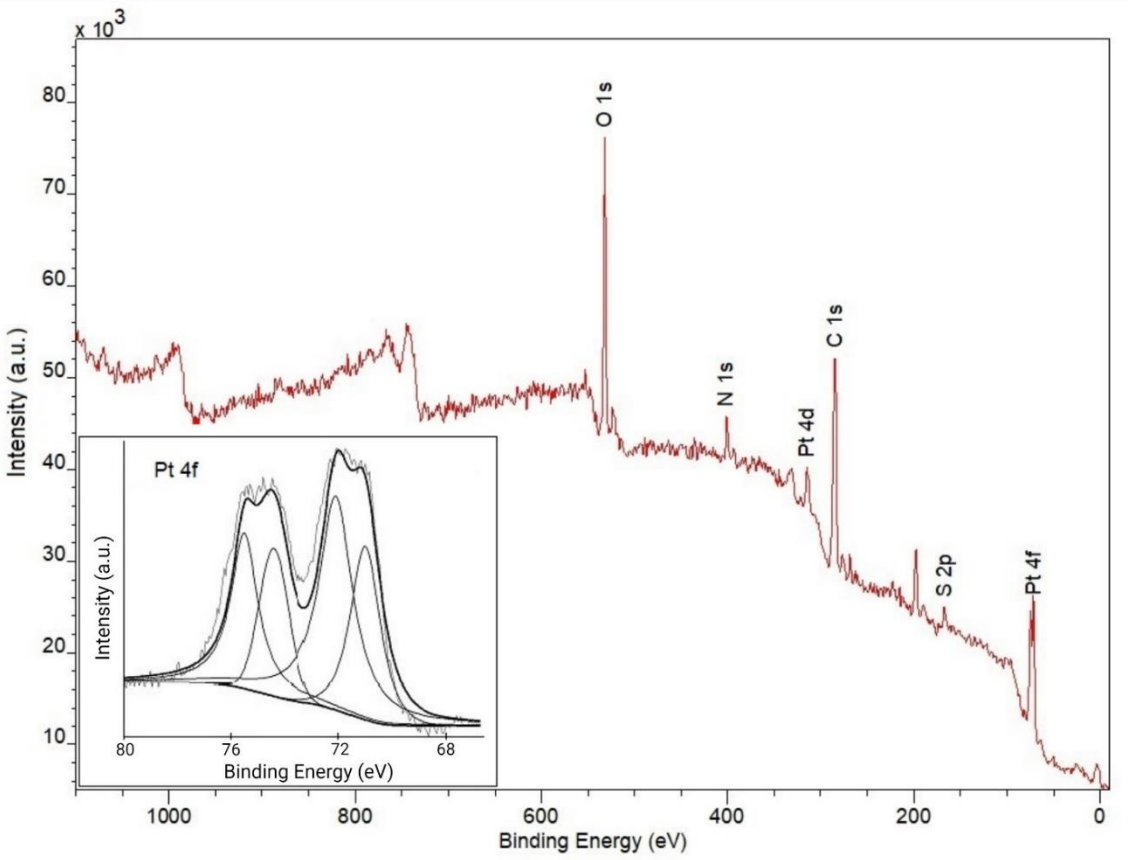

Figure B4 X-ray photoelectron spectroscopy (XPS) survey spectrum of the CHI-thiomer/Pt brush deposition. Inset shows the Pt 4f spectrum indicating the presence of S 2 p peak unbound Pt^0 and S-bonded Pt.

Figure B5 shows SEM for the optimized CHI-thiomer/Pt brush deposition (60 cycles / 6 V / 0.15% CHI-thiomer/Pt). The electrodeposition of CHI-thiomer/Pt brush

led to heterogenous spatial distribution and non-uniform brush sizes distribution on the electrode surface. The SEM images indicate that there is a Pt layer covering the entire electrode and some clusters of CHI-thiomer/Pt brushes dispersed over it forming a network of spherical particles ranging from 100 to 1000 nm.

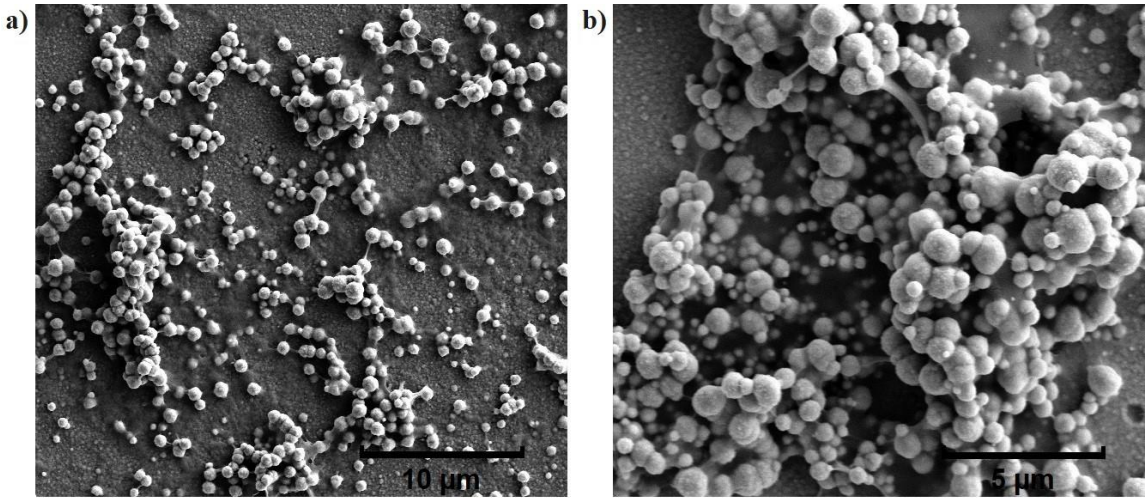

Figure B5 SEM images of CHI-thiomer/Pt brushes at 10 kV and a) 5,100 and b) 10,100 times magnification indicate a non-homogenous and dispersed brush distribution with varying brush sizes resembling a network of spherical particles with diameters between 100 and 1000 nm.

Electrochemical Characterization and Actuation of CHI-thiomer/Pt Nanobrushes

When applying 60 cycles / 6V / 0.15% CHI-thiomer/Pt for the deposition, the increase in ESA was of 12 times (0.36 ± 0.01 cm^2) compared to bare Pt/Ir electrodes (Figure B6a). The hypothesis behind the modification of the chitosan with TGA was that the incorporation of a thiol termination would deposit chitosan brushes embedded with Pt nanoparticles that was expected to result in a more significant increase on the ESA than observed here when compared to the non-modified CHI/Pt brush deposition. Even

though ESA values increased by 12 times with CHI-thiomer/Pt, the non-modified CHI/Pt deposition showed an ESA increase of 11 times without the need for chemical modification as well as a more homogeneous brush deposition onto the electrodes (Figures 3.3, 3.4 and B1) which will later demonstrate enhanced sensing performance. The actuation tests performed using different redox probes with the CHI-thiomer/Pt brush electrodes (Figure B6b) show that the modification of chitosan with thioglycolic acid did not affect the pH stimuli property of chitosan exhibiting the same behavior shown in Figure 3.5 for the CHI/Pt brush electrodes.

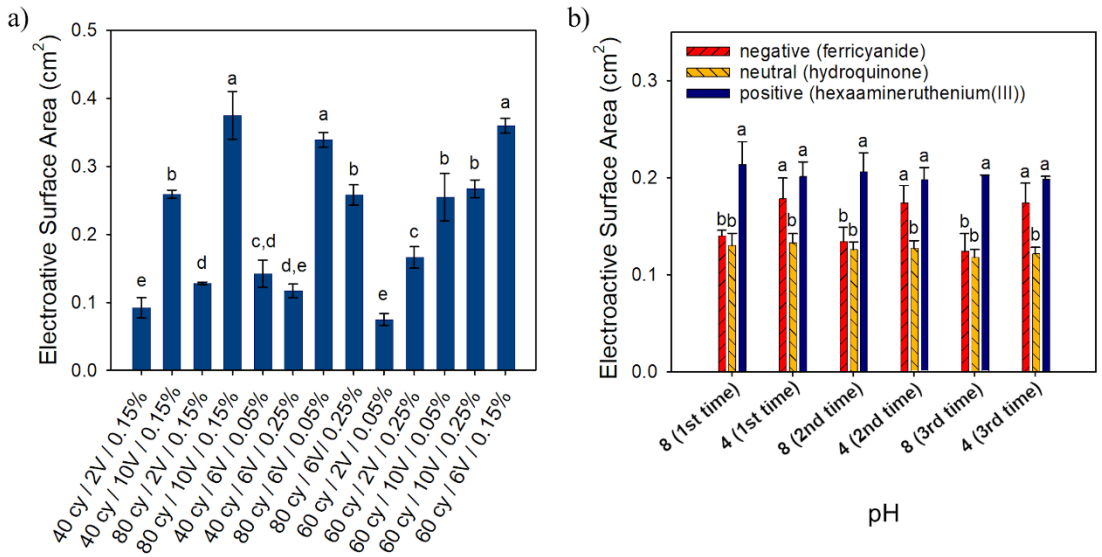

Figure B6 Electrochemical characterization of CHI-thiomer/Pt brushes. (a) Average electroactive surface area (ESA) for various electrode modifications with different number of cycles (cy), voltages (V) and CHI-thiomer concentration (wt.%) using 4 mM K_4FeCN_6 as redox probe. (b) Electrostatic interactions during CHI-thiomer/Pt brush actuation for various redox probes: a negatively charged probe ($KFeCN_6^{3-}$), a neutral probe ($C_6H_4(OH)_2$), and a positively charged probe ($Ru(NH_3)_6^{3+}$. The average electroactive surface area (ESA) is shown for each redox probe under repeated actuation at pH 4 and pH 8 (n = 3). All data represent the average of three replicates and error bars represent the standard deviation of the arithmetic mean; letters denote significantly different means ($p < 0.05$).

Aptamer loading

The functionalization of aptamers onto CHI/Pt and CHI-thiomer/Pt brushes was optimized using CV. As shown in Figure B7, the aptamer attachment caused a decrease in ESA values due to steric hindrance, which was also observed by Hills et al. (2018). This could be expected as the aptamer used is a nucleic acid sequence and it has been shown that DNA can act as an insulator (Bockrath et al., 2002; Gómez-Navarro et al., 2002; Y Zhang et al., 2002). The CHI-thiomer/Pt brushes (Figures B7c and B7d) presented similar ($p > 0.05$) ESA percentage change independent of the aptamer concentration loaded and 800 nM was chosen for further experiments with bacteria. For the CHI/Pt brushes functionalized with aptamers (Figures B7a and B7b), the ones loaded with 1000 nM presented the highest value in ESA change, despite of not being significantly different ($p > 0.05$) from the ones with 1500 nM. Hence, the aptamer concentration of 1000 nM was chosen for better comparison with previous results from the group when working with chitosan.

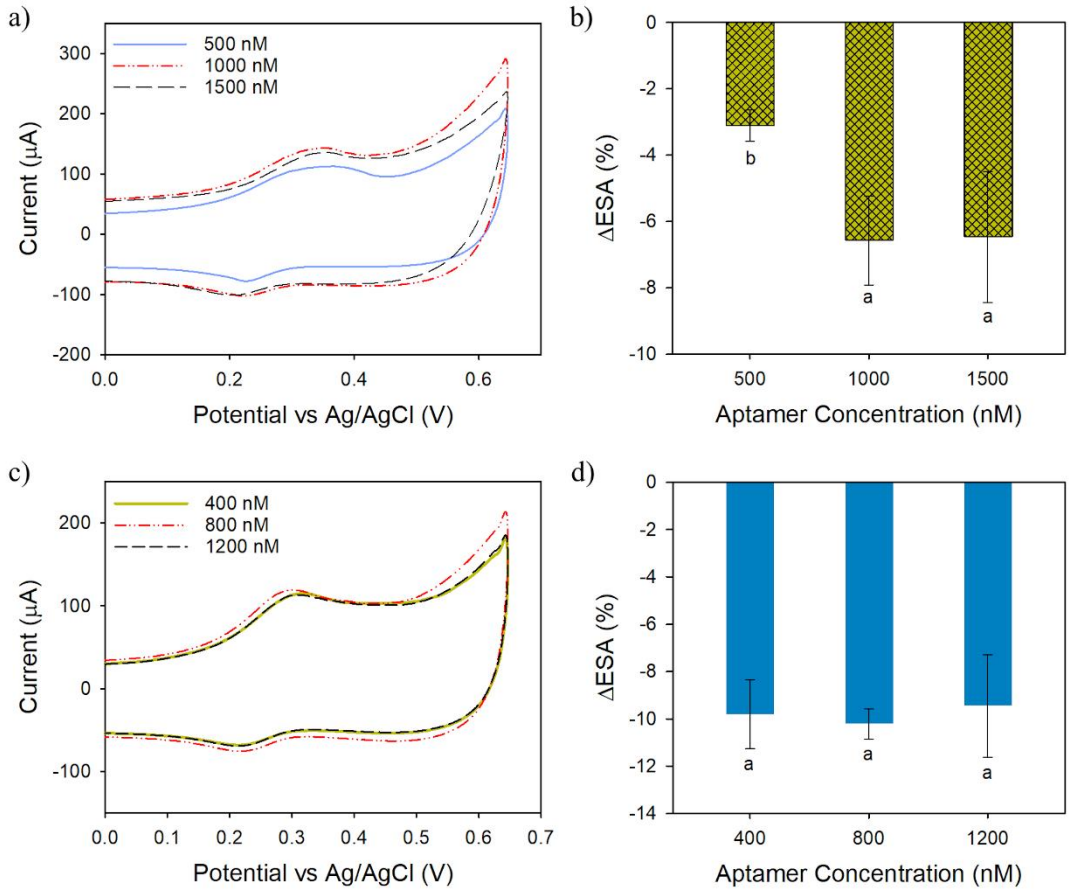

Figure B7 Representative CV curves at 100 mV s^{-1} and comparison of electroactive surface area (ESA) change (%) for (a, b) CHI/Pt, and (c, d) CHI-thiomer/Pt brushes at different aptamer concentrations. Curves represent the average of three replications. Bars denoted by different letters are significantly different from each other ($p < 0.05$). Error bars represent the standard deviation.

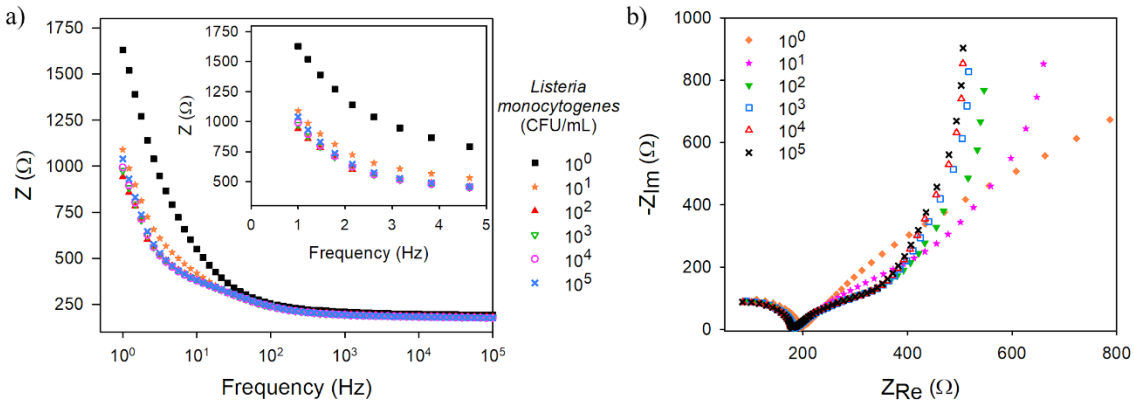

Figure B8 a) Representative Bode plot over the frequency range of 1–100,000 Hz (inset show exploded view over the frequency range from 1–5 Hz), and b) representative Nyquist plots of impedance spectra for the CHI-thiomer/Pt brush sensor functionalized with 800 nM aptamer exposed to increasing concentration of *L. monocytogenes* in PBS. All data represents the average of three repetitions.

APPENDIX C

SUPPORTING INFORMATION CHAPTER IV LASER-INDUCED GRAPHENE WITH NICKEL OXIDE NANOPARTICLES ELECTROCHEMICAL IMMUNOSENSOR FOR RAPID AND LABEL-FREE DETECTION OF *SALMONELLA ENTERICA* TYPHIMURIUM

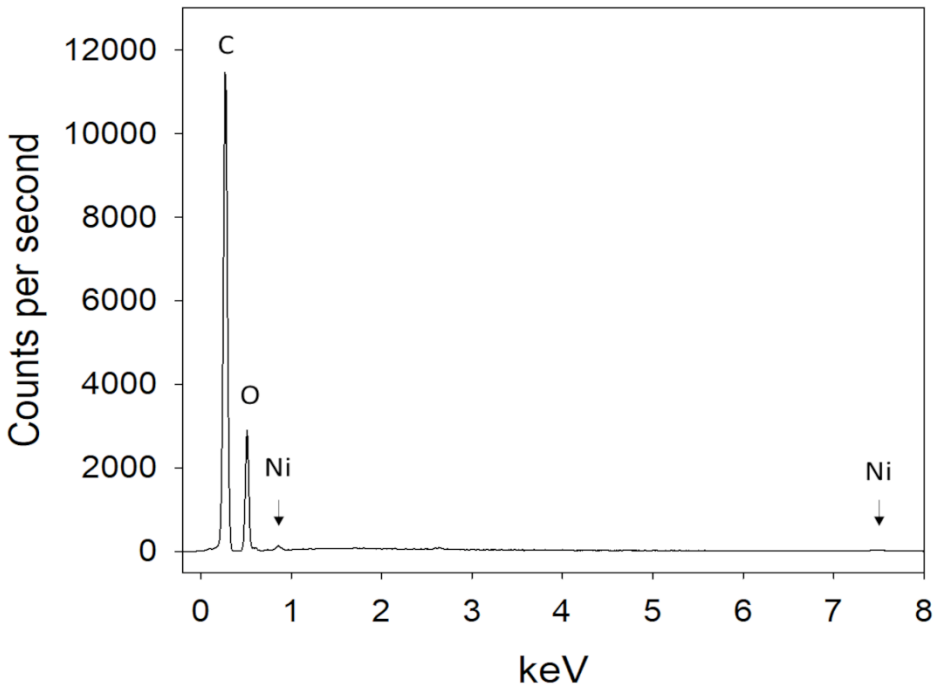

Figure C1 EDS spectrum of the LIG-NiO electrode, showing the predominance of carbon and smaller portions of oxygen and nickel, indicating the change in chemical composition and chemical bonds from the polyimide film after laser processing as well as the deposition of NiO.

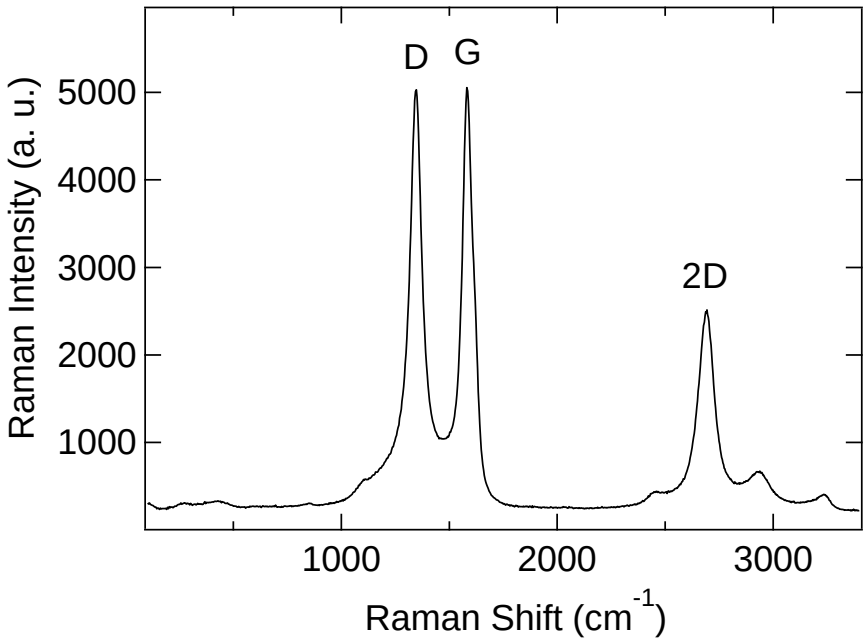

Figure C2 Average Raman spectrum of the LIG-NiO electrode showing the three characteristic peaks of graphene (D, G, and 2D) with a ratio $I_{2D}/I_G = 0.48 \pm 0.03$ that indicates the multilayer graphene formation.

Fitting the EIS data performed on the bare LIG-NiO electrode to the Randles equivalent circuit (Figure C3) resulted in a charge transfer resistance (R_{ct}) value of 212.8 ± 3.4 **Ω**. This value was lower than the R_{ct} reported by Subash, Alagumalai, & Chen (2020) (370 **Ω**) for glassy carbon-nickel oxide electrodes, which could be expected as non-graphitizing carbons exhibit a lower electrical conductivity than the graphitizing ones as it was the case of this work (Sharma, 2018).

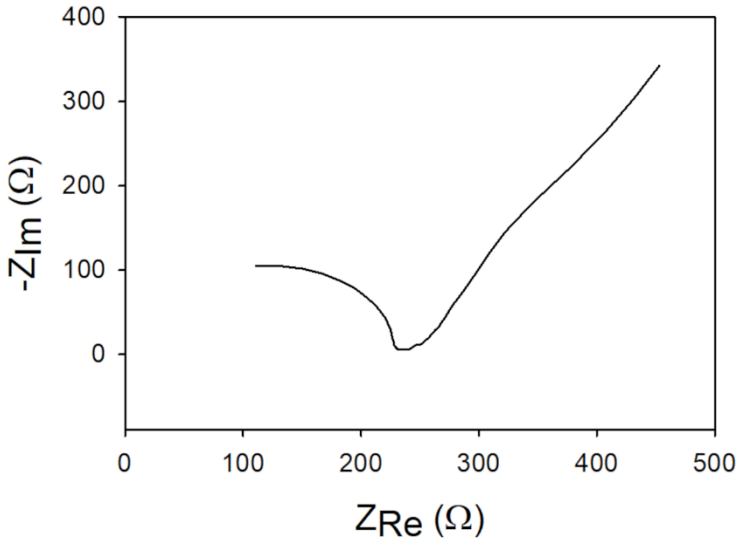

Figure C3 Representative Nyquist of impedance spectra for the LIG-NiO electrode, the inset shows the equivalent Randles circuit used to fit the curve and to calculate the R_{ct} (212.8 ± 3.4 **Ω**).